Investigation of Blunt Trailing Edge Noise from an Asymmetric Airfoil under Different Aerodynamic Loads

Kathrin Stahl

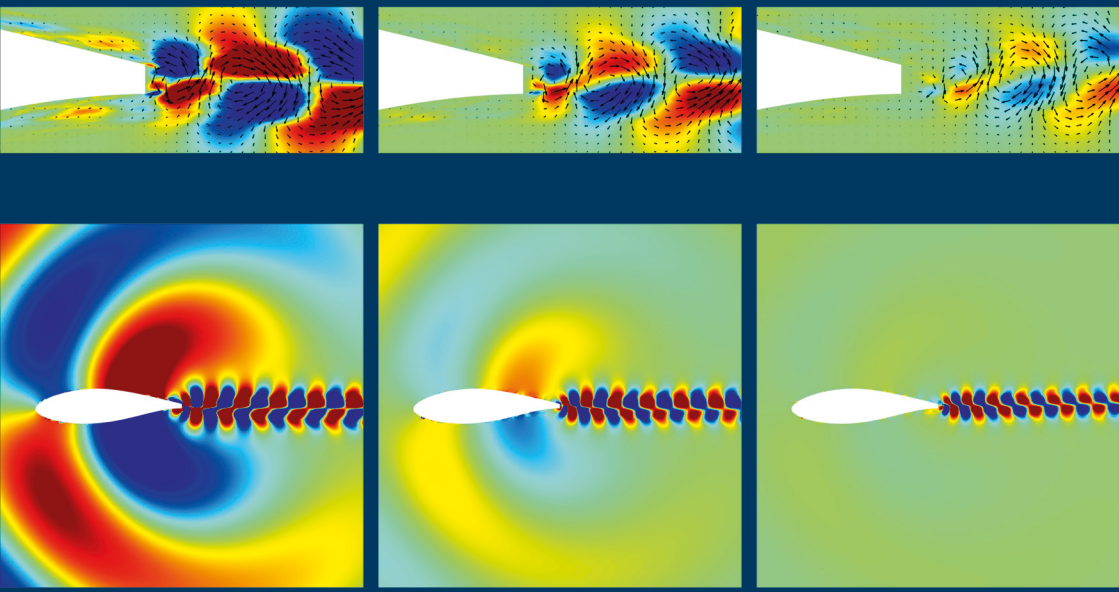

Investigation of Blunt Trailing Edge Noise from an Asymmetric Airfoil under Different Aerodynamic Loads

DISSERTATION

zur Erlangung des Grades eines Doktors
der Ingenieurwissenschaften

vorgelegt von

M.Sc. Kathrin Stahl

geb. am 12.12.1980 in Gummersbach

eingereicht bei der Naturwissenschaftlich-Technischen Fakultät
der Universität Siegen

Siegen 2023

Betreuerin und erste Gutachterin
Prof. Dr.-Ing. Sabine Roller
Technische Universität Dresden
Deutsches Zentrum für Luft- und Raumfahrt
Institut für Softwaremethoden und Produktvirtualisierung

Zweite Gutachterin
Prof. Marlène Sanjosé Ph.D.
Université du Québec
École de Technologie Supérieure, Montreal, Kanada

Dritter Gutachter
Prof. Dr.-Ing. Thomas Carolus
Universität Siegen

Tag der mündlichen Prüfung:
07.08.2023

Berichte aus der Strömungstechnik

Kathrin Stahl

Investigation of Blunt Trailing Edge Noise from an Asymmetric Airfoil under Different Aerodynamic Loads

Shaker Verlag
Düren 2023

Bibliographic information published by the Deutsche Nationalbibliothek
The Deutsche Nationalbibliothek lists this publication in the Deutsche Nationalbibliografie; detailed bibliographic data are available in the Internet at http://dnb.d-nb.de.

Zugl.: Siegen, Univ., Diss., 2023

Printed in Germany.

ISBN 978-3-8440-9285-1
ISSN 0945-2230

Shaker Verlag GmbH • Am Langen Graben 15a • 52353 Düren
Phone: 0049/2421/99011-0 • Telefax: 0049/2421/99011-9
Internet: www.shaker.de • e-mail: info@shaker.de

KURZFASSUNG

Diese Arbeit befasst sich mit dem Schall von der Hinterkante eines zweidimensionalen Tragflächensegments in einer Luftströmung. Von Interesse ist der Mechanismus der strömungsinduzierten Schallerzeugung an der Hinterkante unter besonderer Berücksichtigung deren Stumpfheit.

Anders als bei vielen bekannten Studien wird eine typische asymmetrische Profilierung des Tragflügelsegments gewählt, hier mit dem Profil DU93W210. Dieses wird z.B. häufig bei Windturbinen eingesetzt. Durch Verkürzen der Sehnenlänge wird die Stumpfheit der Hinterkante in mehreren Schritten erhöht. Variiert werden weiterhin die Anströmgeschwindigkeit sowie der Anstellwinkel. Eine Vergrößerung des Anstellwinkels entspricht einer Erhöhung der aerodynamischen Belastung des Tragflügels. Die Studie beschränkt sich auf den Fall einer vollständig turbulente Grenzschicht von der Vorder- bis zur Hinterkante sowohl auf der Saug- als auch der Druckseite, was durch die relativ großen Werte der sehnenbasierten REYNOLDS-Zahl (bis zu 1.2×10^6) in Kombination mit einem sorgfältig gewählten Grenzschichttripping erreicht wird. Die Studienergebnisse werden primär mit dem numerischen Lattice-BOLTZMANN-Verfahren als Computational Aeroacoustic Methode erzielt, jedoch stichprobenartig durch Messungen in einem aeroakustischen Windkanal erfolgreich validiert.

Der beobachtete strömungsinduzierte Schall ist breitbandig mit einer fallweise ausgeprägten tonalen Komponente. Solange die aerodynamische Belastung des Tragflächensegments, d.h. der Anstellwinkel, vergleichsweise gering ist, existiert ein dominanter Ton, dessen Schalldruckpegel mit der Stumpfheit der Hinterkante wächst. Wird die Belastung erhöht, verschwindet der Ton, und es ist dann nur ein breitbandiges Rauschen hörbar. Die Frequenz des Tons nimmt mit der Stumpfheit ab und der REYNOLDS-Zahl zu. Das Kriterium von BLAKE für die Existenz eines Tons bei stumpfer Hinterkante erweist sich als notwendig aber nicht als hinreichend. Bereits eine Analyse des zeitlich gemittelten Geschwindigkeitsfelds zeigt, dass sich mit Erhöhung der Stumpfheit allmählich ein zweiter Wirbel im nahen Nachlauf entwickelt. Diese Wirbel lösen sich alternierend von der Hinterkante ab und es entsteht eine Wirbelstraße. Mit Methoden der Modalanalyse konnte das Strömungsfeld in kohärenten Strukturen zerlegt werden. Durch eine dieser räumlich und zeitlich im Detail aufgelösten kohärenten Strukturen wird die zuvor beschriebene Wirbelstraße repräsentiert. Bei großer Stumpfheit und vergleichsweise geringer aerodynamischer Belastung des Tragflügelsegments befinden sich die abgehenden Wirbel nahe an der Hinterkante. Mit zunehmender aerodynamischer Belastung des Tragflügels wird die Asymmetrie der Strömung zwischen saug- und druckseitiger Grenzschicht größer. Dies hat zur Folge, dass selbst bei vergleichsweise stumpfen Hinterkanten sich die Wirbel erst stromabwärts von der Hinterkante ausbilden, weshalb die typische "blunt trailing edge"- Signatur ausbleibt.

ABSTRACT

This work deals with the noise from the trailing edge of a two-dimensional airfoil segment in airflow. Of interest is the mechanism of flow-induced noise generation at the trailing edge with special consideration of its bluntness.

Unlike in many well-known studies, a typical asymmetric airfoil is chosen for the segment, here the DU93W210 airfoil. This is frequently used for wind turbines, for example. By shortening the chord length, the bluntness of the trailing edge is increased in several steps. Furthermore, the inflow velocity and the angle of attack are varied. An enlargement of the angle of attack corresponds to an increase of the aerodynamic load on the airfoil. The study is limited to the case of a fully turbulent boundary layer from leading to trailing edge on both, the suction and pressure side. This is achieved by operation at relatively large values of the chord-based REYNOLDS number (up to 1.2×10^6) in combination with a carefully chosen boundary layer tripping. The results of the study are primarily obtained using the numerical Lattice-BOLTZMANN method as a computational aeroacoustic method, but are successfully validated randomly by measurements in an aeroacoustic wind tunnel.

The observed flow-induced noise is broadband with a case-dependent pronounced tonal component. As long as the aerodynamic load on the airfoil, i.e. the angle of attack, is comparatively low, a dominant tone exists with a sound pressure level that increases with the bluntness of the trailing edge. If the load is increased, the tone disappears and only broadband noise is present. The frequency of the tone decreases with the bluntness and increases with the REYNOLDS number. The criterion of BLAKE for the existence of a tone at blunt trailing edges turns out to be necessary but not sufficient. Already an analysis of the time-averaged velocity field shows that with increase of the bluntness a second vortex gradually develops in the near wake. The vortices alternately detach from the trailing edge and a vortex street is generated. Using methods of modal analysis, the flow field could be decomposed into coherent structures. One of these coherent structures, which is spatially and temporally resolved in detail, represents the vortex street described above. At high bluntness and comparatively low aerodynamic loading of the airfoil segment, the shed vortices are located close to the trailing edge. As the aerodynamic loading of the airfoil increases, the asymmetry of the flow between the suction- and pressure-side boundary layers becomes larger. As a result, even with comparatively blunt trailing edges, the vortices form further downstream from the trailing edge, which explains why the typical "blunt trailing edge" signature is absent.

ACKNOWLEDGMENT

This thesis was written during my time as a research assistant at the UNIVERSITY OF SIEGEN. My path began at the Institute of Fluid Mechanics and Thermodynamics (IFT), Department of Turbomachinery. First and foremost, I would like to express my sincere gratitude to my Doktorvater Prof. Dr.-Ing. Thomas Carolus, not only for his continuous support of my Ph.D. studies and related research but also for his patience and very thoughtful personal supervision even beyond his retirement. During my work at the IFT, I met Prof. Dr.-Ing. Sabine Roller and Prof. Marlène Sanjosé, Ph.D., both of whom played a very important role during my Ph.D. journey.

I was welcomed by my Doktormutter Prof. Dr.-Ing. Sabine Roller and her team at the Institute of Scientific Computing and Simulation Technique (STS) after Prof. Dr.-Ing. Thomas Carolus retired. Similar to the IFT in a working environment where curiosity, creativity, ethics, and teamwork were created and encouraged.

Since Prof. Dr.-Ing. Sabine Roller followed a call to the TECHNICAL UNIVERSITY OF DRESDEN, I decided to stay in Siegen, became a mother for the third time, and continued still under the supervision of Prof. Dr.-Ing. Sabine Roller. Besides this, I appreciated getting the opportunity to move to the IFT, Department of Fluid Mechanics to Prof. Dr.-Ing Holger Foysi and his team. Most of all, I am very grateful for the unique opportunity to perform experiments in the new aeroacoustic wind tunnel. Especially Alexander Bald and Dipl.-Ing. Bernd Homrighausen, who supported me in setting up and carrying out the experiments, should be mentioned.

The wind tunnel model was manufactured and equipped in the workshop of the Faculty of Technology at the UNIVERSITY OF SIEGEN, while the numerical simulations were conducted on the HorUS and Omni cluster at the university and the Niagara supercomputer at the SciNet HPC Consortium in Canada. I thank all employees of these facilities for the work done and their valuable advice and assistance.

Starting at events such as conferences and later at regular meetings, Prof. Marlène Sanjosé, Ph.D. consistently showed interest in my work, motivated and supported me through her expertise and fruitful discussions. In particular, I was extremely thankful for the opportunity to spend a five-month research stay at the ÉCOLE DE TECHNOLOGIE SUPÉRIEURE (ÉTS) Montreal, UNIVERSITÉ DU QUÉBEC, Canada, under the supervision of Prof. Marlène Sanjosé, Ph.D. It was a great and inspiring experience to work with her and her group and invaluable for me after the pandemic. Here I met Arnaud Le Floc'h, Ph.D. who encouraged me for the last part of my work and showed me the necessary tools. On this occasion, I would also like to express my gratitude to the German Academic Exchange Service (DAAD), for its financial support, which enabled this scientific stay abroad.

Throughout all these stations, I never lost a supervisor, instead, I always got one more, and am therefore, proudly grateful to have a whole Doktorfamilie.

At all these stations I always encountered a working group with great colleagues. I would like to express deep gratitude to Christine Krause, Dipl.-Ing. Bernd Homrighausen from the IFT as well as Bettina Lieberich and Peter Vitt from the STS, who were not just secretary and technical employees in the respective groups but the backbone of the team. Special thank goes to Dr.-Ing. K. Bamberger, Dr.-Ing. K. Volkmer, Dr.-Ing. N. Kaufmann, Dr.-Ing. C. Feldmann, Dr.-Ing. L. Mackowski, Dr.-Ing. F. Manegar, Dr.-Ing. H. Klimach, Dr.-Ing. N. Ebrahimi Pour, Dr.-Ing. K. Masilamani, Jana Gericke, Raphael Haupt, Alexander Bald, Arnaud Le Floc'h, Ph.D, Jorge Santamaria Osorio and Ahmadou Bamba Drame for the mental and emotional support, the constant sharing of the experience, and the great time. Especially the informal knowledge exchanges during our team-building activities or at the coffee table were of outstanding value to me. Furthermore thanks to all student assistants and graduates, who have accompanied and supported me throughout my research.

Finally, I would like to thank my family from the bottom of my heart, for their unconditional love and support.

To my daughters

Vivien, Leonie and Ida

CONTENTS

NOMENCLATURE

Symbols

a_n, a_k	temporal coefficient of mode n or k	[-]
c	chord length	[mm]
$\vec{c}_i$	velocity vector	[m/s]
c_b	chord length of baseline airfoil	[mm]
c_s	nondimensional speed of sound in lattice units	[-]
c_0	speed of sound	[m/s]
C	covariance tensor	[-]
C_d	drag coefficient	[-]
$C_i(\vec{x},t)$	collision operator	[kg/m³]
C_l	lift coefficient	[-]
C_p	pressure coefficient	[-]
C_μ	constant of LBM turbulence model	[-]
f	frequency	[Hz]
$f_i(\vec{x},t)$	particle distribution function	[kg/m³]
$f_i^{eq}(\vec{x},t)$	distribution function of thermodynamic equilibrium	[kg/m³]
f_s	sampling frequency	[Hz]
k	turbulent kinetic energy	[m²/s²]
l_z	spanwise correlations length of pressure fluctuations	[m]
l_f	distance between TE and first fully formed vortex	[mm]
L_{EXP}	segmented span of airfoil in experiment	[mm]
L_{LBM}	segmented span of airfoil in LBM simulation	[mm]
L_{ref}	reference span	[m]
L_{Spp}	level of the power spectral density of pressure	[dB]
Ma	MACH number	[-]
Ma_∞	freestream MACH number	[-]
p	pressure	[Pa]

p_0	standard reference pressure	[Pa]
R	distance between observer and source	[m]
R_{gas}	universal gas constant	[J/kg K]
Re	REYNOLDS number	[-]
R_{ref}	standard reference distance between observer and source	[m]
$R_{xy,coeff}$	normalized two-point cross-correlation	[-]
S_{fk}	cross-spectral density tensor	[-]
St	STROUHAL number	[-]
St_{TE}	STROUHAL number formed with a char. length of the airfoil geometry	[-]
St_{TE+BL}	STROUHAL number formed with a char. length of the airfoil geometry and the boundary layer displacement thickness	[-]
St_{wake}	STROUHAL number formed with a char. length of the airfoil wake	[-]
S_{xx}, S_{yy}	power spectral density	[Pa²/Hz]
S_{xy}	cross power spectral density	[Pa²/Hz]
t	time	[s]
t_{max}	maximum airfoil thickness	[mm]
$t_{trip,SS}$	tripping band thickness of the suction side	[mm]
$t_{trip,PS}$	tripping band thickness of the pressure side	[mm]
t_{TE}	trailing edge thickness	[mm]
t^*	trailing edge thickness-to-chord ratio (degree of bluntness)	[-]
T	period duration	[s]
TI	turbulence intensity	[-]
T_0	absolute temperature	[K]
T_{ac}	acoustic time	[s]
T_c	convective time	[s]
T_f	through-flow time	[s]
u	wall parallel velocity component	[m/s]
u_∞	free-stream velocity	[m/s]
u,v	cartesian velocity components	[m/s]

u^+	dimensionless velocity	[-]
$\vec{u}$	velocity vector of particles	[m/s]
U_e	edge velocity	[m/s]
$\vec{x}$	position vector	[m]
x, y, z	spatial coordinates	[mm]
X	field data for POD / SPOD	
y	distance to the wall	[m]
y_f	vertical distance between two inflection points	[mm]
y^+	dimensionless wall distance	[-]

Greek symbols

α	angle of attack	[°]
α_e	effective angle of attack	[°]
α_g	geometric angle of attack	[°]
γ^2	coherence function	[-]
δ	boundary layer thickness	[mm]
δ^*	boundary layer displacement thickness	[mm]
Δt	time step	[s]
ε	turbulent dissipation	[m²/s³]
η	spacing along spanwise coordinate	[mm]
$\tilde{\eta}$	parameter of LBM turbulence model	[-]
θ	boundary layer momentum thickness	[m]
λ	eigenvalue	[-]
φ	angle between the sloping surface and the TE of an airfoil	[°]
Φ_n	spatial mode n	[-]
ν	kinematic viscosity	[m²/s]
ρ	density	[kg/m³]
τ	relaxation time	[s]
τ_{eff}	effective relaxation time	[s]

τ_w	wall shear stress	[kg/m s²]
ϖ	weight function	[-]

Subscripts

avg	average
c	chord length
PS	pressure side
SS	suction side
tan	tangential component
TE	trailing edge
VS	vortex shedding

Superscripts

$\hat{\cdot}$	FOURIER transform
$\bar{\cdot}$	mean
$\cdot'$	fluctuating part
$\cdot*$	complex conjugate

Acronyms

BGK	BHATNAGER-GROSS-KROOK
BGN	back ground noise
BL	boundary layer
BP	bluntness parameter
BPM	BROOKS, POPE & MARCOLINI
BTE	blunt trailing edge
BTEN	blunt trailing edge noise
CAA	computational aeroacoustics
CAD	computer-aided design
CFD	computational fluid dynamics

DFT	discrete FOURIER transform
DNC	direct noise computation
EXP	experiment
FFT	fast-FOURIER transform
FW-H	FFOWCS WILLIAMS & HAWKINGS
GUI	graphical user interface
IFT	Institute for Fluid- and Thermodynamics
LBL	laminar boundary layer
LBL-VSN	laminar boundary layer vortex shedding noise
LBM	lattice-BOLTZMANN method
LE	leading edge
LES	large-eddy simulations
PDF	particle distribution functions
PIV	particle image velocimetry
POD	proper orthogonal decomposition
PS	pressure side
RANS	REYNOLDS-averaged NAVIER-STOKES
RNG	Renormalization Group
SPOD	spectral proper orthogonal decomposition
SS	suction side
SP	side plates
TBL	turbulent boundary layer
TBL-TEN	turbulent boundary layer trailing edge noise
TE	trailing edge
TEN	trailing edge noise
TKE	turbulent kinetic energy
VLES	very large eddy simulation
VS	vortex shedding
VR	variable resolution

1. Introduction

1.1 Motivation and objectives

Since the beginning of the aviation industry more than a century ago, airfoils have been aerodynamically investigated and improved. With the increasing proliferation of turbomachines such as propellers, fans, wind turbines, etc. the aerodynamically induced noise from airfoils became more and more important. Hence, during the last decades, the acoustics of lifting surfaces have been studied as well.

The aerodynamically induced noise from airfoils can be categorized into inflow noise and airfoil self-noise. Inflow noise is caused by the incoming turbulence impinging the leading edge. Mechanisms of self-noise are stochastic velocity fluctuations in the turbulent boundary layers above the wetted surfaces, boundary layer separation, vortex shedding, and turbulent wake at the trailing edge (TE). Trailing edge noise (TEN) is one of the dominant sources in applications like wind turbines where the inflow noise is small or even negligible [1].

BROOKS ET AL. [2] classified four principally different TEN generation mechanisms relevant for two-dimensional airfoil sections:

- Turbulent boundary layer/trailing edge noise (TBL-TEN); vortices generated in the unstable shear layer on both airfoil (suction and pressure) sides are convected over the TE into the wake; the TE acts as a scattering edge, the hydrodynamic pressure fluctuations are translated into noise.
- Separation-stall noise; is generated by a slightly separated boundary layer flow marked by large-scale flow structures compared to typical vortices within the turbulent boundary layer.
- Laminar boundary layer vortex shedding noise (LBL-VSN); is caused by unstable transition from laminar to turbulent flow.
- Blunt trailing edge noise (BTEN); is caused by finite thickness of the TE which produces a von Kármán-type quasi-periodic vortex shedding.

TEN in general has been the subject of a large number of investigations. The physical mechanisms, underlying TEN, have been investigated in numerous theoretical, numerical, and experimental studies - frequently dealing with a flat plate or a symmetric NACA0012 airfoil. Details including an overview of the present literature are given in Chapter 2 of this thesis. Blades for turbomachinery, however, are cambered and in most cases asymmetrical. Their trailing edges have to be thickened for manufacturing reasons. Hence, blunt trailing edge noise (BTEN) and its contribution to the overall TEN may be an issue.

It may be helpful to remember the textbook case of a flow around a smooth circular cylinder. A remarkable variation in the qualitative aspects of the field is observed from low to high

REYNOLDS numbers. Following, for instance, ANDERSON [3], the flow develops as follows: At very low values of *Re* the flow is of Stokes type with the streamlines symmetrical and attached. As *Re* is increased vortices are alternately shed in a regular fashion and flow downstream (Kármán vortex street). A further increase of *Re* causes the vortex street to become turbulent and to metamorphose into a distinct wake. Depending on *Re*, the upstream boundary layer becomes turbulent, which in turn affects the wake further.

It is the overall objective of this thesis to throw further light on the unsteady flow field in the vicinity of an airfoil trailing edge, the physical mechanisms involved in BTEN, and finally, the parameters affecting BTEN. Hence, important objectives of this thesis are:

- Studying BTEN in case of a state-of-the-art asymmetric airfoil (not a flat plate or a symmetric airfoil like NACA0012).
- Examining the impact of the trailing edge thickness and the boundary layer statistics on the unsteady flow field and eventually on TEN; in particular: What are the parameters for triggering, masking, or eliminating tonal BTEN?
- Evaluating the effect of aerodynamic loading of the airfoil to BTEN; loading means that the airfoil section is operated at increasing angles of attack, affecting the overall lift (and drag), the boundary layer, and potentially TEN/BTEN.
- Assessing the influence of the chord-based REYNOLDS number on BTEN.

Since the assumption of a fully turbulent boundary layer seems reasonable for blades of large wind turbines, this study of BTEN is confined to a fully turbulent boundary layer along the airfoil from leading to trailing edge.

1.2 Outline of the thesis

In Chapter 2, an overview of airfoil self-noise is given. Selected references reflecting the state-of-the-art concerning blunt trailing edge noise (BTEN) are summarized. Open questions concerning BTEN are worked out. Chapter 3 focuses on the methods utilized in the thesis for this new BTEN study. The base line airfoil and various configurations (especially with different trailing edges) are described in detail. The numerical and experimental methods chosen are described thoroughly. Since it is intended to identify vortical flow structures associated with the highly unsteady and tone-generating trailing edge flow, methods like proper orthogonal decomposition (POD) and spectral proper orthogonal decomposition (SPOD) are explained. Chapter 4 deals with a basic verification of the numerical method, e.g. a mesh-independence study, and the principal validation with experimental results. Chapter 5 describes the results, mainly based on the numerical simulation. One highlight of this thesis is the application of proper orthogonal decomposition (POD) and spectral proper orthogonal de-

composition (SPOD) to the flow field data. In Chapter 6 the results are summarized, discussed, and final conclusions are drawn.

2. Blunt Trailing Edge Noise (BTEN): Literature review

2.1 Prelude: Classification of airfoil self-noise

Studies on the aeroacoustics of two-dimensional airfoil sections deal with one or more of the four self-noise mechanisms:

- Turbulent boundary layer/trailing edge noise (TBL-TEN)
- Separation-stall noise generated by a slightly separated boundary layer flow
- Laminar boundary layer vortex shedding noise (LBL-VSN)
- Blunt trailing edge noise (BTEN)

These mechanisms will now be briefly described. For this, the respective flow fields are presented in Figure 2.1.

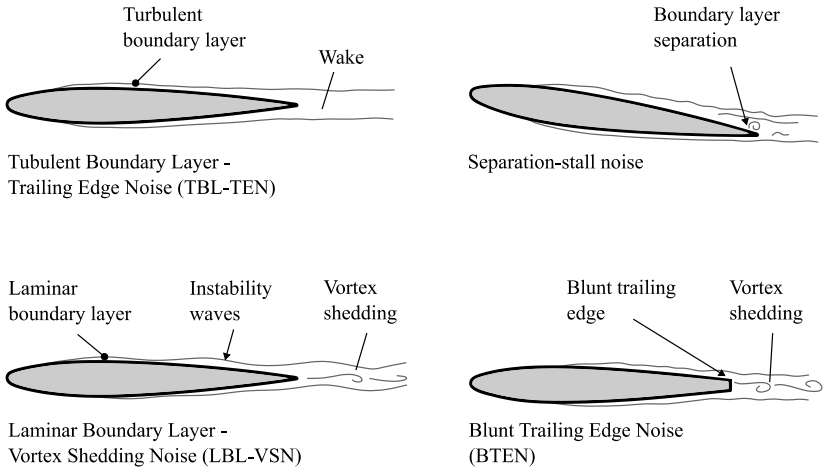

Figure 2.1: Airfoil self-noise mechanisms, adapted from BROOKS [2].

TBL-TEN occurs when the convective turbulence from the turbulent boundary layer of both airfoil sides passes the trailing edge and reaches the wake. TBL-TEN is of broadband nature.

Separation-stall noise generated by an even slightly separated boundary layer flow is marked by large-scale flow structures as compared to typical small-scale vortices within the TBL. FINK & BAILEY [4] showed that due to stall the noise can increase up to 10 dB. For a mildly separated flow, noise is still emitted from the TE and is of dipole nature. The acoustic signatures are humps in the low-frequency range. MOREAU ET AL. demonstrated that for deep stall

the TBL-TEN broadband noise feature appears as well and is additionally characterized by narrow peaks which can be associated with shear layer instabilities and large-scale vortex shedding [5]. PATERSON stated that in case of deep stall, the noise is radiated from the whole chord and hence cannot no longer be named TEN [6].

Furthermore, noise can occur due to vortex shedding (VS). The occurrence of VS can be caused either by blunt trailing edges (BTEs) or by laminar boundary layer vortex shedding (LBL-VS) instabilities. Both result in noise (LBL-VSN), which is tonal or less broadband in nature and sometimes perceived as a loud, annoying whistling. In case of LBL-VSN, FINK, PATERSON, TAM, and YAKHINA agree on the existence of an acoustic feedback loop that amplifies the boundary layer instabilities at certain frequencies [7 - 10]. LBL-VSN tones can be easily suppressed by forcing the transition to turbulence e.g. by tripping (or increasing the REYNOLDS number). Owing to the fact that a laminar boundary layer has to be present, this noise mechanism is associated with low to medium values of the chordwise REYNOLDS number.

Some studies on *blunt* trailing edge noise (BTEN) are summarized in more detail in the next section.

2.2 BTEN: Common parameters and definitions

Figure 2.2 shows examples of lifting surfaces with typical trailing edges. Besides the shape of the airfoil or plate, essential geometric parameters are the (airfoil) chord length c and the trailing edge thickness t_{TE}. Their geometry as well as the aerodynamic and aeroacoustic phenomena apparent when operated in a flow are frequently described in terms of non-dimensional parameters, see also Figure 2.3. Due to the importance of these parameters, their definition in the present work is as follows:

Trailing edge thickness-to-chord ratio. This purely geometric ratio is sometimes also called the “degree of bluntness”. It is defined as

$$t^* \equiv \frac{t_{TE}}{c}. \tag{2.1}$$

Bluntness parameter. In contrast to the degree of bluntness, this ratio involves a parameter characterizing the (boundary layer) flow:

$$BP \equiv \frac{t_{TE}}{\delta^*_{avg}}, \tag{2.2}$$

with δ^*_{avg} being the averaged boundary displacement thickness close to the trailing edge on the suction and pressure side

$$\delta^*_{avg} = \frac{\delta^*_{SS} + \delta^*_{PS}}{2}. \tag{2.3}$$

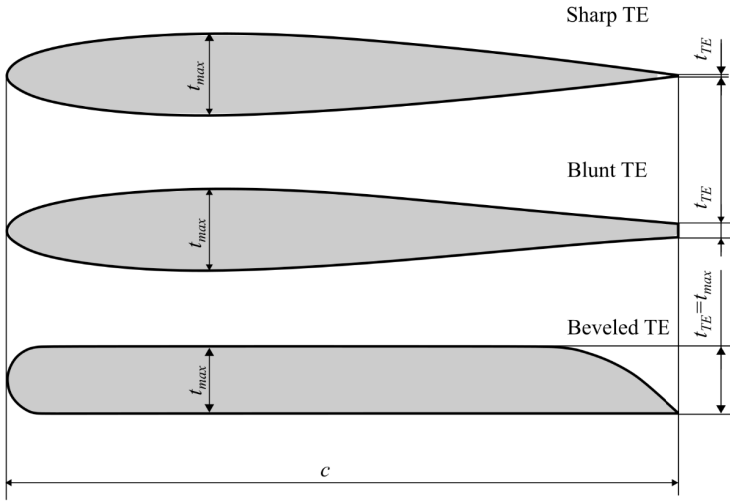

Figure 2.2: Geometry of lifting surfaces with typical trailing edges.

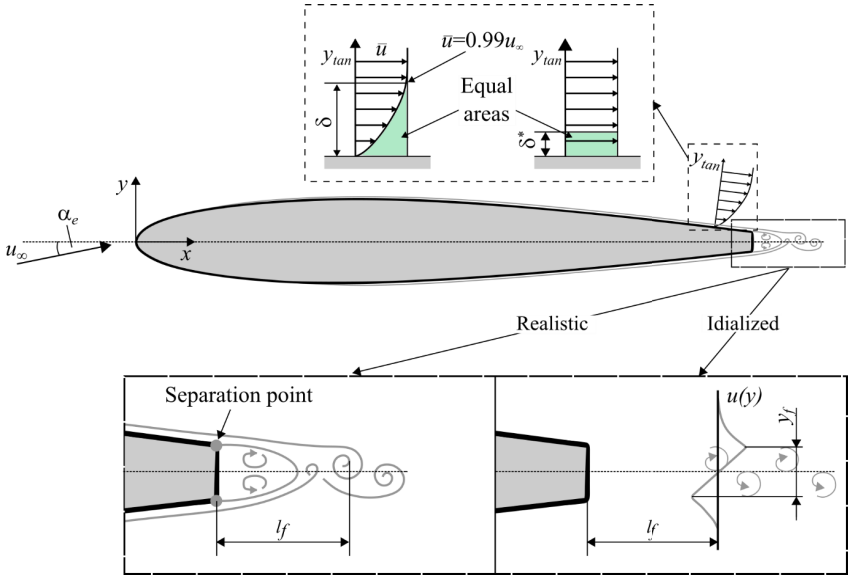

Figure 2.3: Boundary layer and vortex structure downstream of the trailing edge of a lifting surface (schematically), adapted from BLAKE [11].

REYNOLDS number. Two definitions are common:

$$Re_c \equiv \frac{u_\infty c}{\nu} \text{ and} \tag{2.4a}$$

$$Re_{TE} \equiv \frac{u_\infty t_{TE}}{\nu}, \tag{2.4b}$$

with the airfoil chord length c or the trailing edge thickness t_{TE} as the characteristic length, the free-stream velocity u_∞ , and the kinematic viscosity ν of the free-stream.

STROUHAL number. In the case of cylinders, St characterizes the vortex shedding (VS) frequency and is merely a function of the REYNOLDS number. For lift-producing surfaces, however, this is not as trivial. Various characteristic lengths may be utilized: Either the purely geometric trailing edge thickness t_{TE}, the trailing edge thickness t_{TE} augmented by the boundary layer displacement thicknesses at the suction and pressure side δ^*_{SS} and δ^*_{PS}, respectively, or the distance between the two inflection points y_f in the velocity profile of the wake; this distance is determined downstream of the TE at l_f where the velocity fluctuations reach their maximum, which is the location of the first fully formed vortices. Anticipating vortex shedding with an oscillatory wake and tonal BTEN, the corresponding STROUHAL numbers are:

$$St_{TE} \equiv \frac{f_{VS} l_1}{u_\infty} \text{ with } l_1 \equiv t_{TE} \text{ or} \tag{2.5a}$$

$$St_{TE+BL} \equiv \frac{f_{VS} l_2}{u_\infty} \text{ with } l_2 \equiv t_{TE} + \delta^*_{SS} + \delta^*_{PS} \text{ or} \tag{2.5b}$$

$$St_{wake} \equiv \frac{f_{VS} l_3}{u_\infty}, \; l_3 \equiv y_f, \tag{2.5c}$$

where f_{VS} is the VS frequency and u_∞ the free-stream velocity.

Normalization of levels. Targeting a more universal representation of the levels, characteristic parameters are required for non-dimensionalization. A most recent approach is due to HERR [12] in terms of the free stream MACH number and ratio of length scales

$$L_{Spp,norm} = L_{Spp} - 50\log\left(Ma_\infty\right) - 10\log\left(\frac{l_2}{l_1}\right). \tag{2.6}$$

In principle, utilization of other length scales is possible.

2.3 BTEN: Selected literature

An early and frequently quoted semi-empirical correlation between the bluntness parameter BP of a NACA 0012 airfoil at Re_c=3·10^6 and the acoustically relevant vortex shedding frequency was given by BROOKS, POPE, and MARCOLINI as part of their “BPM”-model [2]:

$$St_{VS} = \begin{cases} 0.1BP & for \quad BP < 0.2 \\ \dfrac{0.212 - 0.0045\varphi}{1 + 0.235BP^{-1} - 0.0132BP^{-2}} & for \quad BP \geq 0.2 \end{cases} \tag{2.7}$$

In the BPM-model, the characteristic STROUHAL number is assumed to depend on the *BP* as well as the angle φ between the sloping surface upstream of the TE and the face of the blunt TE. For the edge of a flat plate $\varphi = 0°$, whereas in case of a NACA 0012 airfoil $\varphi = 14°$. The effect of the angle of attack α_e is only considered indirectly via its effect on the boundary layer displacement thickness that is per definition included in *BP*. The BPM-model assumes BTEN to contribute in an additive manner to the total TEN.

A pioneering work on BTEN was published by BROOKS & HODGSON [13] who investigated vortex shedding noise from a symmetric airfoil (NACA 0012) at Re_c ranging from 0.9 to $3 \cdot 10^6$ and thickness-to-chord ratios t^* ranging from 0.18 to 0.41 at zero lift condition. Depending on t^*, spectral peaks were observed evolving as an additive contribution to the self-noise from the sharp edge airfoil. The contribution is a spectral peak at the same frequency as the fluctuating surface pressures measured in the vicinity of the TE.

BLAKE [11] correlated BROOKS & HODGSON's data as well as further hot wire measurements in the wake of a flat plate by CHEVRAY & KOVASZNAY [14] with the bluntness parameter *BP*. According to his finding, no vortex shedding can be expected for $BP < 0.3$ and certainly not for < 0.05. Shedding did occur, however, for $BP > 0.3$ and certainly > 0.5. BLAKE underpins this with the findings by BROOKS & HODGSON as depicted in Figure 2.4.

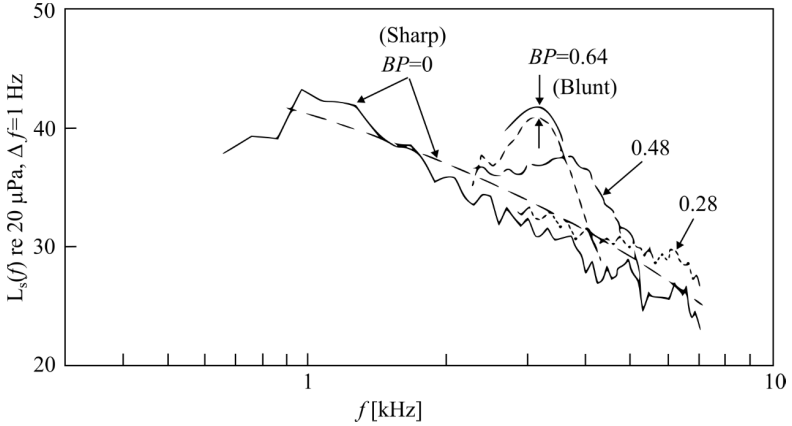

Figure 2.4: Radiated noise for sharp and BTE of a NACA 0012 at $Re_c = 2.8 \cdot 10^6$; after BLAKE [11].

He further showed that with decreasing *BP* the humps of the BTEN broaden and eventually diminish. The coherent shedding at the BTE causing this effect appears to correspond to a STROUHAL number value $St_{TE} = 0.1$.

In [15] HUTCHESON & BROOKS presented measurements from a NACA 63-215 airfoil model with different trailing edge configurations. Spectra and directivity for clean and tripped boundary layer surface treatments were examined only for one single value of Re_c=1.7·10^6 and one airfoil geometric angle of attack α_g = -1.2° (zero lift condition). Later on, HUTCHESON & BROOKS extended this study in [16] to examine the effect of *Re* and angle of attack on TE noise with different blunt trailing edges. Either square or rounded corners were applied to the trailing edge of the airfoil and the thickness-to-chord ratio was varied from $t^* = 0.03$ to 0.8. The test condition comprised values of Re_c from 0.6 to 1.6·10^6 and geometric angles of attack α_g ranging from -6.2° to 8.8°. Besides the experiments, the BPM-model was applied to help interpreting the data. The main findings of this study can be summarized as follows: With increasing angle of attack, the spectral hump of TBL-TEN increases in level and shifts to lower frequencies, whereas the BTEN peak level decreases but does not change in frequency. As the flow velocity is increased, BTEN and TBL-TEN increase in level and shift to higher frequencies as well. With increasing trailing edge thickness-to-chord ratio the level of the BTEN peak increased and shifted to lower frequencies. A rounded trailing edge broadens the spectral peak. The characteristic value of STROUHAL number $St_{TE} = 0.1$ was confirmed. As in BROOKS & HODGSON [16] the authors consider the overall noise to be a superposition of the TBL-TEN and BTEN.

In 2008 BARONE & BERG [17] published a study about BTE airfoils with the goal to improve performance and noise emission. For this, they attached a so-called splitter plate to the trailing edge, which had a length equal to the TE thickness t_{TE}, as seen in Figure 2.5. The airfoil investigated was a thick cambered airfoil (DU97W300) with a trailing edge-thickness-to-chord ratio $t^* = 0.1$. Acoustic far-field wind tunnel measurements were conducted for a high REYNOLDS number flow and various angles of attack. Besides the aerodynamic performance increase and the noise reduction due to the splitter plates, the vortex shedding frequency in case of the untreated baseline airfoil was found at $St_{TE} = 0.24$. Independent of the TE configuration increasing the angle of attack from 4° to 11° reduced the VS peak noise power level by about 4 dB with unchanged narrowband characteristics.

Figure 2.5: Wind tunnel model with splitter plate attached from BERG & ZAYAS [18].

In the same year, BERG & ZAYAS [18] published a similar study to quantify the noise generated by BTE airfoils, again with TE splitter plates. This time, the acoustic results covered not only the low-frequency range where the VS peak is located but also high frequencies. It was obvious that in the low-frequency range left from the VS peak, all configurations (sharp, blunt, and treated TE) exhibited the same characteristics. For the frequency range beyond the VS peak, the BTE version provided a higher noise contribution.

Other scientists like BILKA, LEW, SHANNON, VAN DER VELDEN, and WU [19 - 28] focused on the acoustic emission of the flat plate with a beveled TE, the so-called "Blake airfoil". SHANNON and SHANNON ET AL. [24 - 27] investigated experimentally the far field noise employing a phased array and the flow field in the near wake region by using PIV at $Re_c = 1.9 \cdot 10^6$ and 0° geometric angle of attack α_g. Spatially resolved velocity data collected in the near wake of a trailing edge have revealed the presence of an asymmetric von Kármán wake instability. By phase averaging with respect to VS, it was shown that VS is responsible for tonal and broadband noise. The corresponding value of the STROUHAL number St_{wake} was found to be 0.184.

Later, LEW ET AL. [23] performed numerical investigations under the same conditions as SHANNON [24 - 27] and compared their results with the findings of SHANNON. The numerical method applied was a Lattice-BOLTZMANN Method (LBM) with the Very Large Eddy Simulation (VLES) approach, combined with the FFOWCS-WILLIAMS and HAWKINGS (FW-H) analogy to predict the far-field noise. The predicted vortex shedding frequency showed good agreement as compared to the experimental data (215 Hz vs. 219 Hz). However, the value of STROUHAL number $St_{wake} = 0.14$ associated with VS deviated from the experimentally determined value of 0.184. The mean magnitudes of the tonal peak showed the correct trends, but the LBM results did not correctly predict the measured peak values. The authors argued that the discrepancies were due to the different setups in the experiment (open jet) and their simulation (free field), mesh setup, flow conditions, and possibly due to insufficient convergence statistics.

BILKA ET AL. [22] studied the beveled plate and varied the ratio of the boundary layer momentum thickness θ to TE thickness t_{TE} at constant Re_c. PIV measurements indicated distinct differences in the near-wake flow field that were then related to the far-field noise. The near-wake of the largest value of t_{TE}/θ showed coherent, periodic shedding of vorticity in the near-wake, which resulted in a very narrowband tone in the radiated noise spectra. The two cases with smaller t_{TE}/θ showed lower unsteadiness levels and more random, incoherent vorticity in the near-wake. As a result, the radiated noise was considerably higher than what one would expect from the scattering of the approaching boundary layer - but still broadband, and lower than expected from the vortex-shedding case.

WU ET AL. [28] developed a hybrid method for aerodynamic noise prediction based on a discrete vortex model and acoustic perturbation equations. For this, a flat plat with a straight TE and different trailing edge thickness-to-chord ratios $t^* = 0.013$, 0.026, and 0.052 were tested at zero angle of attack. A comparison of the simulated sound pressure level between exper-

imental and theoretical results from ROGER & MOREAU and ROGER ET AL. [29, 30] and the noise prediction of the semi-empirical BPM-model [2] were carried out. The shedding frequency calculated was very close to the measured values with only a difference of 52 Hz. The BPM-model predicted peak agreed as well in frequency but gave too high sound pressure level for the vortex shedding noise. Depending on the BTE thickness the frequency for the vortex shedding was found at a STROUHAL number of $St_{TE} = 0.21$.

VAN DER VELDEN ET AL. [19 - 21] reported the application of a Lattice-BOLTZMANN method for the analysis of TEN from a beveled plate. The acoustic prediction was obtained via the FFOWCS WILLIAMS & HAWKINGS aeroacoustic analogy in the far-field and direct probes in the near-field. The flow field data were compared with PIV measurements. The unsteady flow field prediction agreed well with the experiments. The shedding frequency was correctly captured. The probes in the near-field overestimated somewhat the higher frequency range as compared to experimental data.

HERR AND HERR & DOBRZYNSKI [12, 31, 32] investigated experimentally in an aeroacoustic wind tunnel a flat plate with different trailing edge thicknesses. Their interest was in TEN mitigation measures and scaling laws of TEN. A special feature of the flat plate configuration was an exchangeable center with which different chord lengths were realized. Results for Re_c from 2.1 to $7.9 \cdot 10^6$ and $t^* = 0.00025$ to 0.003 were obtained. The BTEN contributions were found at a characteristic STROUHAL number value $St_{TE} = 0.1$. In contrast to former results from BROOKS & HODGSON and HUTCHESON & BROOKS [15, 16, 33] a significant noise contribution from the trailing edge was found, even for the range of the bluntness parameter $BP < 0.3$, where it has not been expected. BROOKS & HODGSON [33] showed that BTE humps broadened and finally disappeared with decreasing t^*. This was not confirmed by HERR's results for the plate configurations. HERR & DOBRZYNSKI reasoned that the broadening of TEN spectra with decreasing TE thickness as seen by BROOKS & HODGSON origins from a reduced coherence of the turbulent pressure rather than from a change of boundary layer thickness or the bluntness parameter [32].

In addition to the flat plate, HERR AND HERR & DOBRZYNSKI [12, 31, 32] studied the symmetric NACA 0012 airfoil section at Re_c from 1.1 to $1.6 \cdot 10^6$ and $t^* = 0.000375$ to 0.0025. Unlike to the flat plate study of HERR and HERR & DOBRZYNSKI, here the bluntness parameter BP is a valid indicator of the occurrence of BTEN. It is worth noting, however, that this is mainly based on the NACA 0012 study by BROOKS & HODGSON [2]. The VS frequencies were found to scale on a characteristic STROUHAL number $St_{TE+BL} = 0.1$. Moreover, HERR rejected the earlier hypothesis that BTEN is additive in nature, BTEN is not an independent additive to the overall trailing edge noise signature. HERR suspects that the vortex shedding in the wake affects the turbulent energy cascade in the boundary layer upstream.

GARREC ET AL. [34] investigated a NACA 0012 airfoil at high REYNOLDS number, i.e. $Re_c = 2.32 \cdot 10^6$ and an effective angle of attack α_e of 2.5°. The main objective was to evaluate a direct noise computation (DNC) method to simulate the noise mechanisms identified by BROOKS. To save computational effort, an in-house developed multi-mesh multi-time-step al-

gorithm was used. Although this is a promising method, the results did not agree with given experimental data. A substantial difference in the VS frequency as well as in level had been found. The authors concluded that an improvement in the results could be expected with a longer simulation time and hence the fundamental mean flow prediction.

Two more recent examples of a refinement of the early semi-empirical BPM-model are due to KIM ET AL. [35] and ZHU ET AL. [36]. Both efforts did not yield consistently better results as compared to experiments.

2.4 Intermediate conclusions

The problem of predicting blunt trailing edge noise has been investigated intensively. Predominantly, the flat plate and the symmetrical NACA 0012 airfoil had been studied in the past, but only very few airfoil shapes were close to a practical application, requiring camber and a blunt trailing edge, among other features. In addition, many of the authors had limited their study to zero lift condition which is far away from applications in turbomachinery like for instance wind turbines. The few studies, however, which varied the angle of attack and hence "aerodynamic" loading proved that loading can have a strong effect on BTEN. The methods employed range from experimental, semi-analytical, and - more recently - sophisticated computational methods of aeroacoustic. Among the numerical methods, the Lattice-BOLTZMANN method (LBM) seems promising in representing the unsteady complex flow field in the trailing edge region, and simultaneously, because of the low Mach number application, the acoustic field.

As a consequence, this thesis is concerned with an asymmetric airfoil, here the cambered airfoil DU93W210, developed by TIMMER AND VAN ROOIJ [37] at the TECHNICAL UNIVERSITY OF DELFT for modern wind turbines. To examine the impact of trailing edge thickness and identify parameters triggering, masking, or eliminating BTEN, the trailing edge is gradually truncated from sharp to blunt during the course of this study. In addition, different REYNOLDS numbers will be realized for this purpose by varying the inflow velocity. The maximum value of Re_c is fixed to $1.2 \cdot 10^6$. As most applications of turbomachinery are characterized by high REYNOLDS numbers and associated turbulent boundary layers, the study is confined to the case of fully turbulent boundary layers on both, pressure and suction side of the section which are achieved by boundary layer tripping. For variation of the loading, the effective angle of attack of the airfoil section is varied. Two methods are selected for this study: (i) High-fidelity simulations of the flow and acoustics with a Lattice-BOLTZMANN method and (ii) experiments in an aeroacoustic wind tunnel.

3. Methods for the present BTEN-Study

This chapter compiles information on the subject matter and methods of the present blunt trailing edge noise study conducted within this thesis. It contains information about the airfoil studied, including the different geometries of the trailing edge and other varied parameters, such as the REYNOLDS number and the angle of attack. Finally, an "experimental" plan is prepared for both the numerical simulations and the experimental studies of the flow and sound field. The numerical Lattice-BOLTZMANN Method (LBM) is briefly summarized, followed by a description of the numerical setup and details of the computational domain and boundary conditions. The aeroacoustic wind tunnel used in this study at the UNIVERSITY OF SIEGEN and the experimental test case are presented. Finally, the unified evaluation of the numerical and experimental data is described.

3.1 Airfoil and parameters varied

The complete study is based on the DU93W210 airfoil. It has been developed by TIMMER and VAN ROOIJ [37] at the TECHNICAL UNIVERSITY OF DELFT, originally for the mid-blade region of large wind turbine rotors.

The denotation DU*yy*W*xxx* DU is as follows: DU stands for DELFT UNIVERSITY, *yy* for the year of development, W for the wind energy application area, and the last three digits *xxx* correspond to ten times the maximum thickness *t* of the airfoil, based on the airfoil chord. Hence, the DU93W210 has a maximum thickness of 21% of the chord length. As depicted in Figure 3.1 the DU93W210 is a cambered airfoil with a partly concave pressure side. This original airfoil has a trailing edge-thickness-to-chord ratio $t^* = 0.005$ and is taken as the baseline geometry in this study. Hence, the chord length of the baseline geometry is referred to as c_b. In order to obtain three different blunt trailing edges, the original airfoil has been truncated in three steps. Truncation always implies that the effective chord length c becomes shorter than the baseline c_b.

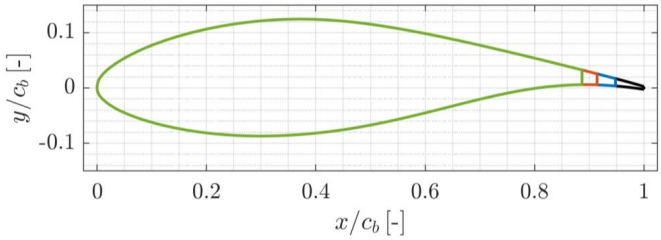

Figure 3.1: DU93W210 airfoil (baseline with $t^* = 0.005$, black) and three blunt trailing edges ($t^* = 0.014$, blue, $t^* = 0.022$, red, $t^* = 0.030$, green); t^* is always defined with the effective chord c of the truncated airfoil.

It is important to note that the trailing edge-thickness-to-chord ratio t^* and the REYNOLDS number are always defined with the effective chord length c of the (truncated) airfoil. The variation of aerodynamic loading is achieved via three effective[1] angles of attack, of $\alpha_e = 0°$, 1.5° and 3.5°. Finally, the REYNOLDS number is varied, by setting the free-stream velocity to $u_\infty = 30$ m/s and 60 m/s. For the present study, the chord length of the baseline airfoil is chosen as 300 mm. Table 3.1 compiles the values of the dimensional as well as non-dimensional parameters. The MACH number *Ma* is mentioned for information only, it is considered as an irrelevant parameter within this study.

3.2 Boundary layer tripping

As initially stated this study is confined to the case with the boundary layer over the most part of the airfoil section pressure and suction side being turbulent. For both, the numerical simulation and the experiments, this requires careful tripping. Since the angle of attack is varied during the study, and the airfoil itself is also asymmetrical, the tripping positions have been chosen differently. Boundary layer tripping was applied close to the leading edge using a zig-zag tripping band on the suction side at $x/c_b = 0.02$ and on the pressure side at $x/c_b = 0.05$, see Figure 3.2.

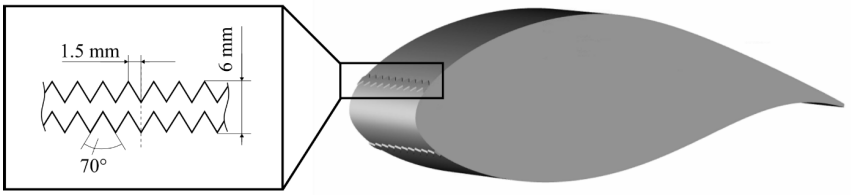

Figure 3.2: Sketch of tripping on pressure and suction side of the airfoil section DU93W210 with a chord length of 300 mm.

The challenge was to ensure transition close to the leading edge for all operation conditions but without overtripping. Overtripping would prevent the boundary layer from developing similarly to a "natural" turbulent boundary layer. Thus, if the tripping band is too thick, the boundary layer thickness will be higher than the naturally formed boundary layer. For this reason, simulations were carried out with different tripping band thicknesses which are reported in Appendix A. Tripping were implemented both in the experiment and in the Lattice-BOLTZMANN (LBM) simulation. Table 3.2 provides information on the tripping band thicknesses selected for each case for suction and pressure sides for experiment and simulation.

[1] The definition of the effective angle of attack is given in Appendix B.

Table 3.1: Parameters for simulation and experiment. Cases marked with $^{+}$ have been simulated only (for a better overview ./. indicates that the parameter has not been changed with respect to the previous line).

Case	t_{TE} [mm]	c [mm]	α_e [°]	u_∞ [m/s]	t^* [-]	c/c_b [-]	$Re_c \cdot 10^{-6}$ [-]	$Re_{TE} \cdot 10^{-3}$ [-]	Ma [-]
I	1.5	300	0	30	0.005	1.000	0.6	3.1	0.087
II	./.	./.	1.5	./.	./.	./.	./.	./.	./.
III	./.	./.	3.5	./.	./.	./.	./.	./.	./.
IV	./.	./.	0	30	./.	./.	1.2	6.2	0.175
V	./.	./.	1.5	./.	./.	./.	./.	./.	./.
VI	./.	./.	3.5	./.	./.	./.	./.	./.	./.
VII	4.0	284	0	30	0.014	0.947	0.6	8.2	0.087
VIII^{+}	./.	./.	1.5	./.	./.	./.	./.	./.	./.
IX	./.	./.	3.5	./.	./.	./.	./.	./.	./.
X	./.	./.	0	60	./.	./.	1.2	16.4	0.175
XI^{+}	./.	./.	1.5	./.	./.	./.	./.	./.	./.
XII	./.	./.	3.5	./.	./.	./.	./.	./.	./.
XIII^{+}	6.0	274	0	30	0.022	0.913	0.6	12.3	0.087
XIV^{+}	./.	./.	1.5	./.	./.	./.	./.	./.	./.
XV^{+}	./.	./.	3.5	./.	./.	./.	./.	./.	./.
XVI^{+}	./.	./.	0	60	./.	./.	1.1	24.6	0.175
XVII^{+}	./.	./.	1.5	./.	./.	./.	./.	./.	./.
XVIII^{+}	./.	./.	3.5	./.	./.	./.	./.	./.	./.
XIX	8.0	266	0	30	0.030	0.867	0.5	16.4	0.087
XX	./.	./.	1.5	./.	./.	./.	./.	./.	./.
XXI	./.	./.	3.5	./.	./.	./.	./.	./.	./.
XXII	./.	./.	0	60	./.	./.	1.1	32.9	0.175
XXIII	./.	./.	1.5	./.	./.	./.	./.	./.	./.
XXIV	./.	./.	3.5	./.	./.	./.	./.	./.	./.

Table 3.2: Tripping band thickness selected for suction and pressure side of the airfoil for LBM simulation and experiment.

Case	*LBM*		*EXP*	
	$t_{trip,SS}$ [mm]	$t_{trip,PS}$ [mm]	$t_{trip,SS}$ [mm]	$t_{trip,PS}$ [mm]
I	0.9	0.7	0.6	0.7
II	0.7	0.7	0.6	0.7
III	0.7	0.8	0.6	0.7
IV	0.8	0.7	0.6	0.7
V	0.7	0.7	0.6	0.7
VI	0.6	0.8	0.6	0.7
VII	0.9	0.7	0.4	0.7
VIII	0.7	0.7	-	-
IX	0.7	0.8	0.4	0.7
X	0.7	0.7	0.4	0.7
XI	0.7	0.7	-	-
XII	0.6	0.7	0.4	0.7
XIII	0.9	0.7	-	-
XIV	0.7	0.7	-	-
XV	0.7	0.7	-	-
XVI	0.7	0.7	-	-
XVII	0.7	0.7	-	-
XVIII	0.7	0.7	-	-
XIX	0.9	0.7	0.6	0.7
XX	0.7	0.7	0.6	0.7
XXI	0.7	0.8	0.6	0.7
XXII	0.8	0.7	0.6	0.7
XXIII	0.7	0.7	0.6	0.7
XXIV	0.6	0.7	0.6	0.7

3.3 Numerical methodology and case setup

In this section, the fundamentals of the Lattice-BOLTZMANN method (LBM) are briefly summarized. Since the LBM in the implementation of the commercial code PowerFLOW™ Release 6-2020-R1[38] is utilized, the general simulation procedure, the program-specific generation of the numerical grid, and some peculiarities of the physical modeling are outlined. Finally, the setup of the simulation case is presented.

The introduction given in this section is mainly based on the textbooks by KRÜGER [39] and GU and SHU [40]. In contrast to classical continuum mechanics, involving solving the nonlinear partial differential NAVIER-STOKES equations, the Lattice-BOLTZMANN method (LBM) is based on a gas kinetic approach, utilizing a discrete form of the BOLTZMANN equation. The flow is considered on a mesoscopic level which is based on a molecular perspective. Instead of following the movement of each molecule (microscopic approach), a statistical description is used. The basic quantity of LBM is the discrete-velocity distribution function $f_i(\vec{x},t)$, which represents the probability to encounter a number of fluid particles with a certain velocity $\vec{c}_i = (c_{xi}, c_{yi}, c_{zi})$ at a certain position *x* and time *t*. For each distribution function, the BOLTZMANN equation is solved on a numerical mesh, known as a lattice. This is realized in a simple efficient numerical scheme consisting of a local collision and a streaming step to the neighbors. The BOLTZMANN equation is a nonlinear integro-differential equation for the distribution function *f* and its derivation is based on the conservation of particles in phase space. For a detailed description of the derivation, the reader is referred to the textbook by KRÜGER [39]. The Lattice-BOLTZMANN equation itself has the form:

$$f_i(\vec{x}+\vec{c}_i\Delta t, t+\Delta t) - f_i(\vec{x},t) = C_i(\vec{x},t). \tag{3.1}$$

The left-hand side of equation 3.1 describes the streaming process and contains the temporal and convective change of the distribution function. The right side describes the collision and hence the change of the distribution function due to collisions of the fluid particles and is called the collision operator C_i. Since the collision operator is composed of a complex integral, it is approximated. The solver applied in this work models the collision term with the well-known BHATNAGAR-GROSS-KROOK (BGK) approximation [41] which assumes that every non-equilibrium state targets an equilibrium state. Accordingly, the collision term is defined as follows:

$$C_i(\vec{x},t) = -\frac{\Delta t}{\tau}\left[f_i(\vec{x},t) - f_i^{eq}(\vec{x},t)\right], \tag{3.2}$$

where τ is the viscous relaxation time, which is related to the fluid kinematic viscosity and speed of sound. f^{eq} is the MAXWELL-BOLTZMANN equilibrium distribution function.

To solve these equations efficiently, they are discretized onto a three-dimensional cubic lattice, named stencil, with predetermined discrete directions comprising a discrete velocity space, denoted using the abbreviation D*d*Q*q*. Where *d* is the number of spatial dimensions the

stencil covers and q is the number of discrete velocities. Here, the three-dimensional stencil D3Q19 is applied. This stencil discretizes the velocity space into 19 discrete velocities as shown in Figure 3.3.

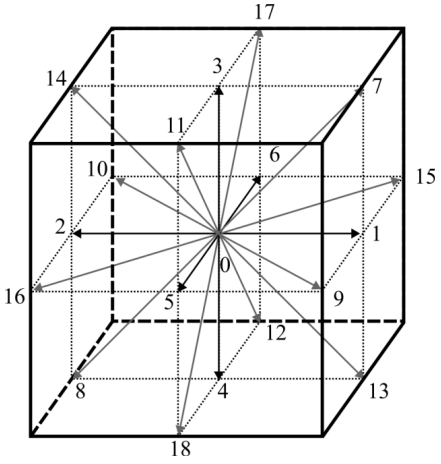

Figure 3.3: D3Q19 Stencil.

The need for 19 velocities arises from the requirement of sufficient lattice symmetry to ensure the recovery of the NAVIER-STOKES equations, FRISCH ET AL. [34]. To obtain macroscopic hydrodynamics, the equilibrium distribution function f^{eq} must be chosen to satisfy the conservation laws (mass, momentum, etc.[19]). Here, f^{eq} is approximated, for low MACH numbers, by a second-order expansion onto a Hermite polynomial basis [19]:

$$f_i^{eq}\left(\vec{x},t\right)=\rho\overline{\omega}_i\left[1+\frac{\vec{c}_i\vec{u}}{c_s^2}+\frac{(\vec{c}_i\vec{u})^2}{2c_s^4}-\frac{\vec{u}\cdot\vec{u}}{2c_s^2}\right], \tag{3.3}$$

where $\overline{\omega}_i$ are weighting parameters specific to the chosen stencil and c_s the non-dimensional speed of sound in lattice units with a value of $1/\sqrt{3}$.

Before calculating the collision step (3.2) or after solving the streaming step the velocity distribution functions f_i are obtained on each mesh point from different directions. From these distributions, the flow variables of interest are calculated as moments of these distributions. Since these distributions are only discrete, the integral over all velocities is replaced by the sum over all discrete velocities. As an example, the following equations show the moments for the calculation of density and velocity at the macroscopic level:

$$\rho\left(\vec{x},t\right)=\sum_i f_i\left(\vec{x},t\right), \tag{3.4}$$

$$\rho\vec{u}\left(\vec{x},t\right)=\sum_i \vec{c}_i f_i\left(\vec{x},t\right)\cdot \tag{3.5}$$

The link between the Lattice-BOLTZMANN and the NAVIER-STOKES equations can be established by using the CHAPMAN-ENSKOG analysis [42]. For small MACH numbers, the Lattice-BOLTZMANN equation leads to a macroscopic behavior similar to that of the NAVIER-STOKES equations, where the kinematic shear viscosity v is given by the relaxation time τ as:

$$\tau=\frac{\nu}{c_s^2}+\frac{\Delta t}{2}. \tag{3.6}$$

c_s^2 is the non-dimensional speed of sound in lattice units.

In this work, the LBM has been used with a Very Large-Eddy Simulation (VLES) turbulence model which models the unresolved scales of turbulence. Turbulence modeling is incorporated directly into the BOLTZMANN BGK equation by modifying the relaxation time τ to τ_{eff} in the collision operator to give an extended relaxation time scale [40, 43]. τ_{eff} is derived from a systematic Renormalization Group (RNG) theory [44] as

$$\tau_{eff}=\tau+C_\mu\frac{k^2/\varepsilon}{(1+\tilde{\eta}^2)^{1/2}}, \tag{3.7}$$

where k is the turbulent kinetic energy, ε the dissipation, $C_\mu = 0.09$ a constant, and $\tilde{\eta}$ a parameter accounting for local strain, vorticity, and helicity parameters. In the RNG formulation the parameter $\nu_T = C_\mu k^2/\varepsilon$ is called the eddy viscosity. A further swirl correction reduces the eddy viscosity in areas of high vorticity, allowing the resolution of the unsteady large-scale vortices in regions where these vortices can be resolved by the underlying mesh [45].

The velocity distribution very close to surfaces is modeled by the *law of the wall*. This is realized in such a way that the cell next to the surfaces follows that law [46]. Here, a hybrid wall function $g(y^+)$ is used that smoothly transitions from a turbulent wall function (i.e. a logarithmic profile) at high y^+ values to a viscous wall function (i.e., a linear profile) at low y^+ values:

$$y^+=\frac{y}{\nu}\sqrt{\frac{\tau_w}{\rho}}, \tag{3.8}$$

$$u^+=u\sqrt{\frac{\rho}{\tau_w}}, \tag{3.9}$$

$$u^+=\begin{cases} y^+ & for \quad y^+<5 \\ g\left(y^+\right) & for \quad 5<y^+<35 \\ 1/\kappa\, log\left(y^+\right)+C_1 & for \quad y^+>35 \end{cases} \tag{3.10}$$

where y is the distance to the wall, y^+ the normalized distance to the wall, u^+ the dimensionless velocity, u the velocity parallel to the wall, τ_w the wall shear stress, and κ and C_1 are empirical constants with a value of 0.41 and 5.0 respectively. The wall function is also sensitized to the pressure gradient to account for the effects of an adverse pressure gradient on the near-wall boundary layer profile which is done by an extension of u^+ [47, 48].

3.3.1 The LBM code

In the present work, LBM is utilized in form of the commercial code SIMULIA PowerFLOW™, Release 6-2020-R1. PowerFLOW™ is based on a Cartesian mesh with automatic mesh generation, without restriction on the geometric complexity of the models that can be treated. The PowerFLOW™ software package is subdivided into several modules. There are server as well as client components available. The server components have no graphical user interface (GUI) and are typically executed in the background on a computer cluster. The client components are interactive applications, containing a GUI, and typically run on a user's desktop workstation. Server components include the *Discretizer*, which generates the computational mesh (consisting of so-called *surfels* and *voxels*), the *Decomposer*, with which the computational mesh is distributed across multiple processors for a parallel simulation and the *Simulator*, which runs the simulation and generates the results. Furthermore, for this study following client components are relevant:

- PowerCASE for creating the case setup
- PowerVIZ for visualization and evaluation of simulation results
- PowerACOUSTICS for evaluation of the acoustics (e.g. spectral analyses) and converting PowerFLOW specific file formats into common formats for further processing (e.g. with Matlab™).

A few general remarks concerning mesh generation: The computational mesh is Cartesian; it is constructed from cubic volume elements and is generated automatically. With the help of so-called Variable Resolution (VR) zones, a coarsening/refinement of the computational mesh can be achieved, see Figure 3.4. The resolution of neighboring regions differs by a factor of two in all three dimensions. Thus, in the finest computational domain, the flow quantities are calculated in every time step, in the next coarser one in every second time step, and so on. In addition to the volume elements (*voxels*), the computational mesh also contains surface elements (*surfels*), both of which are created during the discretization of the domain. *Surfels* are created wherever the surface of a body intersects the fluid. For illustration, this is shown in Figure 3.4. It can also be seen in that figure that the lattice of volume elements has a regular cubic structure, whereas the lattice of surface elements is irregular. With this approach, it is possible to create a Cartesian mesh with an arbitrary surface geometry.

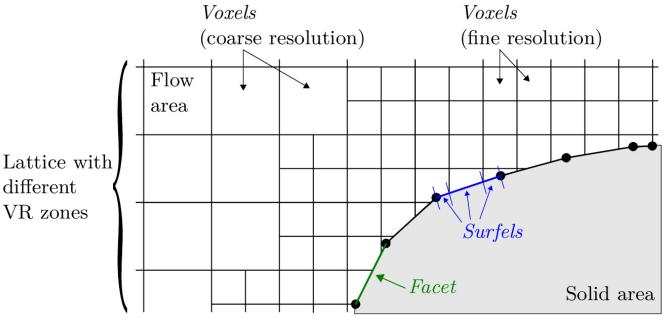

Figure 3.4: Mesh generation in PowerFLOW, adapted from PowerFLOW User guide [38].

3.3.2 Case setup

The LBM simulations are conducted for a DU93W210 airfoil section (slice) of $0.1c_b$ spanwise extension (in z-direction corresponding to a span of L_{LBM} = 30 mm). The global computational domain in the x-/y-plane of the LBM simulation is represented in Figure 3.5 with a tenfold enlarged airfoil for illustration only. The geometry of the numerical setup is normalized with the chord length of the baseline airfoil c_b. Despite the chord length varies when the airfoil is truncated, the physical global size of the numerical setup is kept constant. As indicated in Figure 3.5 the domain extends over $100c_b$ in x- and y-direction. The TE of the airfoil is consistently placed in the center, for all configurations. The boundary conditions on all four boundaries of the simulation domain (North, East, South, and West) are given in terms of the velocity vector $\vec{u}_\infty$ and the static pressure 101,325 Pa. In z-direction the boundary conditions are set to periodic, which means there are no walls, and fluid entering or leaving the domain in z-direction on one side is equivalent to that fluid leaving or entering the opposite side of the domain.

To avoid the reflection, of outgoing sound waves back into the domain, a sponge is implemented in the outer zone of the domain which starts at a radius of $33c_b$, indicated by the gray area in Figure 3.5. Within the sponge zone, additional damping is provided by the exponential increase of the viscosity in the direction of the domain boundaries.

Three scales are useful to be defined:

- The convective time T_c; it describes the time that a fluid particle needs to travel through the domain from west to east; for the given set-up, the convective time is $T_c = 100c_b/u_\infty = 0.5$ s for $u_\infty = 60$ m/s and $T_c = 1$ s for $u_\infty = 30$ m/s.
- The acoustic time T_{ac}, i.e. the time required by an acoustic wave traveling from the airfoil to the outer region of the domain; here $T_{ac} = 50c_b/c_s = 0.04$ s, when taking the speed of sound as $c_s = 340.3$ m/s.

- The through-flow time T_f, which is the time for a fluid particle to pass the airfoil from leading to trailing edge; here: $T_f = c_b/u_\infty = 0.005$ s for $u_\infty = 60$ m/s and $T_f = 0.010$ s for $u_\infty = 30$ m/s.

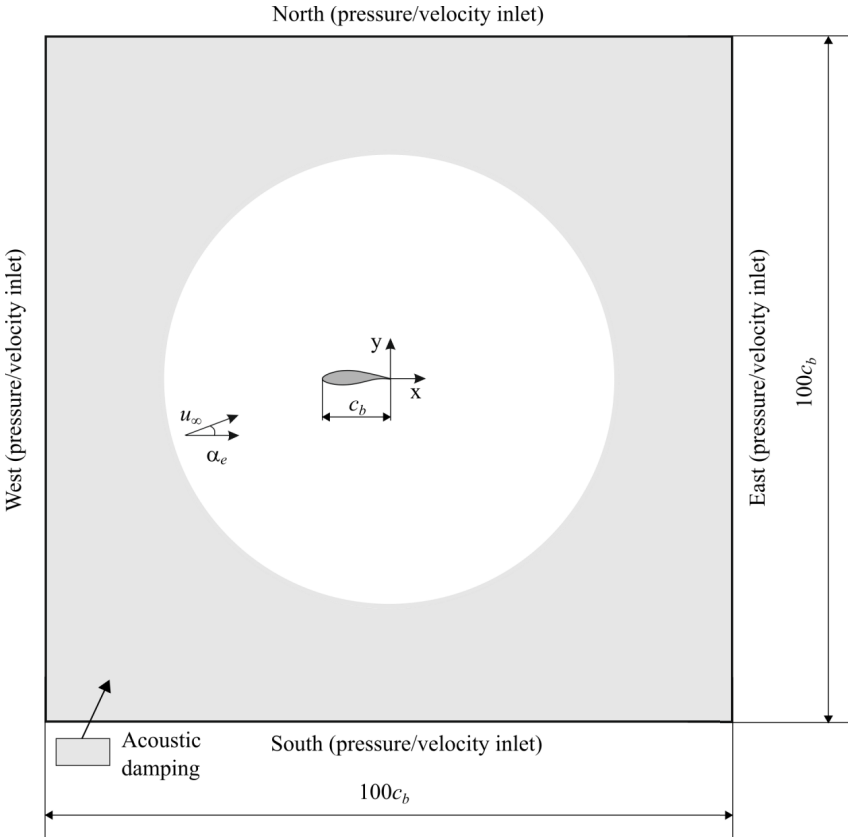

Figure 3.5: Schematic representation of the LBM setup with the tenfold enlarged airfoil.

Since the flow is only affected in the region of the airfoil, and the noise radiation originates from the airfoil, it can be assumed that the flow in the outermost areas of the computational domain is hardly influenced by the airfoil and a fine resolution in these areas would hardly influence the simulation results. Because of the greatest influence on the flow, the finest mesh level is found in the immediate vicinity of the airfoil. Figure 3.6 and Figure 3.7 illustrate how the VR zones are distributed in the vicinity of the airfoil and the domain. Figure 3.6 depicts the first five VR zones close to the airfoil and Figure 3.7 the remaining ones at a greater distance from the airfoil.

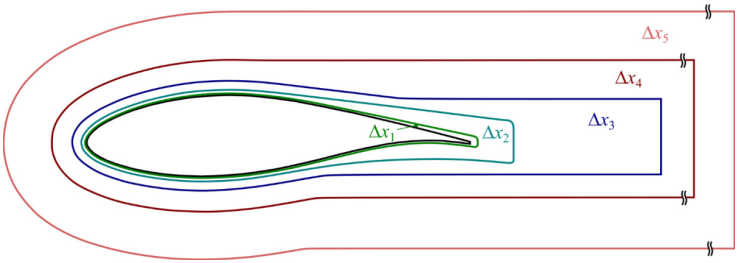

Figure 3.6: To-scale presentation of VR1 to VR5 in the vicinity of the airfoil and its wake indicated by the *voxel* size Δx.

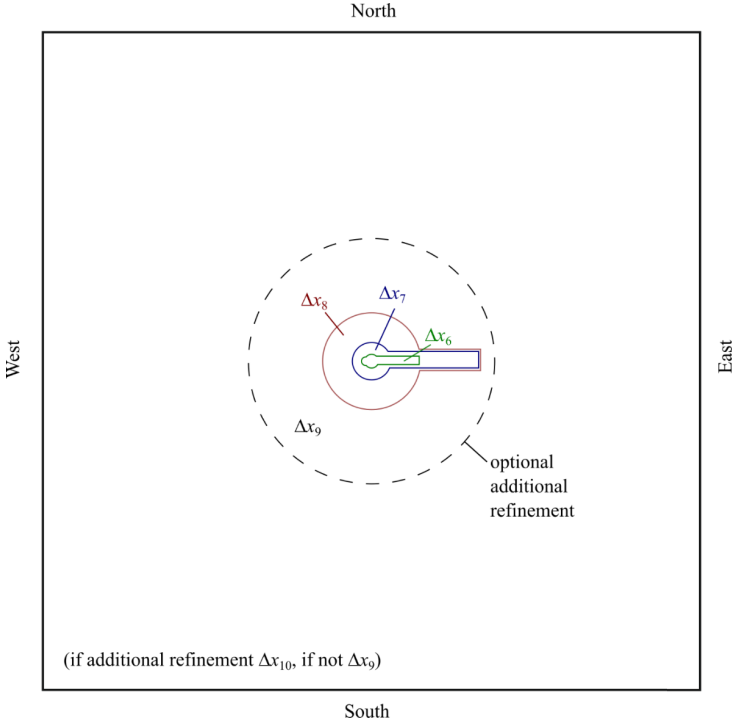

Figure 3.7: To-scale presentation of VR6 to coarsest VR indicated by the *voxel* size Δx.

There are in fact several options for generating the VR zones. This can be done using pre-defined CAD geometries for the corresponding VR zones or using automatically generated VR zones in the form of offsets. As already mentioned the resolution of the flow structures around the airfoil and particularly in the wake is crucial for an accurate solution of the flow field.

For this reason, the VR zone with the finest resolution surrounds the airfoil, and as the distance between the airfoil and its wake increases, the *voxels* in VR zones become coarser. In principle, each VR zone contains at least 20 voxel layers. Two VR zones were specifically designed in CAD for the boundary layer, one containing the finest element size Δx_1, whose distance to the airfoil surface is always larger than the boundary layer displacement thickness, and a second whose distance to the airfoil surface is always larger than the respective boundary layer thickness. Since these sizes increase with increasing proximity to the trailing edge, this was taken into account when creating the VR zones and the distance of the next VR zone also increases with increasing proximity to the trailing edge. This is clearly shown in Figure 3.8 where the true mesh is shown. After the first two VR zones, there are three further zones in which an offset of 20 *voxels* was created and this zone was expanded especially for the wake. The corresponding geometric data are compiled in Table 3.3.

Table 3.3: Geometric details of the different VR zones. Note: The coordinate system referred to is located at the trailing edge position, in the center of the domain.

VR Zone	*Voxel* size	VR zone created by	Extension from TE x-direction	Coordinates of two point box for wake $P_1(x_1\ y_1)$, $P_2(x_2\ y_2)$ $[m]$	Radius of circle $[m]$
VR1	Δx_1	CAD file	$0.02c_b$	-	-
VR2	Δx_2	CAD file	$0.1c_b$	-	-
VR3	Δx_3	offset + box	$0.5c_b$	(-0.125 -0.024) (0.150 0.035)	-
VR4	Δx_4	offset + box	$1.5c_b$	(-0.175 -0.042) (0.450 0.065)	-
VR5	Δx_5	offset + box	$6c_b$	(-0.175 -0.082) (1.200 0.105)	-
VR6	Δx_6	circle + box	$12c_b$	(-0.175 -0.200) (2.400 0.260)	0.35
VR7	Δx_7	circle + box	$24c_b$	(-0.175 -0.400) (4.800 0.460)	0.90
VR8	Δx_8	circle + offset	-	-	2.25
		optional additional VRs by adding circles			
VR9	Δx_9	domain boundaries	-	$(-50c_b\ -50c_b)$ $(50c_b\ 50c_b)$	-

The remaining coarser VR zones from VR6 onwards have been realized with the help of circles whose center lies in the reference coordinate system. For VR6 and VR7, as before, boxes have been created for a finer resolution in the area of the wake. Additional VR zones could be realized by adding more circles between VR8 and the domain boundaries, as indicated in Figure 3.7. The exact *voxel* size Δx_1 to Δx_9 and the mesh structure in this area will be ex-

plained in more detail in section 4.1, where – based on a mesh refinement study – the final mesh is chosen.

Not only the turbulence in the vicinity of the airfoil has to be resolved, furthermore the resolution of the area where the acoustic field data is captured with “microphone probes” is relevant for the direct computation of the acoustics. Sufficient accuracy is obtained when ensuring at least 12 to 16 *voxels* per wavelength [49]. It is essential to note that between the finest *voxel* and the location of the microphone with its *voxel* size, only a stepwise coarsening towards the microphone takes place and the aforementioned requirement is fulfilled.

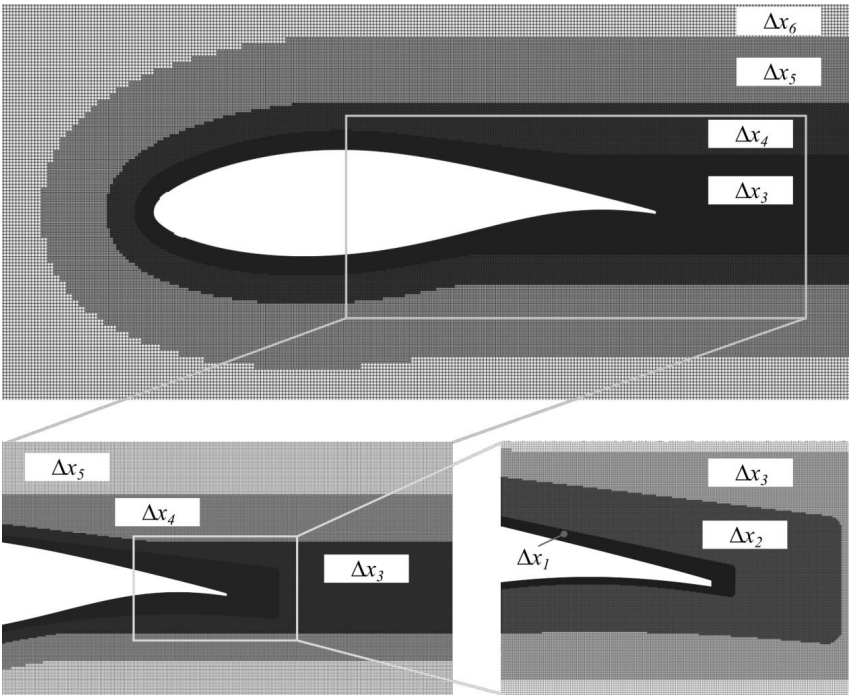

Figure 3.8: Mesh in the vicinity of the airfoil and the airfoil wake and their corresponding *voxel* size Δx.

Figure 3.9 shows the positions of the probes at which the acoustic data are captured in the far field. In total, there are 72 probes arranged in a circle every 5 degrees at a distance of $2.4c_b$ around the trailing edge.

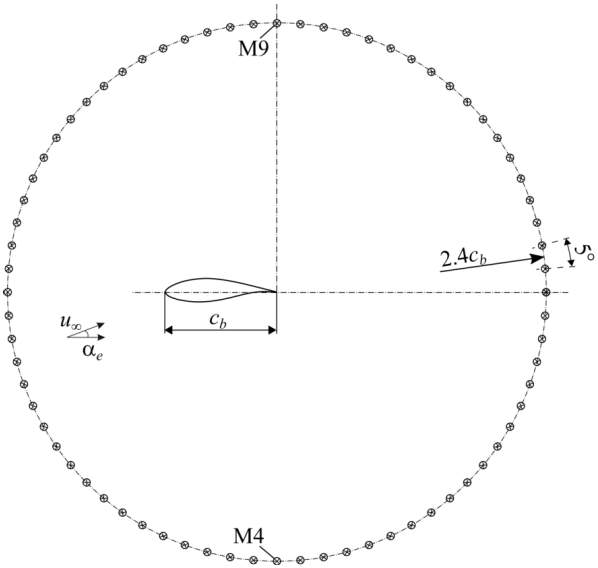

Figure 3.9: Schematic representation of the probes located in the LBM domain for capturing the acoustic far-field data.

3.3.3 Evaluation of acoustic field data

The LBM simulates the unsteady and compressible flow field with low dissipation and dispersion. Assuming the mesh resolution is sufficient, these properties allow the direct extraction of the sound pressure in the domain. This has many advantages. For example, additional models or assumptions are unnecessary when determining the acoustic field. In principle, it is also possible to simulate the surroundings of the test object such as the test rig, as shown by SANJOSÉ ET AL. [50] (which is not done in this thesis).

The numerical setup selected comprises an airfoil section (“slice") of $0.1c_b$ spanwise extension, with periodic boundary conditions in the spanwise direction. However, it is known from OBERAI ET AL. and EWERT ET AL. [51 - 54] that in low-MACH-number flows the turbulent length scale is significantly smaller than the acoustic length scale. Applying periodic boundary conditions for the compressible problems leads to an unphysically correlated acoustic source in the spanwise direction which causes acoustics waves to decay approximately with the inverse of the square root of the radius R ($\sim R^{-1/2}$). Physically, however, the sound pressure decreases approximately with the inverse of the radius R ($\sim R^{-1}$). This would result in an overestimation of the sound pressure level. To avoid this one could consider the full span or use absorbing boundary conditions in spanwise direction. However, this goes along with increased computational cost, and most non-reflecting boundary conditions will not work

properly. Since an integral length scale of the acoustic source in the spanwise direction is small compared to the acoustic wavelength for small MACH numbers, the source is compact in the spanwise direction, WAGNER [51]. As a result, an acoustic simulation with a spanwise extension and periodic boundary conditions is equivalent to a 2D acoustic simulation with a spanwise averaged acoustic source [51]. This can be compensated with the help of a correction to the noise spectra from direct probes in the domain. OBERAI ET AL. and EWERT ET AL. [51 - 54] derived a three-dimensional, frequency-dependent correction for low MACH number flows, which can be rewritten in a dB form as:

$$L_{Spp,3D} = L_{Spp,2D} + 10\log\left(\frac{fL_{LBM}^2}{c_0 R}\right)\text{dB}. \tag{3.11}$$

$L_{Spp,2D}$ is the quantity obtained by the direct probe in the domain, f the frequency, L_{LBM} the simulated spanwise extension, c_0 the speed of sound, and R the observer distance. This correction has been applied to the tracked signals from the probes in the domain for direct noise computation.

In parallel to the direct noise calculation, a hybrid approach is adopted for the computation of the acoustics. This approach is the FFOWCS WILLIAMS and HAWKINGS (FW-H) acoustic analogy [55]. The employed FW-H analogy is based on a forward-time solution [56] of FARASSAT'S formulation 1A [57]. This solution from FARASSAT and SUCCI was extended by BRÈS ET AL. [58] to a convective wave equation. By means of GREEN's function, an integral solution can be generated for the far field, allowing one to employ the analogy for different observer positions. Time-dependent surface pressure fluctuations, sampled at the finest voxels on the airfoil surface, are fed into the acoustic analogy. The formulation is used in this work only for the evaluation of the far-field noise. Note that the analogy only considers sources on the blade surface CURLE [59], other noise sources such as the turbulent wake of the airfoil are not considered. A FW-H far-field analysis code is provided by PowerACOUSTICS.

3.4 Experimental setup and measurement techniques

The experimental investigations carried out in the aeroacoustic wind tunnel of the University Siegen, include the measurement of

- the steady-state pressure distribution along the airfoil pressure and suction side,
- unsteady-state surface (wall) pressure in the vicinity of the trailing edge,
- the turbulent flow field quantities in the wake of the airfoil by hot-wire anemometry, and
- the acoustic far-field.

The measurement setup, measurement technology, and instrumentation of the airfoil are explained in the following sections.

3.4.1 Aeroacoustic wind tunnel

Figure 3.10 depicts the open-jet closed circuit aeroacoustic wind tunnel. The test section has a length of 2.24 m, the nozzle exit area is 0.8 m x 0.8 m. The contraction ratio of the upstream rectangular nozzle, i.e. the ratio of the cross-sectional area at the nozzle in- to outlet, is 6.89. The flow upstream of the nozzle is rectified by a honeycomb and turbulence is reduced by screens in the settling chamber. These design features enable a typical turbulent intensity of less than $TI = 0.5$ % at a maximum flow velocity of 70 m/s in the test section. The collector can be shifted to the side such that it completely captures strongly deflected flow as in the case of airfoil testing. The heat generated is removed by a radiator downstream of the fan.

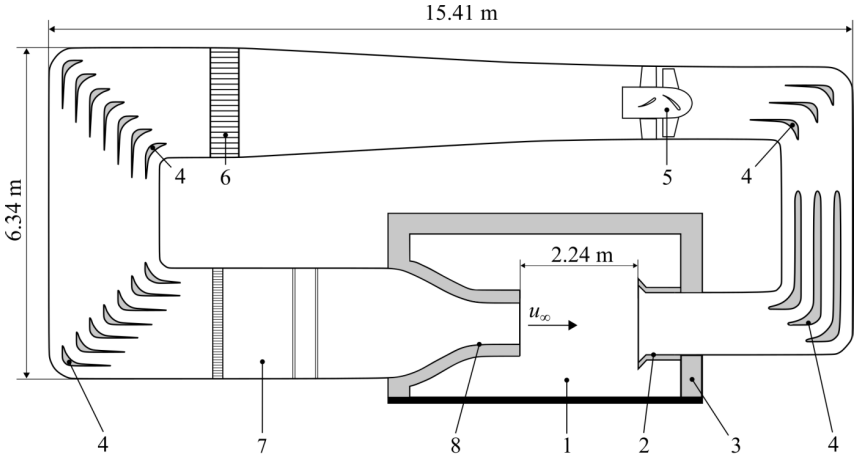

Figure 3.10: Sketch of the aeroacoustic wind tunnel of the UNIVERSITY OF SIEGEN (side view): 1: semi-anechoic chamber/test section, 2: collector, 3: anechoic lining, 4: sound absorbing guide vanes, 5: axial fan, 6: heat exchanger, 7: settling chamber, 8: nozzle.

The test section is located in a large semi-anechoic chamber with sound-absorbing lining. This enables acoustic measurements at free-field conditions according to ISO 3745 [60] for frequencies $f > 100$ Hz. The dimensions of the anechoic chamber surrounding the free jet are 5.2 m x 6.1 m x 3.0 m.

The nozzle exit flow velocity is determined by the differential pressure method. For this purpose, the pressure difference between the settling chamber and the plenum or anechoic chamber is measured. The static pressure in the settling chamber is measured downstream of the last turbulence screen via a ring line. In the anechoic chamber, the static pressure, which in this case is equivalent to atmospheric pressure, is captured via a pressure transducer above the nozzle. It considers losses between the settling chamber and the nozzle outlet as well as boundary layer thickness by corrections.

A series of 12 microphones (1/2", type 4190 from BRÜEL & KJÆR™) is arranged in a circle at a distance of 1 m (corresponding to $3.3c_b$) around the trailing edge at various angles. Microphones M4 and M9 are always perpendicular to the trailing edge. Figure 3.11 illustrates the configuration of the microphones during the measurements. Note that the microphone position changes with the angle of attack to the airfoil. All microphones are located outside of the jet and are additionally equipped with a windscreen. According to the manufacturer, the microphones enable the recording of sound signals from 6.3 Hz to 20 kHz at a dynamic range of 14.6 - 146 dB. All microphones are calibrated prior to a measurement with a BRÜEL & KJÆR™ calibrator type 4231.

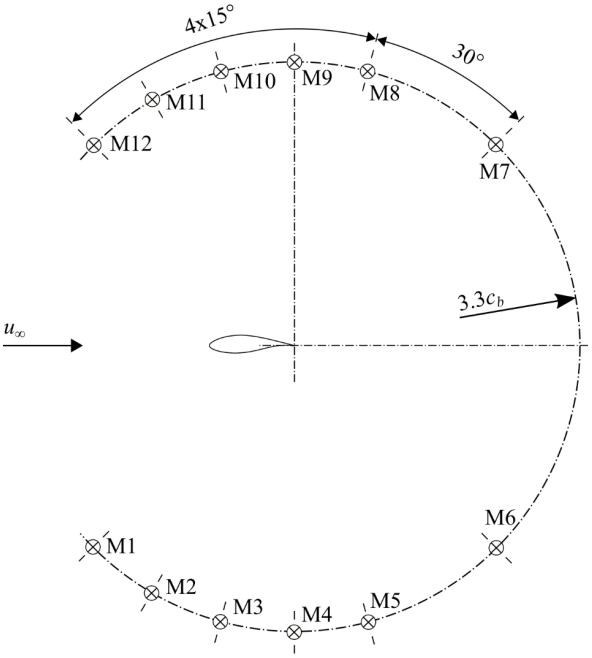

Figure 3.11: Schematic representation of the microphone setup.

The illustration Figure 3.12 shows the installed airfoil in the test section of the wind tunnel. The airfoil is clamped vertically between side plates. These side plates are covered with acoustic foam. To adjust the angle of attack, the airfoil can be rotated vertically.

The background noise (BGN) of the wind tunnel with and without side plates (SP) is depicted in Figure 3.13 for the two selected flow velocities u_∞ = 30 m/s and 60 m/s.

Figure 3.12: Setup at the aeroacoustic wind tunnel of University Siegen: 1: nozzle, 2: anechoic lining, 3: side plate, 4: SS of the airfoil, 5: exchangeable TE section, 6: collector, 7: microphone and 8: PS of the airfoil.

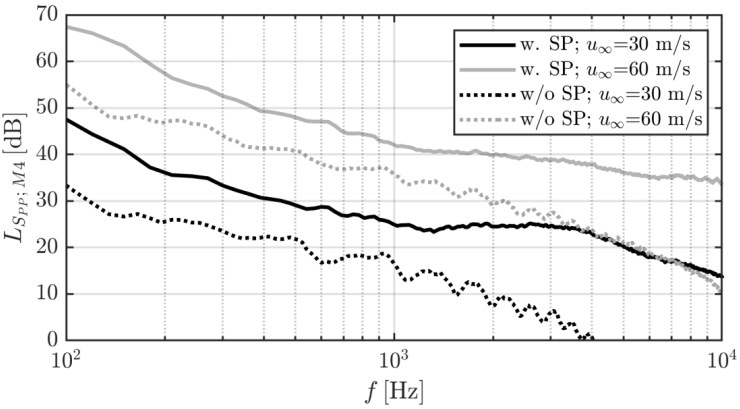

Figure 3.13: Background noise of empty wind tunnel with and without side plates (SP) at u_∞ = 30 m/s and 60 m/s; power spectral density of the signal from microphone M4.

3.4.2 Airfoil section and instrumentation

The airfoil section for the wind tunnel tests, Figure 3.14, consists mainly of a main front body, accurately milled from aluminum and a set of trailing edge sections. The trailing edge sections were printed via stereolithography with a DuraForm polyamide. They can be attached to the main body. Because of tolerances, at the transition from the main front body to the trailing edge sections, occasionally a very small step on the suction side of about 0.1 mm was observed. The span of the airfoil section investigated experimentally is L_{EXP} = 800 mm. It corresponds to the side length of the wind tunnel nozzle exit.

The airfoil section is instrumented for measuring the static pressure distribution along the pressure and suction side, the unsteady wall pressure in the vicinity of the TE, and the unsteady flow velocity in the turbulent wake.

Static pressure distribution. At midspan, 39 small holes on the suction side and 15 on the pressure side along the chord serve as static pressure taps. Naturally, close to the trailing edge pressure taps were not feasible. Each of these holes is connected via a tube to a multi-channel pressure scanner from PRESSURE SYSTEMS INC. (type: NETSCANNER, model: PSI 9116).

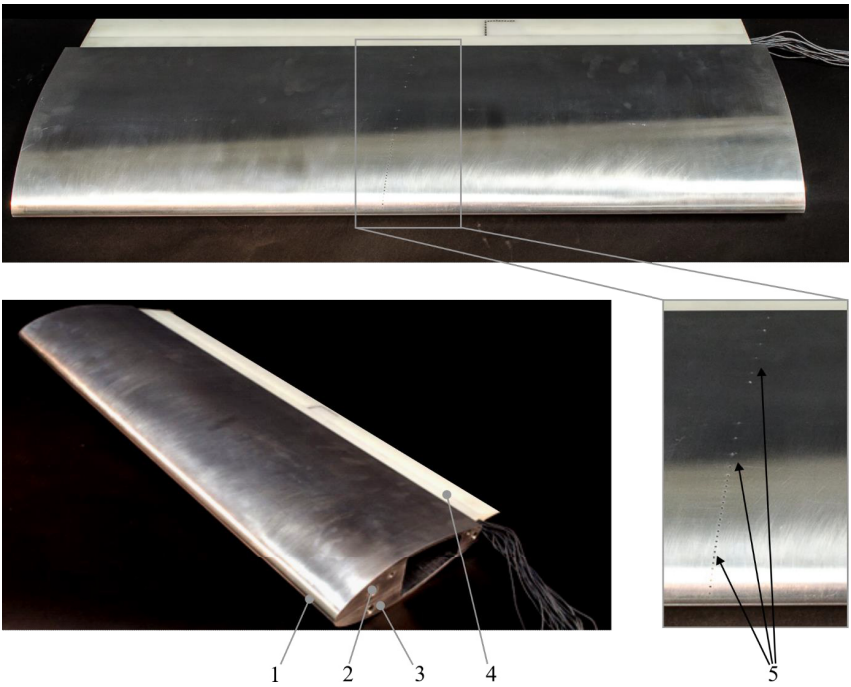

Figure 3.14: Airfoil assembly for experimental tests in the aeroacoustic wind tunnel: 1: leading edge, 2 and 3: main front body, 4: exchangeable trailing edge section, 4: exchangeable trailing edge section and 5: static pressure taps along the chord.

Unsteady wall pressure. The unsteady wall pressure at point-like locations in the vicinity of the TE is recorded with a special probe microphone (BRÜEL & KJÆR™, type 4182), Figure 3.15. The probe is placed at $x/c = 0.93$ on both, the suction and pressure side. The probe microphone readings are corrected for non-flat frequency response in the 20 Hz to 10 kHz range using the frequency response curve provided by the manufacturer. A schematic drawing and a typical frequency response of the probe microphone used can be found in Appendix C.

Unsteady flow velocity. The unsteady flow velocity in the turbulent wake is obtained by hot-wire anemometry. The 1-wire probe is a TSI type 1210-T1.5 probe. Its tungsten wire is 1.25 mm long and has a diameter of 5 µm. The positioning of the probe relative to the airfoil is performed by a three-axis traverse from ISEL™, consisting of three linear units with spindle drive (ball screws, type: LES 4 or LES 6). The positioning accuracy is 0.02 mm.

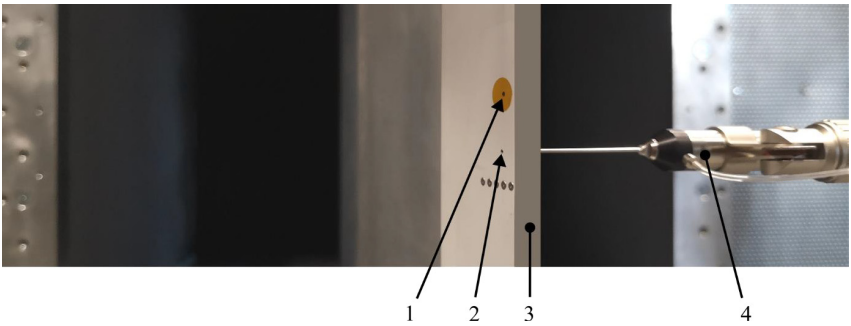

Figure 3.15: Installation of the probe microphone for the acquisition of surface pressure fluctuations: 1: Access for measurement on pressure side, 2: Measurement on suction side, 3: Trailing edge, 4: Probe microphone; the five surface mounted miniature microphones at the trailing at are not used within this study.

The probe is traversed along 13 lines, each extending over 200 mm, which are located in the center of the span and perpendicular to the mean flow u_∞, Figure 3.16. The increment of the measuring points is varied depending on the distance to the wake, in the outer region $\Delta\psi = 2$ mm, in the inner 0.5 mm. Moreover, the inner, finer-resolution part, is shifted to account for the anticipated direction of the wake. In order not to damage the hot-wire the minimum distance to the center of the TE was $\Delta x = 7.5$ mm.

The density of the air ρ is determined via the measured barometric pressure and temperature in the test section. Reference velocity u_∞ and pressure p_∞ are determined according to the standard DIN EN 12599:2010 [61].

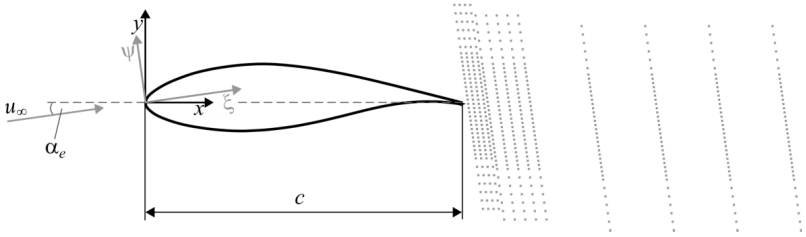

Figure 3.16: Traverses of the hot wire probe for capturing the flow velocity in the wake.

3.5 Data acquisition and evaluation

3.5.1 Data acquisition

The multi-channel data acquisition system National Instruments™, type: NI PXI-4472, has a resolution of 24 bits. Sampling frequencies and acquisition times are compiled in Table 3.4.

This table also lists the corresponding values for the evaluation of the data from the Lattice-BOLTZMANN simulations.

Table 3.4: Sampling frequencies and time for capturing different types of data from experiment and simulation.

Type of data acquisition	Sampling frequency $f_{s,LBM}$ [kHz]	Acquisition time $t_{s,LBM}$ [s]	Sampling frequency $f_{s,EXP}$ [kHz]	Acquisition time $t_{s,EXP}$ [s]
Far-Field acoustics	157.2	0.2	51.2	30
Pressure distribution	245.4	0.1	0.2	30
Surface pressure fluctuations	10,059	0.2	51.2	30
Unsteady/steady flow measurements	39.3	0.1	51.2	1

For the numerically acquired data, it is particularly important to determine the time at which a (quasi-) steady-state solution is reached. For this, a simulation with a physical runtime of 1 s for the case with $t^* = 0.005$, $\alpha_e = 0°$ and $u_\infty = 60$ m/s was carried out. The time trace of the velocity u and the effective angle of attack α_e are depicted in Figure 3.17. As a conclusion, only data starting 0.05 s from initiation (i.e. $t = 0$ s) are used for data evaluation.

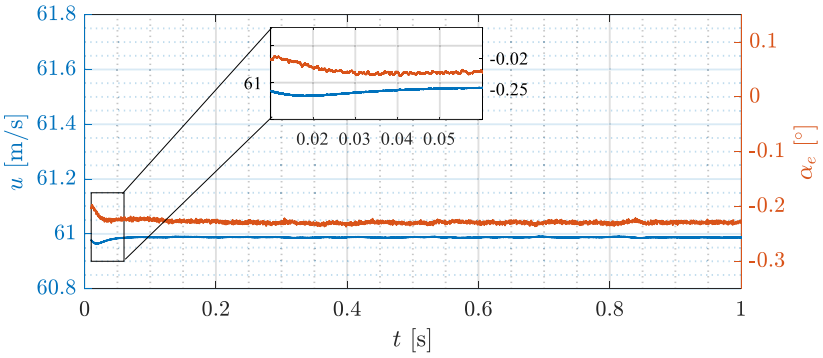

Figure 3.17: Lattice-BOLTZMANN simulation: Steady-state solution after 0.05 s upon initiation of simulation.

3.5.2 Data evaluation

If not otherwise stated the evaluation is identical for both, experimental and numerical LBM-data.

3.5.2.1 Time-averaged quantities

The pressure coefficient is defined as:

$$C_p \equiv \frac{p - p_\infty}{0.5\rho u_\infty^2} \tag{3.1}$$

where p is the static pressure at the point at which pressure coefficient is being evaluated, p_∞ and u_∞ are the static pressure and velocity in the free-stream and ρ the density of the fluid. The pressure coefficient is used to represent the distribution of the time-averaged static pressure on the airfoil pressure and suction sides.

The boundary layer (BL) integral quantities such as BL thickness δ and displacement thickness δ^* are calculated in the usual way. δ_{99} is defined as the point y_{tan} away from the wall, where the wall-parallel velocity is 0.99 of the edge velocity U_e and the integral of the wall-normal vorticity component stabilizes and becomes zero:

$$\delta_{99} = y_{\tan}\left(u = 0.99U_e\right). \tag{3.2}$$

The BL displacement thickness δ^* is the distance a streamline just outside the BL is displaced away from the wall:

$$\delta^* = \int_{y=0}^{y(u=0.99U_e)} \left(1 - \frac{u}{U_e}\right) dy. \tag{3.3}$$

The surface points, at which the steady and later the unsteady pressure distribution as well as the BL parameters are extracted from the LBM database, are shown in Figure 3.18. Lines normal to the airfoil surface were created along the chord to determine the suction and pressure side BL parameters. In the wind tunnel experiments, the boundary layer data were not collected. The pressure distribution determined in the experiment was based on fewer measuring points, whose distribution was more concentrated at the LE of the airfoil and coarser toward the TE.

3.5.2.2 Unsteady quantities

The standard spectral representation of any unsteady quantity x' (in this thesis the acoustic pressure, wall pressure, and flow velocity) is the power spectral density. The power spectral density is the averaged power of a given signal at each frequency in an infinitesimally small frequency band:

$$S_{xx}(f) = \lim_{\Delta f \to 0} \frac{x'^{\,2}_{rms}(f)}{\Delta f}. \tag{3.4}$$

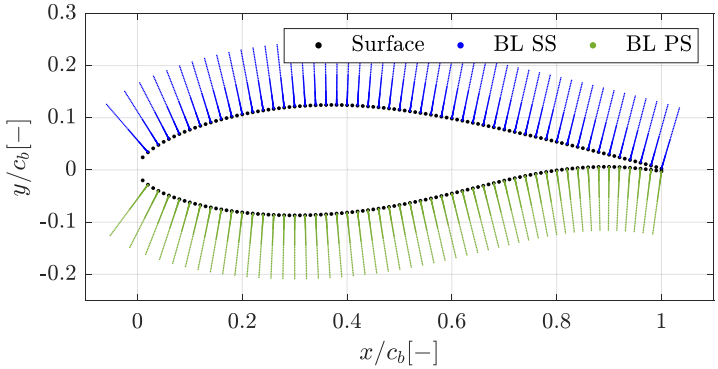

Figure 3.18: Points on the airfoil surface taken for LBM evaluation of the static pressure distribution, wall pressure fluctuations, and BL characteristics.

To obtain levels in dB a reference bandwidth Δf_{ref} = 1 Hz and a reference value x_{ref} are chosen. For any fluctuating pressure (wall or acoustic pressure), $x_{ref} = p_0 = 2 \cdot 10^{-5}$ Pa:

$$L_{S_{xx}}(f) = 10 \log_{10}\left(\frac{S_{xx}\Delta f_{ref}}{x_{ref}^2}\right) \text{dB}. \tag{3.5}$$

In practice, the power spectral density of the recorded time signals, whether from simulation or experiment, is transformed into the frequency domain by a fast-Fourier-transformation (FFT). For this purpose, the function *pwelch* in Matlab™ R2022a is utilized. The parameters chosen in *pwelch* are `window` = hanning, `noverlap` = 0.5, `nfft` = $f_s/\Delta f$ with the final frequency resolution of Δf = 30 Hz if not stated differently.

The spanwise coherence of wall pressure fluctuations, which is known to play a relevant role for TEN in the scattering process, ROGER ET AL. [30], is considered as well. To examine the relation between two signals x and y the Matlab™ coherence function *mscohere* is used. It is defined as the squared magnitude of the cross-spectrum of two signals sampled at two spanwise positions spaced x and y, divided by the power spectrum of both signals at each frequency:

$$\gamma_{xy}^2(f) = \frac{\left|S_{xy}(f)\right|^2}{S_{xx}(f) \cdot S_{yy}(f)}. \tag{3.6}$$

A further important parameter is the spanwise coherence length l_z. It can be seen as the length of a source term scattering at the TE and it is a function of the frequency f:

$$l_z = \int_0^\infty \sqrt{\gamma^2(f,\eta)}\, d\eta, \tag{3.7}$$

where $\gamma^2(f, \eta)$ is the squared coherence function of the wall pressure between two positions spaced by η along the spanwise coordinate z.

Another quantity used in this work to analyze the signals is the discrete normalized two-point cross-correlation $R_{xy,coeff}$, which is a measure of the similarity between two discrete signals x and y:

$$R_{xy,coeff}(m) = \frac{1}{\sqrt{R_{xx}(0)\,R_{yy}(0)}} R_{xy}(m) \text{ with } R_{xy}(m) = \sum_{n=1}^{N-m-1} x_{n+m} y_n\,, \tag{3.8}$$

where the time lag m is used to apply a relative time shift to the sequences so their similarity can be compared over time. The Matlab™ function *xcorr* is utilized for this.

3.5.2.3 Normalizing acoustic data to reference distance source - observer

Since experimental and numerical results potentially origin from different distances between observer and source R and different spanwise extensions L of the airfoil section, the spectral density level of the acoustic pressure is normalized to a reference distance between observer and source of R_{ref} = 1 m and a reference span of L_{ref} = 1 m. This has been done in many TEN studies. As described in VAN DER VELDEN ET AL. [62], assuming a non-compact sound source, the working formula is

$$L_{S_{PP}} = L_{S_{PP},raw} + 10\log\left[\left(\frac{R}{R_{ref}}\right)^2\left(\frac{L}{L_{ref}}\right)\right]\text{dB}. \tag{3.9}$$

3.5.2.4 Proper orthogonal decomposition (POD) with the direct and snapshot methods

Coherent structures play an essential role in turbulent flows, e.g. in the context of noise generation. The presence of “organized” or coherent structures in sheared flows has interested the aerodynamic community. Several families of modal analysis exist to decompose the coherent structures that govern the behavior of a flow. In this thesis, the proper orthogonal decomposition (POD) and spectral proper orthogonal decomposition (SPOD) are applied to identify the presence of the VS structures associated with the strong unsteadiness in the flow and affecting the acoustics.

The most popular method used in the literature is the POD, whose algorithm has been described in detail by a large number of authors, among others by BERKOOZ ET AL. [63], CHATTERJEE [64], TAIRA ET AL. [65] and WEISS [66]. The challenge is to decompose a vector field of a quantity (here velocity) representing the motion of a turbulent flow via a set of deterministic functions as:

$$u'(\vec{x},t) = \sum_{n=1}^{\infty} a_n(t)\,\Phi_n(\vec{x}), \tag{3.12}$$

where each of them captures a ratio of the kinetic energy of the flow. $u'(\vec{x}, t)$ is the fluctuation of the velocity vector at the measurement point $\vec{x}$ and time t considered.

The fluctuations of the velocity component are decomposed into the sum of the product of the deterministic function $\Phi_n(\vec{x})$ multiplied by the time coefficient $a_n(t)$, in theory over an infinite number of modes. In practice, this decomposition is performed for a finite number of modes, implying as many representations of "coherent structures", whereby most of the flow energy is encapsulated in only a few dominant contributions CHEN ET AL. [67]. These functions $\Phi_n(\vec{x})$ are furthermore eigenfunctions whose corresponding eigenvalues come from the covariance matrix, denoted C, defined in:

$$C\Phi_n = \lambda_n \Phi_n \text{ with } \Phi_n \in \mathbb{R}^M \text{ and } \lambda_1 > \lambda_2 > ... > \lambda_M, \tag{3.13}$$

with

$$C = \frac{1}{N-1}\sum_{i=1}^{N} x(t_i)x(t_i)^T = XX^T \in \mathbb{R}^{M\times M}, \tag{3.14}$$

where the matrix X represents the N *snapshots* of the recorded velocity fluctuation field data that have been grouped into columns of length M as:

$$X = \left[x(t_1)x(t_2)...x(t_N)\right] \in \mathbb{R}^{M\times N}. \tag{3.15}$$

The column vectors $x(t_i)$ have in this case the size of the selected mesh taken for capturing the quantities during the simulation, i.e. $M = N_{dim} \times N_x \times N_y$ with $N_{dim} = 2$ for the u and v components and $N_{dim} = 1$ for the pressure. Furthermore, N_x and N_y are the number of points defined in the measurement window of the simulation along the x and y axes respectively. This resolution of the eigenvalue problem is called the direct POD method.

Since the matrix C is real and symmetric by construction, the eigenmodes $\Phi_n(\vec{x})$ form an orthonormal basis in which the covariance matrix of the direct method is diagonalizable. The modes obtained are then orthogonal two by two, and verify in addition the following scalar product relation:

$$<\Phi_j, \Phi_k> = \int_V \Phi_j \cdot \Phi_k dV = \delta_{jk}, \text{ with } j,k = 1,...,N. \tag{3.16}$$

Then the temporal coefficients are obtained with the relation:

$$a_k(t) = < X(t), \Phi_k > \tag{3.17}$$

and finally, the reconstruction of the velocity components is obtained for a number N of modes considered:

$$\tilde{u}(\bar{x},t) = \begin{bmatrix} \bar{U} \\ \bar{V} \end{bmatrix} + \sum_{k=1}^{N} a^k(t)\Phi_k(\bar{x}). \tag{3.18}$$

The relation obtained in equation (3.17) represents the reconstruction of the motion of a turbulent flow based on a chosen number of deterministic modes that optimally capture the associated turbulent kinetic energy. The original POD method thus allows to create a reduced model by considering a minimal dimension from the eigenvectors of the obtained basis. When the mesh size of the $M = N_{dim} \times N_x \times N_y$ points in the selected mesh of view increases, the corresponding increase in the size of the covariance matrix $C \in \mathbb{R}\, M \times M$ makes the eigenvalue problem practically impossible to solve. SIROVICH [68], however, showed that an alternative called the method of *snapshots*, simplifies this problem when the number of recorded data images is small compared to the number of measurement points considered. One then can study the matrix $C_S = X^T X$ instead of $C = XX^T$ defined in Equation (3.14). This results in a matrix problem of size $N \times N$ instead of $M \times M$ whose non-zero eigenvalues are then the same as for the direct method. Instead of considering a decomposition involving deterministic spatial modes and random coefficients, one can consider a decomposition in deterministic temporal modes with spatial coefficients with random spatial coefficients, which - in other words - amounts to exchanging x and t in the POD algorithm, WEISS [66]. The relative ease of implementation of POD (on 2D data at least) as well as the robustness to noise in the data make it a popular tool, TAIRA ET AL. [65]. On the other hand, an important limitation in the study of turbulent flows and the instationarities involved remains: Each POD time coefficient contains a multitude of frequencies. Hence, it is not possible to relate a POD mode to a single frequency. This point is addressed in the next section which presents the modal analysis methods in the frequency domain (Spectral proper orthogonal decomposition, SPOD). Although the POD analysis provides one mode for each snapshot and ranks them according to their energy contribution to the total turbulent kinetic energy it is unnecessary to interpret them all. One can focus on only a few of the low-order modes, the main contributors that govern the behavior of a flow.

3.5.2.5 Spectral proper orthogonal decomposition (SPOD)

The spectral proper orthogonal decomposition method in the frequency space, known as SPOD, has recently been formulated by TOWNE, SCHMIDT, and COLONIUS [69]. This form of POD ties back to the original work as formulated by LUMLEY, but has not had the same success in the literature to date as POD in the classical sense. To justify their approach, TOWNE ET AL. [69] argue that a key point of comparison between SPOD and POD is that, while the former guarantees modes that are consistent in time and space, the latter only provides access to spatially consistent modes. In this way, they address the disagreement over the very definition of coherent structures (cf. GEORGE [70]).

Recently, SCHMIDT and COLONIUS [71] continued their explanation in a user guide of the algorithm and made the observation that for the classical POD, the covariance matrix is com-

puted for a zero delay. Therefore, any notion of temporal correlation in the resulting structures would be lost.

Previously, the covariance matrix C used for the POD was defined by:

$$C = \frac{1}{N-1}\sum_{i=1}^{N} x(t_i)x(t_i)^T = XX^T \in \mathbb{R}^{M\times M} . \tag{3.19}$$

Equation (3.19) is evaluated at zero delay, i.e. $C = (x, x', 0)$. The idea of SPOD is to realize that a statistically stationary flow contains both dimensions, spatial and temporal, in the calculation of the covariance:

$$C(x, x', t, t') \rightarrow C(x, x', \tau), \text{ with } \tau = t - t' . \tag{3.20}$$

From equation (3.20) one can then solve a series of problems with POD eigenvalues, in Fourier space, namely one frequency at a time. The transition to frequency is written in an integral way:

$$S(x, x', f) = \int_{-\infty}^{\infty} C(x, x', \tau) e^{-2i\pi f\tau} d\tau . \tag{3.21}$$

Equation (3.21) is the Fourier transform of the covariance and becomes the cross-spectral density tensor. The latter becomes the centerpiece on which the eigenvalue problem is repeated: One then finds a basis of eigenmodes defined at each frequency $\phi_f(x)$, which when going back to the time domain, are mutually orthogonal. This process is summarized in Figure 3.19. The computation is performed as follows: Again the velocity data are concatenated into column matrices of length M, considering N snapshots:

$$X \equiv Q = [q_1, q_2, ..., q_N] \in \mathbb{R}^{M\times N} . \tag{3.22}$$

Then we group the data into a number n of blocks as described in the first step in Figure 3.19:

$$Q^{(n)} = \left[q_1^{(n)}, q_2^{(n)}, ..., q_{N_f}^{(n)} \right] \in \mathbb{R}^{M\times N_f} . \tag{3.23}$$

Equation (3.23) shows the number N_f contained in the block (n). Then for each block, the cross-spectral density tensor is obtained by performing a discrete Fourier transform (DFT) as seen in the second step in Figure 3.19:

$$\hat{Q}^{(n)} = \left[\hat{q}_1^{(n)}, \hat{q}_2^{(n)}, ..., \hat{q}_{N_f}^{(n)} \right], \text{ with} \tag{3.24}$$

$$\hat{q}_k^{(n)} = \frac{1}{\sqrt{N_f}} \sum_{n=1}^{N_b} \hat{q}_j^{(n)} e^{-2i\pi(k-1)(j-1)/N_f} . \tag{3.25}$$

Then we can obtain the tensor $S(x, x', f)$ at frequency $f = f_k$ by writing

$$S_{f_k} = \frac{\Delta t}{N_b} \sum_{n=1}^{N_b} \hat{q}_k^{(n)} \left[\hat{q}_k^{(n)} \right]^*, \tag{3.26}$$

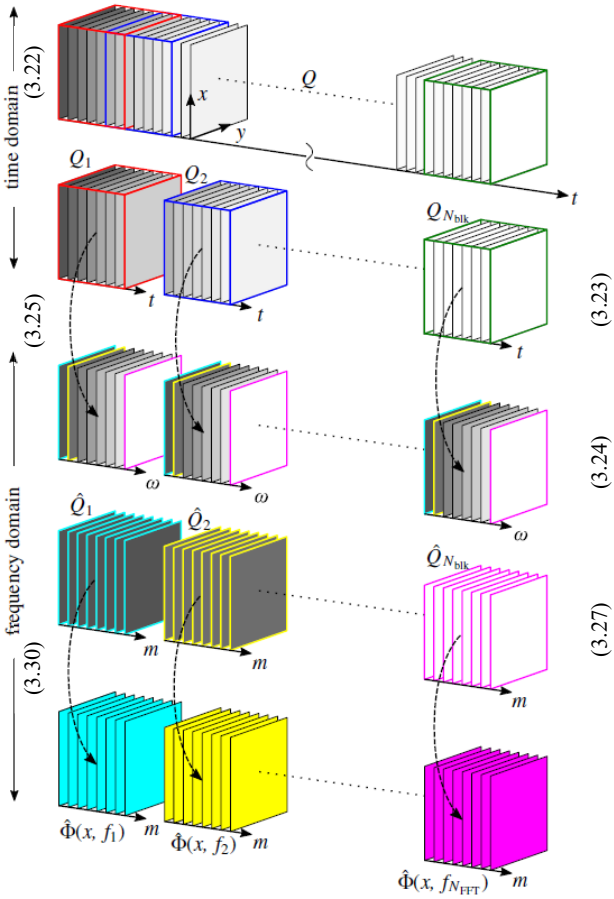

Figure 3.19: Schematic of the SPOD algorithm. Each rectangular slice represents a snapshot, and the numbers in the parentheses denote the equation in the text. The data is first segmented into blocks, then Fourier transformed, then reordered by frequency, and finally diagonalized into SPOD modes (taken from SCHMIDT and COLONIUS [71]).

where the * denotes the conjugate matrix. Then, as seen in the third step in Figure 3.19, the Fourier coefficients are reordered into new blocks, but this time with the same frequency value Fourier coefficients into new blocks associated with the k^{th} index in the frequency vector:

$$\hat{Q}_{f_k} = \sqrt{\kappa}\left[\hat{q}_k^{(1)}, \hat{q}_k^{(2)}, ..., \hat{q}_k^{(N_b)}\right] \in \mathbb{R}^{N \times N_b} \text{ with } \kappa = \frac{\Delta t}{N_b}. \tag{3.27}$$

This allows writing the formula for the cross-spectral density tensor as:

$$S_{f_k} = \hat{Q}_{f_k} \hat{Q}_{f_k}^{*}. \tag{3.28}$$

The SPOD eigenvalue problem is then written as:

$$S_{f_k} \Psi_{f_k} = \Psi_{f_k} \Lambda_{f_k}, \tag{3.29}$$

which, it should be noted, must be solved for each frequency f_k. We find in Equations (3.28) and (3.29) an analogous problem to the spatial POD that defined the covariance matrix: $XX^T \cdot \Psi = \Psi\Lambda$. Now the problem is the size of the matrix $\hat{Q}_{f_k}$ which is: [LBM mesh size × N_b], where LBM mesh size = $N_{dim} \times N_x \times N_y$, here the dimension to consider is $N_{dim} = 2$ for the velocity field ($N_{dim} = 1$ for the pressure field), and the number of blocks formed N_b. Similar to the POD problem reformulated by SIROVICH [68], where X^TX is treated preferentially rather than XX^T, TOWNE ET AL. [69] treat the problem $\hat{Q}_{f_k}^{*} \hat{Q}_{f_k}$ rather than $\hat{Q}_{f_k} \hat{Q}_{f_k}^{*}$ to handle a smaller eigenvalue problem as [LBM mesh size] >> N_b. The new SPOD problem is then rewritten as

$$M_{f_k} \cdot \Theta_{f_k} = \left(\hat{Q}_{f_k}^{*} \hat{Q}_{f_k}\right) \cdot \Theta_{f_k} = \Theta_{f_k} \Lambda_{f_k}, \tag{3.30}$$

and the new eigenvalue problem is solved for:

$$\left[\Theta_{f_k}, \Lambda_{f_k}\right] = eig\left(M_{f_k}\right), \text{ with } M_{f_k} = \hat{Q}_{f_k}^{*} \hat{Q}_{f_k} / N_b. \tag{3.31}$$

An important element is then the reconstruction of the velocity or rather pressure fields using a reduced model, similar to what is done for the POD snapshot method. For the reconstruction from the SPOD decomposition, the inverse Fourier transform is performed on $\hat{Q}_{f_k}$ to return to the reconstructed flow, as done by LE FLOC'H [72]:

$$\Psi_{f_k} = \left(\hat{Q}_{f_k} \Theta_{f_k}\right) \Lambda_{f_k}^{-1/2} N_{f_k}^{-1/2} \Rightarrow \hat{Q}_{f_k} = \sqrt{N_b \Lambda_{f_k}}\, conj\left(\Theta_{f_k}\right). \tag{3.32}$$

Following Equation (3.32) one then recovers the FFT term by extracting the eigenvalues Θ_{f_k} from the code of TOWNE ET AL. [69], which allows, after performing the inverse Fourier transform, to reconstruct the fluctuations of the velocity/pressure field. A comparative overview of the POD and SPOD analysis is given in Table 3.5. It also provides information about the pos-

sibility to finally reconstruct the components of the fluctuating field (pressure/velocity) by choosing the number of modes desired and/or the range of frequencies of interest.

Table 3.5: Comparative overview of the POD (spatial) and SPOD (spatio-temporal) algorithms and field reconstruction for the example of the velocity field.

	POD	**SPOD**
Domain	Time t	Frequency f_k
Name of the data	$X \in \mathbb{R}^{(2N_xN_y)\times(N_t)}$	$\hat{Q}_{f_k} \in \mathbb{C}^{(2N_xN_y)\times(N_b)}$
Name of the eigenvector	Spatial mode $\Phi_k \left(k=1,...,N_t\right)$	Spatial and temporal mode: $\Psi_{f_k} \left(k=1,...,N_f\right)$
Covariance vector	$C = XX^T \in \mathbb{R}^{(2N_xN_y)\times(2N_xN_y)}$	$S_{f_k} = \hat{Q}\hat{Q}^* \in \mathbb{C}^{(2N_xN_y)\times(2N_xN_y)}$
Direct problem	$C\Phi_k = \Phi_k\Lambda_k$ → Voluminous	$S_{f_k}\Psi_{f_k} = \Psi_{f_k}\Lambda_{f_k}$ → Voluminous
"Snapshot" method	$C_S = X^T X \in \mathbb{R}^{N_t\times N_t}$ → $C_S\Psi_k = \Psi_k\Lambda_k$	$M_{f_k} = \hat{Q}^*_{f_k}\hat{Q}_{f_k} \in \mathbb{C}^{N_b\times N_b}$ → $M_{f_k}\Theta_{f_k} = \Theta_{f_k}\Lambda_{f_k}$
(Eigen-) Mode	$\Phi_k = X\Psi_k\Lambda_k^{-1/2}$	$\Psi_{f_k} = \hat{Q}_{f_k}\Theta_{f_k}\Lambda_{f_k}^{-1/2}N_b^{-1/2}$
Coefficient reconstruction	in time: $a^k(t) = \langle X(t), \Phi_k \rangle$	in frequency: $\hat{Q}_{f_k} = \sqrt{N_b\Lambda_{f_k}}\Psi_{f_k} conj\left(\Theta_{f_k}\right)$
Reconstruction the field of fluctuation	$\begin{bmatrix} u' \\ v' \end{bmatrix} = \sum_{k=1}^{N_t} a^k(t)\Phi_k\left(\bar{X}\right)$	$\begin{bmatrix} u' \\ v' \end{bmatrix} = \sum_{k=1}^{N_f} \mathrm{Re}\left(\hat{Q}_{f_k}\right)\times\cos\left[2\pi(k-1)t\right]...$ $-\sum_{k=1}^{N_f} \mathrm{Im}\left(\hat{Q}_{f_k}\right)\times\sin\left[2\pi(k-1)t\right]$

4. Verification and validation of the LBM results

The objective of this chapter is to verify and validate the numerical LBM results. The case considered is the

- baseline airfoil section with its TE thickness-to-chord ratio $t^* = 0.005$, operated at standard conditions,
- effective angle of attack $\alpha_e = 0°$,
- free-stream velocity of $u_\infty = 60$ m/s, corresponding to $Re_c = 1.2 \cdot 10^6$,
- fully turbulent boundary layer on suction and pressure side. Boundary layer tripping was applied close to the leading edge using a zigzag tripping band on suction side at $x/c = 0.02$ with a thickness of 0.7 mm in LBM and 0.6 mm in the experiment. On the pressure side the tripping was located at $x/c = 0.05$ with a thickness of 0.7 mm in both LBM and experiment.

It is important to note that the baseline airfoil operated at the standard conditions, as specified above, is not expected to produce the tonal trailing edge noise.

The verification is confined to (i) a rudimentary mesh refinement study and (ii) the variation of the spanwise computational domain. Validation efforts comprise comparisons of the LBM-results with experimental, and partly, with XFOIL data.[2] In Chapter 5, case by case, further comparisons of LBM-predictions with experimental wind tunnel data will be provided.

Finally, a decision is made concerning the mesh topology used to produce the series of results in Chapter 5.

4.1 Mesh configurations studied

In order to obtain certain accuracy in resolving physical acoustic waves numerically usually scientists refer to the modified wave number e.g. by LELE or COLONIUS AND LELE [73, 74]. For LBM, BRÈS [49] provided estimates to guarantee sufficient resolution, suggesting at least 12 to 16 *voxels* per wavelength. The resolution of the turbulent flow structures around the airfoil, however, requires a locally considerably finer mesh. At the microphone positions that allow the direct determination of the far-field noise in the domain, a sufficient resolution was ensured.

The first mesh topology, denoted "Medium I", is characterized by a size of the finest voxels as $\Delta x = 5.86 \cdot 10^{-5}$ m, nine VR zones, and the spanwise extension of the computational domain as $0.1 c_b$. The decision for the finest voxel size, the number of VR zones (but not the topology of the VR zones), and the extension of the domain in spanwise direction were triggered by a preceding similar study by MANEGAR ET AL. [75]. Based on Medium I a second to-

[2] In chapter 5 case by case more comparisons of LBM with experimental data are given.

pology "Medium II" with a doubled spanwise extension of $0.2c_b$ was investigated. Finally, keeping the spanwise extension to $0.1c_b$, the mesh resolution was increased by implementing an additional VR zone (as indicated in the previous chapter), resulting in a size of the finest voxels as $\Delta x = 2.93 \cdot 10^{-5}$ m. This topology is denoted "Fine". Table 3.3 summarizes the parameters of these three different meshes and the resulting number of *voxels*, *surfels*, the time step size, dimensionless wall distance y^+, and the required CPUh per flow pass T_f (as defined in Section 3.3.2). As expected the size of the computational mesh has a very strong influence on the computational time required. For instance, the refinement of the computational domain by an additional VR results in a factor of ten in terms of computational time for one flow pass and the spanwise extension in a factor of two.

Table 4.1: Parameters of the three numerical meshes for verification.

	Medium I	Medium II	Fine
Resolution zones	9	9	10
Finest *voxel* size	$5.86 \cdot 10^{-5}$ m	$5.86 \cdot 10^{-5}$ m	$2.93 \cdot 10^{-5}$ m
Coarsest *voxel* size	$1.5 \cdot 10^{-2}$ m	$1.5 \cdot 10^{-2}$ m	$1.5 \cdot 10^{-2}$ m
Time step size	$9.941 \cdot 10^{-8}$ s	$9.941 \cdot 10^{-8}$ s	$4.971 \cdot 10^{-8}$ s
Number of *voxels*	$360 \cdot 10^6$	$720 \cdot 10^6$	$2{,}104 \cdot 10^6$
Number of *surfels*	$12 \cdot 10^6$	$21 \cdot 10^6$	$42 \cdot 10^6$
Spanwise extension L_{LBM}	$0.1c_b$	$0.2c_b$	$0.1c_b$
Dimensionless wall distance y^+	3 - 8	3 - 8	1.5 - 4
CPUh/flow pass T_f	$1.7 \cdot 10^3$	$3.4 \cdot 10^3$	$17.5 \cdot 10^3$

4.2 Results

4.2.1 Static pressure distribution

Figure 4.1 shows the static pressure distribution in terms of the pressure coefficient on the airfoil pressure and suction sides, obtained with the three different numerical meshes. The pressure coefficient does not appear to be sensitive to the mesh resolution or the spanwise extension.

4.2.2 Wall pressure spectrum

Figure 4.2 and Figure 4.3 present the spectra of the time-dependent surface pressure fluctuations on the suction and pressure side in the vicinity of the trailing edge, more precisely at $x/c = 0.93$. It should be mentioned that the sampling rate of the configuration Fine is twice as

high as those of medium I and II. A first observation is that over the entire frequency range, the LBM-predictions are not affected substantially by the different mesh topologies, in other words, the mesh "Medium I" seems to be adequate. Secondly, the agreement with the experimental data is satisfactory which is seen as a successful validation of the prediction.

Further proof of plausibility is the fact that the levels decay from 2 kHz to 10 kHz proportional to f^{-2}, beyond 10 kHz to f^{-5}. This behavior has been found for fully turbulent boundary layers by several authors [11, 76].

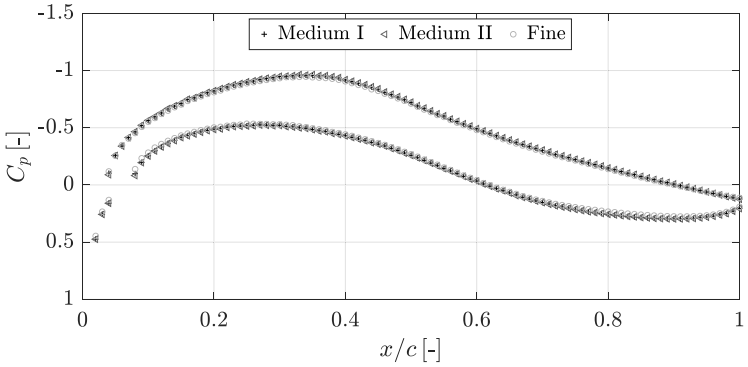

Figure 4.1: Pressure coefficient of suction and pressure side obtained with the three numerical meshes.

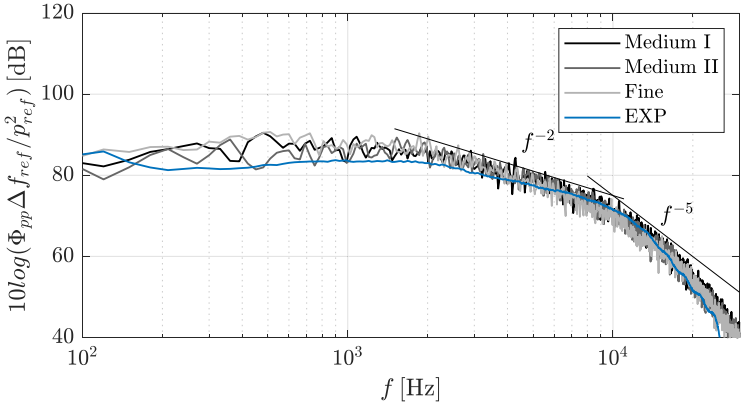

Figure 4.2: Surface pressure fluctuations on the suction side at *x/c* = 0.93 for different mesh topologies and experiment.

4.2.3 Spanwise correlation length and coherence

An adequate mesh resolution is required to accurately capture the spatial variations of the pressure fluctuations and to correctly represent the correlations along the span. If the mesh is chosen too coarse, the spatial variations of the flow structures may not be properly captured and the simulation results may be inaccurate. On the other hand, if a too-fine mesh is chosen, then unnecessary computational resources and memory are required without providing significant improvements in the simulation results.

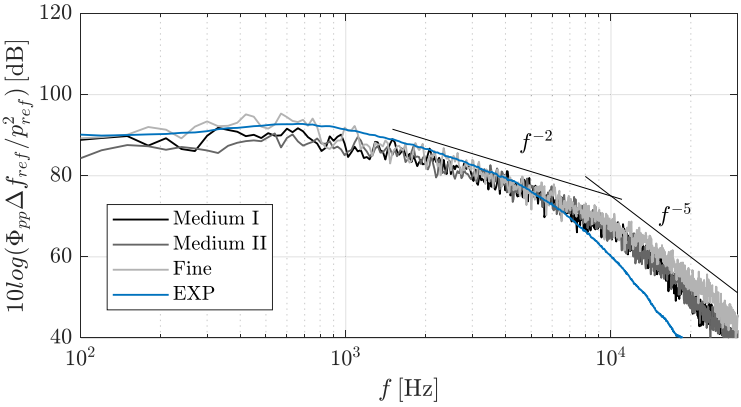

Figure 4.3: Surface pressure fluctuations on the pressure side at x/c = 0.93 for different mesh topologies and experiment.

Figure 4.4 shows the spanwise correlation length on the pressure and suction side at a position x/c = 0.93 as a function of frequency. The comparison of the results with the "Medium I" and "Fine" mesh topologies shows on the suction side that the correlation length for the finer

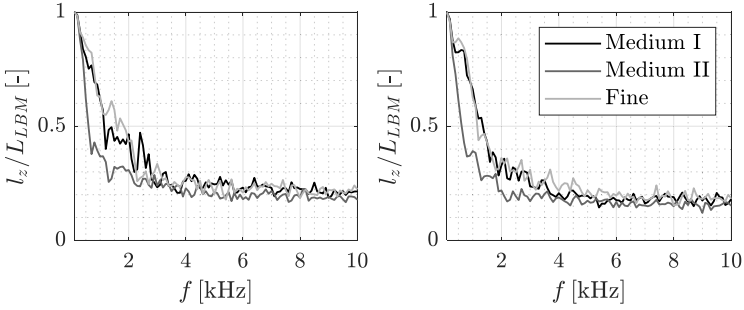

Figure 4.4: LBM-predicted spanwise correlation length for Medium I, II, and Fine mesh topology close to the trailing edge at x/c = 0.93 for suction (left) and pressure side (right).

mesh is higher between 1 kHz and 2 kHz. Beyond 2 kHz, the correlation length of the finer mesh decreases faster before it follows the course of the Medium I mesh. For the pressure side, there are only minor differences between the Medium I and Fine mesh topologies.

This indicates a sufficient resolution of the turbulent structures already with the coarser mesh "Medium I". If the results for different spans, i.e. "Medium I" and "Medium II", are compared, a faster decay of the correlation length with 0.2c span can be seen until finally, all curves coincide at about 3 to 4 kHz.

Figure 4.5 shows the contour plots of the pressure coherence along the spanwise coordinate z with the spacing η = 0.5 mm as a function of frequency. The signal from mid-span position is taken as the reference signal.

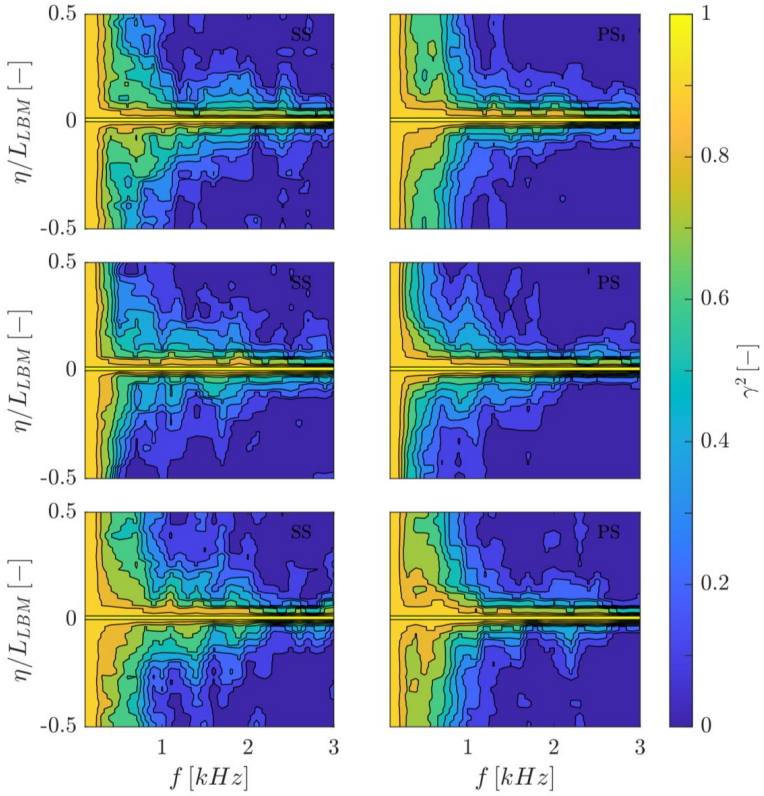

Figure 4.5: Spanwise coherence of time-dependent surface pressure fluctuations for Medium I, II, and Fine mesh topology close to the trailing edge at x/c = 0.93 for suction and pressure side.

Both, mesh "Medium I" and "Fine" yield quantitatively the same pattern which again indicates that the resolution of the turbulent structures with the coarser mesh is sufficient. The effect of spanwise extension of the computational domain - from $0.1c_b$ with "Medium I" to $0.2c_b$ with "Medium II", results in a stronger decrease of the coherence towards the edges. This is to be expected since larger structures can also be captured with a larger span.

4.2.4 Boundary layer and wake characteristics

Since no experimental data are available, the LBM-predicted boundary layer parameters are compared with results from XFOIL [77]. Based on the time-averaged velocity field, Figure 4.6 depicts the boundary layer thickness δ_{99} and displacement thickness δ^*, calculated via Equations 3.2 and 3.3, and from XFOIL. Comparing the results of the different mesh topologies, neither the element size nor the expansion in the spanwise direction have a substantial effect on the boundary layer thickness.

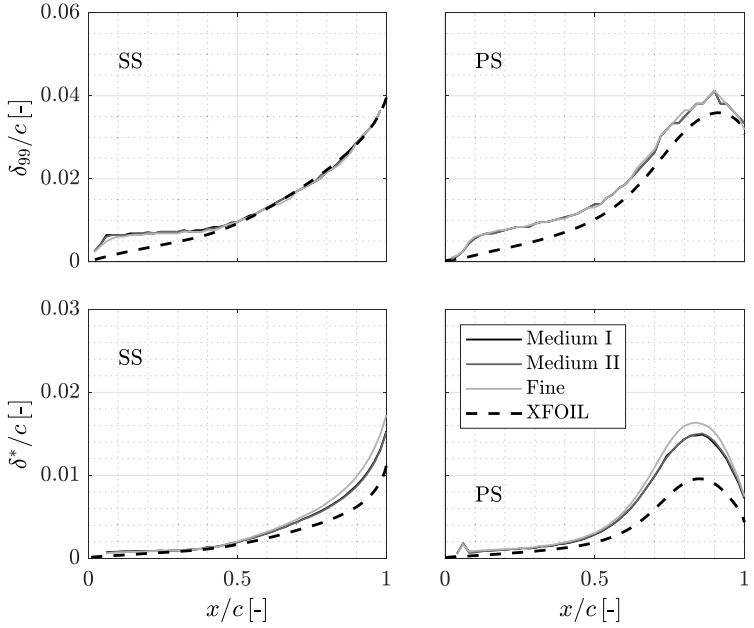

Figure 4.6: Boundary layer and boundary layer displacement thickness along chord for suction (left) and pressure side (right).

The comparison of the boundary layer parameters with XFOIL shows only a good agreement for the boundary layer thickness on the suction side from a position of $x/c = 0.5$. The boundary layer thickness on the pressure side shows the same behavior but deviates quantita-

tively. The differences between simulation and XFOIL could be due to the different ways of forcing the laminar-turbulent transition. In the simulation, a zigzag band with a geometric height is used. In the XFOIL simulation, the laminar-turbulent transition at the specified position is enforced without tripping band or the equivalent geometrical add-ons.

Figure 4.7 shows the time-averaged velocity $\overline{u}$ distribution normalized with the free-flow velocity u_∞. LBM- and experimental hot wire data are plotted for different distances Δx downstream of the trailing edge. Similarly to what was observed for the boundary layer thickness and displacement thickness, there is no significant effect of the mesh topologies utilized. However, the wake deficit captured from the experimental hot-wire measurements reveals small differences in the near-wake region. It is slightly smaller than the numerically predicted, particularly on the suction side. It is hypothesized that those differences are caused by the upstream suction-side boundary layer thickness which is predicted too large by LBM. In the far wake, however, the differences between experiment and simulation become negligibly small.

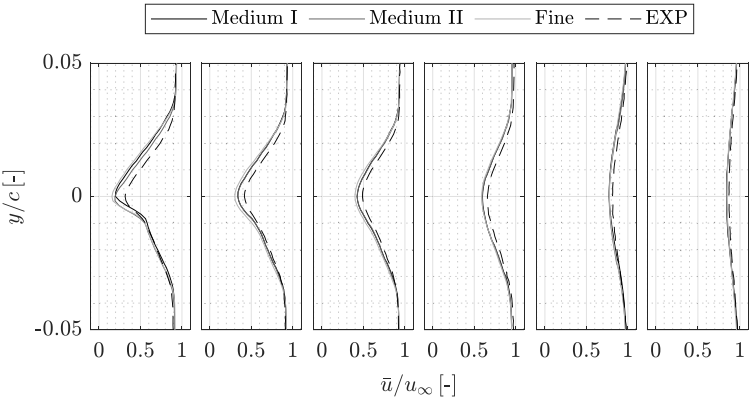

Figure 4.7: Mean velocity distribution in the wake for experiment, Medium I, Medium II, and Fine LBM simulation for various distances from the TE from left to right: *x/c* = 0.025, 0.042, 0.058, 0.158, 0.625, and 1.03.

In Figure 4.8 the power spectral density of the fluctuations of the velocity component u (parallel to the undisturbed flow u_∞) as a function of the height y at various distances x from the TE are plotted. Again, the effect of refinement is marginal, and the comparison with experimental data is favorable. In the experimental results, the tones at about 2 kHz, 3 kHz, and 5 kHz are due to vortex shedding which is caused by the probe holder positioned in the flow.

4.2.5 Far-field noise

The far-field noise at monitoring points ("probes", see Section 3.3.2), obtained via a direct noise calculation (DNC) and with the Ffowcs Williams & Hawkings(FW-H) model, is con-

sidered in Figure 4.9. The gray areas indicate the frequencies where the results are not reliable: In the low-frequency range due to limited physical simulation time; in the high-frequency range due to the voxel size which results in a cut-off frequency of about 5 kHz.

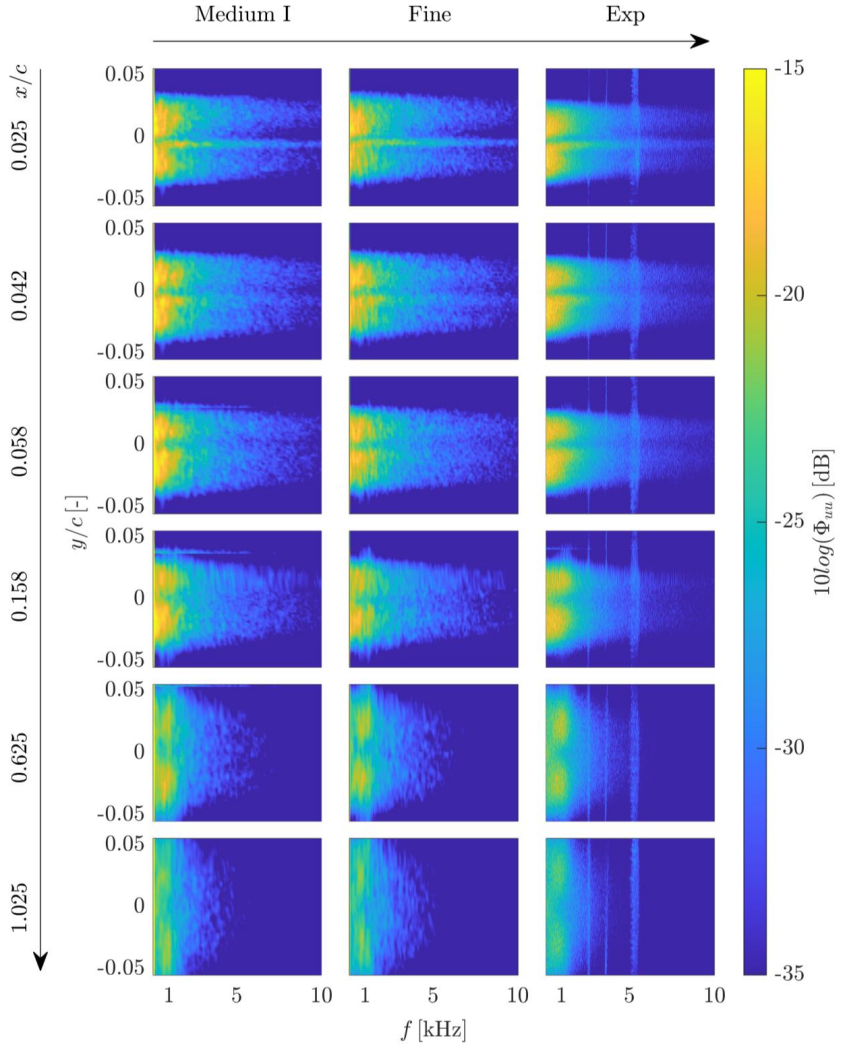

Figure 4.8: Power spectral density of the fluctuations of velocity component u (parallel to the undisturbed flow) in the wake region.

The jump in the high-frequency region of the Medium II configuration is due to the number of voxels per wavelength and reaching the cut-off frequency (see Section 3.3.2). The agreement between the spectra is very favorable. Hence, from an acoustic point of view, the Medium I mesh topology is sufficient.

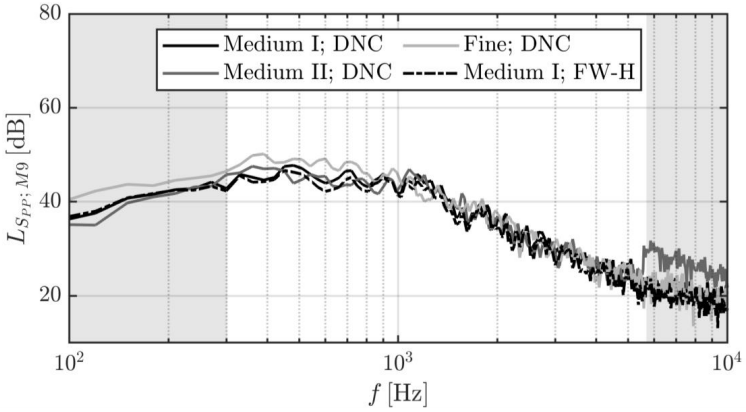

Figure 4.9: LBM-predicted far-field noise; comparison of a direct noise calculation (DNC) with results from a FFOWCS WILLIAMS and HAWKINGS far-field (FW-H) analysis.

Figure 4.10 presents the LBM far-field noise prediction with "Medium I" and the measured far-field noise and background noise (BGN) (microphone position M9, see Figure 3.11). For the frequency range in which the airfoil's self-noise is separable from the background noise, the spectral power densities are in qualitative agreement.

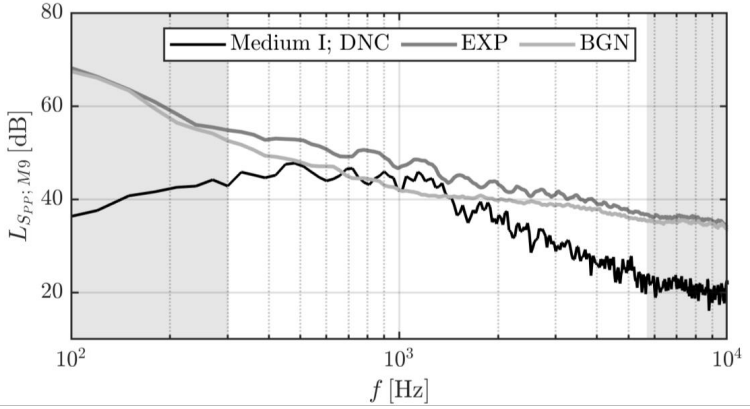

Figure 4.10: LBM-predicted far-field noise; comparison with experimental data and wind-tunnel background noise (BGN).

Quantitatively, the far-field noise is somewhat underestimated in the simulation. Potential causes for this are elaborated at the end of Section 5.1.1. The gray areas show the frequencies at which the far-field noise differs by less than 3 dB from the BGN of the wind tunnel and thus an interpretation or comparison of the far-field noise in this range is not reliable.

4.3 Intermediate conclusion

The objective of this Chapter was to verify and validate the numerical LBM results. For the baseline airfoil section, operated at standard conditions, time-averaged and fluctuation boundary layer parameters in the vicinity of the trailing edge, the flow field in the wake, and the far-field acoustic field were considered. Within the rudimentary mesh refinement study, it became obvious that the LBM results, obtained with the coarsest numerical mesh investigated, can hardly be improved by a finer mesh. A second finding of the study concerns the size of the computational domain. As could be seen by comparing to the other simulations, the spanwise extension of the airfoil section $L_{LBM}/c_b = 0.1$ is sufficient. Hence, for all further simulations the mesh "Medium I" will be chosen. This helps to confine the (still very large) computational effort and eventually to study the effect of parameters such as trailing edge thickness, airfoil loading, etc. more systematically.

5. Results: Far-field acoustics and unsteady flow field

5.1 Acoustic far field

5.1.1 Spectra

In this thesis, the far-field noise emitted from the airfoil in the flow is of primary interest. Parameters studied are the airfoil's trailing edge geometry and the airfoil operating point, more specifically the trailing edge thickness-to-chord ratio t^*, the airfoil loading (i.e. the effective angle of attack α_e), and the chord-based REYNOLDS number Re_c. If not otherwise stated, the results presented are obtained from the direct noise computation based on the LBM simulation.

Figure 5.1 shows the power spectral density of the far-field noise at position M4 (see Section 3.4.2). The gray areas indicate the frequencies where the results are not reliable for different reasons: In the low-frequency range due to the small spanwise extension of the airfoil section and limited physical simulation time; in the high-frequency range due to the voxel size which results in a cut-off frequency of about 5 kHz. Essential features of the spectra are:

i. As t^* is increased a distinct tone of increasing level appears in the spectrum.
ii. Increasing the chord-based REYNOLDS number Re_c (i.e. the free stream flow velocity) rises the levels of both, the broadband and the tonal spectral components.
iii. It is suspected that the tones - as already pointed out in section 2.3 - are caused by vortex shedding at the trailing edge which can be expected as the trailing edge bluntness is increased. Therefore, provisionally the frequency of the tones is named vortex frequency f_{VS}, i.e. the frequency of the vortices shedded from the trailing edge. In Section 5.2 the analysis of the unsteady flow field in the vicinity of the trailing edge will support this hypothesis.
iv. The frequency f_{VS} increases with t^* and the chord-based REYNOLDS number.
v. Varying the parameters investigated, it is observed that the transition from cases with and without tone is gradual.
vi. Increasing airfoil loading (i.e. α_e) decreases the level of the tone until it is masked by the otherwise unchanged broad band floor.

The far-field noise is relatively easy to measure. Therefore, for additional validation of the LBM results, the measured spectra are depicted in Figure 5.2. Frequency ranges that have a poor signal-to-background noise ratio with less than 3 dB difference between BGN and signal are grayed out. Numeric values of the spectral features are compiled in Table 5.1. Since the BTEN contributions do not occur only at the frequency f_{VS} but rather over a frequency range of $f_{VS}-100$ Hz and $f_{VS}+100$ Hz, the levels of acoustic power of the tones $L_{Spp,VS}$ are obtained by integration of the spectral density over the given frequency range. ΔL_{Spp} is the difference to the baseline case with t^*=0.005 for the respective REYNOLDS number and angle of attack.

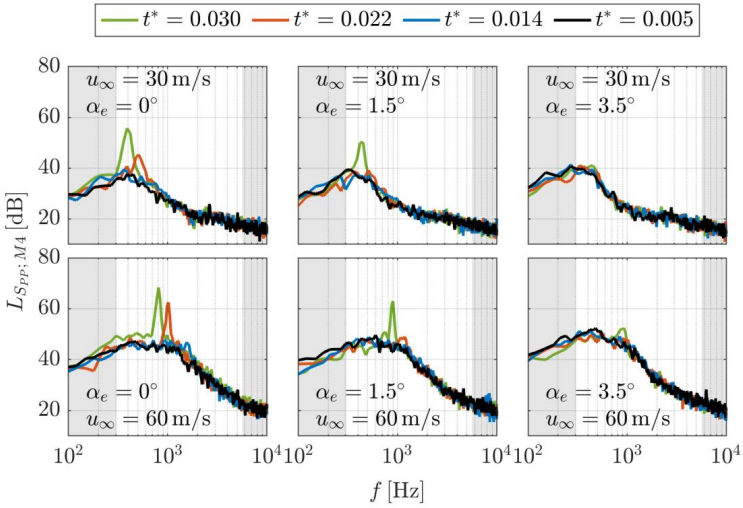

Figure 5.1: Power spectral density of LBM-predicted far-field noise captured at microphone position M4: Effect of trailing edge thickness-to-chord ratio t^*, REYNOLDS number and loading (i.e. α_e).

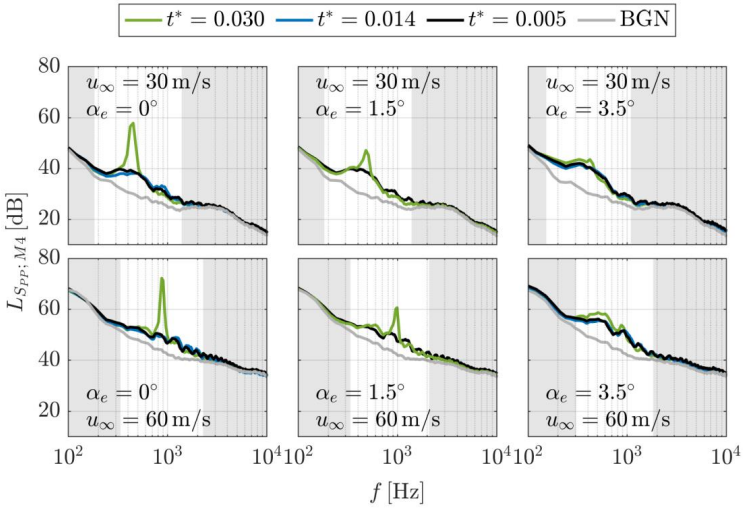

Figure 5.2: As Figure 5.1, but for experimental data.

Table 5.1: Shedding frequency f_{VS}, associated level of power spectral density $L_{Spp,VS}$ (integrated from f_{VS} - 100 Hz to f_{VS} + 100 Hz), and ΔL_{Spp} (which is the difference to the baseline case with t^*=0.005 for the respective REYNOLDS number and angle of attack).

Case	Configuration				LBM			Experiment		
	α_e [°]	u_∞ [m/s]	t^* [-]	$Re_c \cdot 10^6$ [-]	f_{VS} [Hz]	$L_{Spp,VS}$ [dB]	ΔL_{Spp} [dB]	f_{VS} [Hz]	$L_{Spp,VS}$ [dB]	ΔL_{Spp} [dB]
X	0	60	0.014	1.2	1,560	54	7	1720	50	0
XIII$^+$	0	30	0.022	0.6	510	51	7	No data available		
XIV$^+$	1.5	30	0.022	0.6	510	46	2	No data available		
XVI$^+$	0	60	0.022	1.1	1020	67	14	No data available		
XVII$^+$	1.5	60	0.022	1.1	1170	56	4	No data available		
XIX	0	30	0.030	0.5	390	59	14	440	61	14
XX	1.5	30	0.030	0.5	430	57	13	480	52	5
XXI	3.5	30	0.030	0.5	450	48	2	440	50	2
XXII	0	60	0.030	1.1	810	71	18	880	75	18
XXIII	1.5	60	0.030	1.1	900	66	13	990	65	8
XXIV	3.5	60	0.030	1.1	930	59	5	880	61	2

There are a few quantitative discrepancies between the experimental and the LBM-predicted results. In case XIX the difference in predicted and measured f_{VS} amounts up to 13% (440 Hz vs. 390 Hz). The levels of the tones differ up to 5 dB. The reason for this discrepancy is not known in detail at the moment. Nevertheless, the following issues can be identified and surely contribute to the observed differences:

- The boundary layer or the wake are not fully resolved (see Section 4).
- Boundary conditions of the simulation.
- Manufacturing inaccuracies of the test specimen.
- Fundamental differences between the simulation and the experiment, e.g. the airfoil section in the simulation is placed in an infinitely large space, whereas in the experiment the section is placed in a jet provided by the wind tunnel nozzle.
- Boundary layer tripping; the thickness of the tripping band was carefully chosen for the baseline case, but - depending on the parameters - required various adjustments for both, experiment and simulation.
- Small inaccuracies when setting the angle of attack in the experiment.

- Different inflow conditions (turbulence intensity, velocity distribution) between experiment and simulation.
- Additional side plate – airfoil flow interaction noise in the experiment.

Nevertheless, despite these quantitative differences, the effects of the parameters on the spectrum are well captured by the numerical simulation.

5.1.2 Directivity

The directional characteristics of the tones for two cases are depicted in Figure 5.3. As before, the levels are obtained by integration of the levels in a frequency band between f_{VS} – 100 Hz and f_{VS} + 100 Hz. In the LBM prediction, the data are captured from 72 probes, uniformly spaced at a radius of R_{LBM} = 0.72 m every 5 degrees around the trailing edge. In the experiment, 12 microphones were used facing the TE with a distance of R_{EXP} = 1m, as seen in Figure 3.11. Both data, experimental and numerical, have been scaled to a uniform span of L_{ref} = 1 m and observer distance of R_{ref} = 1 m. The predicted and measured directional patterns agree very well. Obviously, the tones are of dipole nature with forward directivity as with any typical scattering problem.

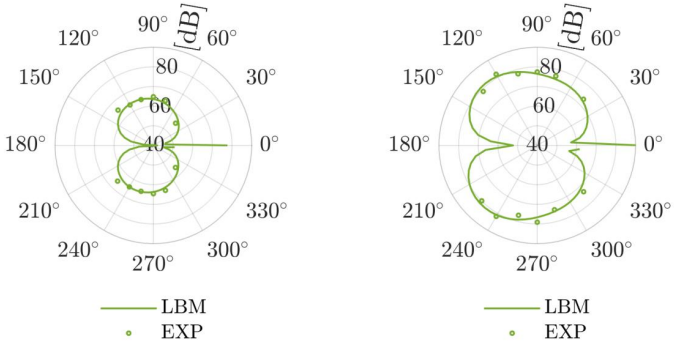

Figure 5.3: Directivity of the tones at u_∞ = 30 m/s (left) and 60 m/s (right); t^* = 0.030, α_e = 0°; results from experiment and LBM simulation.

5.2 Flow field

5.2.1 Velocity field near the TE

Figure 5.4 depicts time-averaged data in the vicinity of the trailing edge by contour plots of the streamwise velocity component *u*. The streamlines, shown in black, are calculated from *u* and *v* as well as the isocontour indicated by the gray dashed line for *u* = 0 m/s. The isocontours are intended to provide information about the recirculation zone behind the TE. The spatial discretization is 0.234 mm in *x* and *y*-direction. Clearly, the recirculation zone grows with

increasing angle of attack and trailing edge thickness-to-chord ratio t^*. In case of the sharp TE ($t^* = 0.005$) and $\alpha_e = 0°$ the recirculation zone contains one vortex, but as t^* is increased, gradually a second vortex develops. Furthermore, it can be observed that the suction side vortex is always located directly behind the trailing edge. The pressure side vortex moves downstream with increased airfoil loading (α_e) and decreased t^*. In order to directly identify configurations with a BTEN contribution, the trailing edges were marked in Figure 5.4, Figure 5.5, and Figure 5.6 according to Table 5.1. A distinction was made according to the type of BTEN contribution, the symbol ● was added for a very pronounced tonal versus • for a comparatively weak and less tonal contribution.

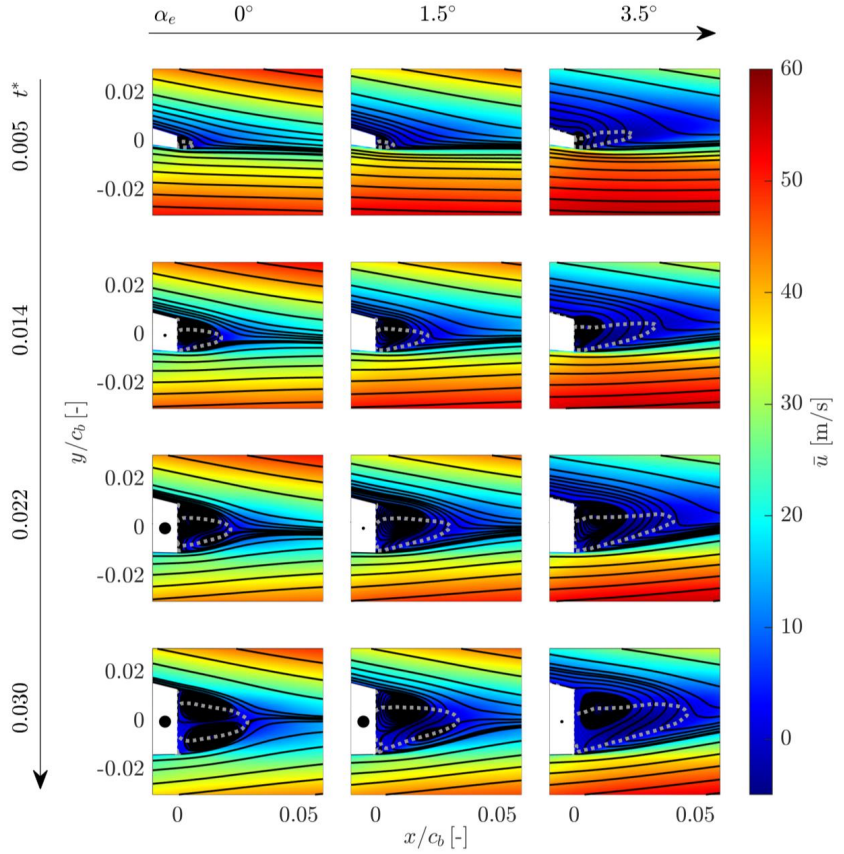

Figure 5.4: Time-averaged data in the vicinity of the trailing edge: colored by the velocity component u, streamlines of the components u and v (black) and isocontours (dashed gray) for $u = 0$ m/s (configurations with a BTEN contribution are marked with ● for a significant strong tonal contribution and • for a comparatively weak and less tonal contribution).

The root-mean-square maps of the velocity fluctuations u'_{rms} are plotted in Figure 5.5. In general larger u'_{rms} indicates higher levels of fluctuations. The dashed lines indicate the loci of maximal RMS-values. For $\alpha_e = 0°$ and a high degree of bluntness, the pattern of the wake is mostly symmetrical. On the other hand, when α_e is increased to 3.5°, the near wake becomes more asymmetric. The suction-side activity in the wake decreases or shifts further downstream. The arrows point to regions of highest fluctuations in the immediate vicinity of the TE. They occur for $\alpha_e = 0°$ and are assumed to be responsible for the tonal noise emitted.

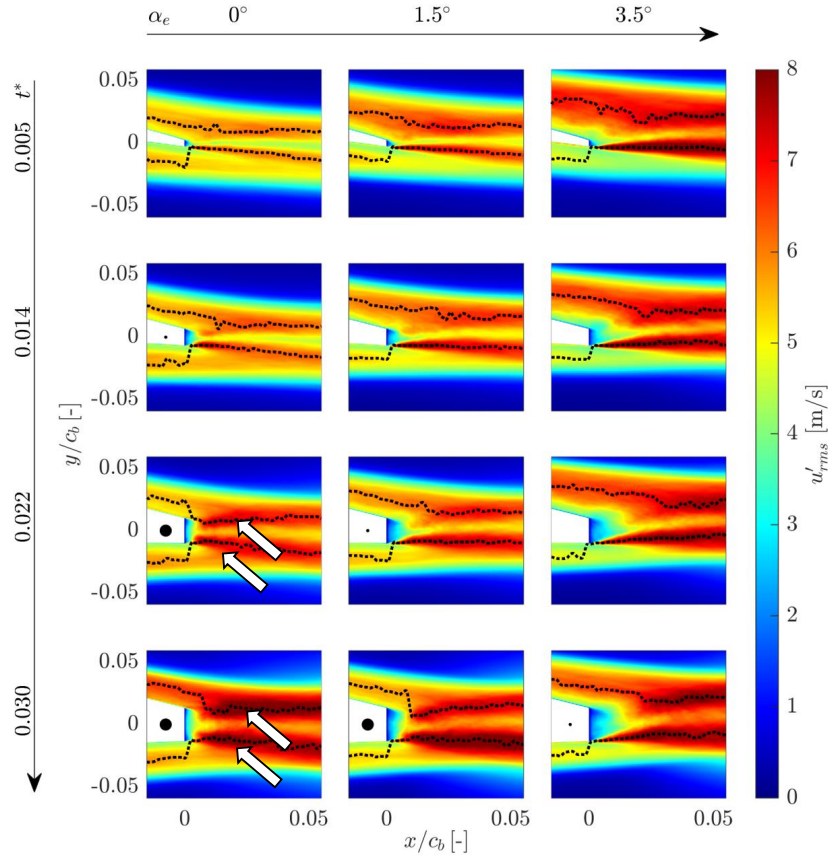

Figure 5.5: Root-mean-square of the fluctuating velocity component *u;* the dotted lines indicate loci of maximal RMS-values, the arrows point to two regions of highest fluctuations in the immediate vicinity of the TE and hence are assumed to be responsible for the tonal noise emitted (configurations with a BTEN contribution are marked with ● for a significant strong tonal contribution and • for a comparatively weak and less tonal contribution).

Finally, in Figure 5.6 the time-averaged product of the fluctuating velocities $\overline{u'v'}$ (proportional to the REYNOLDS stress component $\tau'_{xy} = \rho\overline{u'v'}$) is provided. These plots support the previous findings.

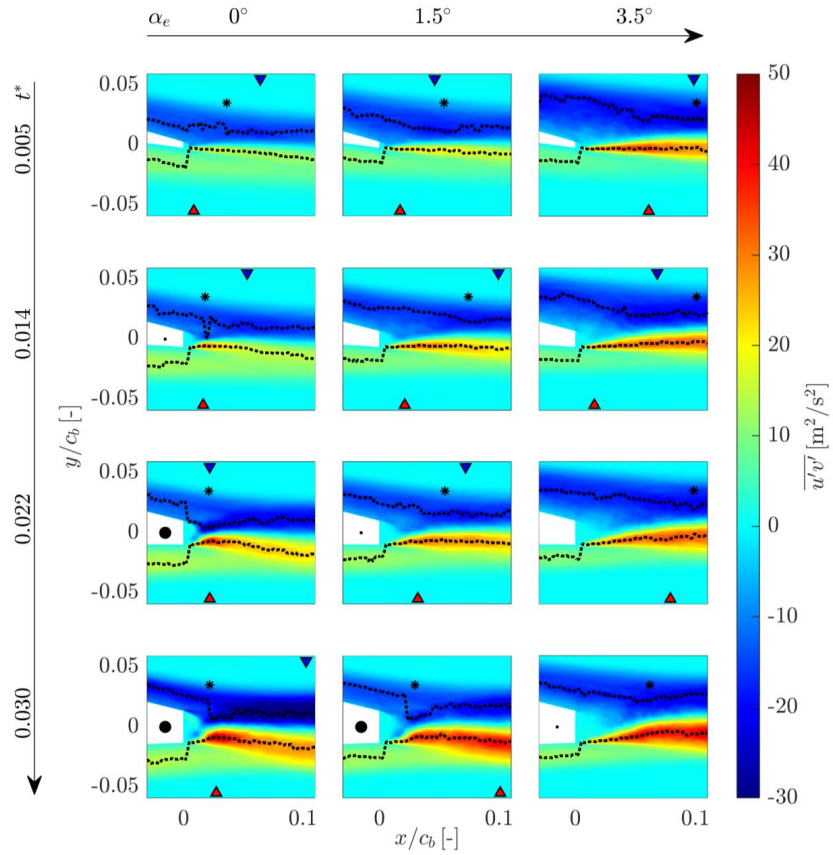

Figure 5.6: Maps of REYNOLDS stress $\overline{u'v'}$, the dotted lines indicate loci of minima and maxima values on SS and PS, the different markers indicate x/c_b positions: ▼ for the smallest minimum within the wake on the suction side, ▲ for the largest maximum within the wake on the pressure side and * for the smallest distance between SS minimum and the PS maximum (configurations with a BTEN contribution are marked with ● for a significant strong tonal contribution and • for a comparatively weak and less tonal contribution).

The black dotted lines show the course of the minimum values on the suction side and the maximum values on the pressure side for the REYNOLDS stresses. In addition, different x/c_b positions are marked in the plots. The triangular markers indicate with ▲ and ▼ where the

magnitude of the maxima and minima are located, respectively. With * those x/c_b positions are marked, where the distance between suction side minimum and pressure side maximum is the smallest.

The color gradient shows that the absolute values for all configurations are higher on the pressure side, which is due to the asymmetry of the airfoil and its influence on the flow. Considering the pressure side loci of the extrema values, a discontinuity appears for all configurations. This occurs within the shear layer shortly after the trailing edge. Similar discontinuities can be observed on the suction side, but only with a high degree of bluntness and under low loading conditions, or in other words, only for cases with a pronounced BTEN contribution. In case this occurs, the location is found usually further downstream than the pressure side discontinuity, and a constricted region is obtained before the distance between the loci of the maxima and minima diverge again downstream. This constricted region indicates most likely the region of the first fully formed vortices responsible for BTEN. The triangular markers illustrate that for very few configurations the maxima and minima are found at the same x/c_b position in the wake. This complicates the determination of y_f according to Section 2.2, where y_f is the distance between the two inflection points (at which the velocity fluctuations reach their maximum) in the velocity profile of the wake. The different positions of the absolute maximum values can also be attributed to the asymmetry of the flow. For this reason, the minimum distance between minimum and maximum is chosen as the characteristic length of the wake y_f at this point. The pressure side position of the maximum often occurs at a similar position, but on the suction side, it is often much further downstream.

Table 5.2 compiles numerical quantities of different boundary layer parameters (see Section 2.3), derived from the LBM-predicted flow fields. The bluntness parameter BP is evaluated as well. Cases with distinct tones in the far-field noise are printed in bold. For configurations with BTEN contribution, the parameters y_f and the distance to the trailing edge l_f, at which y_f was determined, are also given. Although the bluntness parameter BP initially seemed to be a very conservative indicator for the occurrence of tonal BTEN (since it only takes into account the averaged boundary layer displacement thickness of the suction and pressure sides), this parameter appears to be a suitable metric: For $BP > 0.3$ tones occur, as already stated by BLAKE [11]. However, this is only true for relatively low loading of the airfoil. Increased loading renders the tonal BTEN to disappear, even if $BP > 0.3$.

A frequency analysis of the velocity component u in the near wake as a function of y (see Section 3.4.2) at various streamwise distances to the trailing edge of x/c_b is depicted in Figure 5.7. Please note that the chord length of the unmodified airfoil c_b was used for non-dimensionalization of the lengths.

Basically, one very strong vertical peak identical with amplitude to the extend of the chord (y/c_b=0) can be detected for low aerodynamic loading condition at all distances to the TE. This peak agrees very well with the shedding frequency of f_{VS} = 810 Hz observed in the far-field spectra in Figure 5.1. The peaks continue even beyond the wake boundary, regardless of the distance to the trailing edge, and are always stronger on the pressure side.

Table 5.2: BL thickness δ, BL displacement thickness δ^* at trailing edge position for suction and pressure side as well as BP and the distance y_f and the position l_f (Note: For configurations with a BTEN contribution, the BP parameter is displayed in bold).

Case	t^*	α_e	u_∞	Re_c	δ_{SS}	δ^*_{SS}	δ_{PS}	δ^*_{PS}	BP	y_f	l_f
	[-]	[°]	[m/s]	[-]	[mm]	[mm]	[mm]	[mm]	[-]	[mm]	[mm]
I	0.005	0	30		12.8	5.1	10.5	2.4	0.100		
II	./.	1.5	./.		14.2	6.3	9.6	1.7	0.094		
III	./.	3.5	./.		18.5	9.3	8.6	1.0	0.073		
IV	./.	0	60		11.9	4.6	9.6	2.2	0.111		
V	./.	1.5	./.		13.8	6.0	8.6	1.6	0.098		
VI	./.	3.5	./.		15.6	8.1	7.4	0.9	0.083		
VII	0.014	0	30		11.9	3.9	10.5	2.8	0.298		
VIII	./.	1.5	./.		12.5	5.2	9.6	2.1	0.276		
IX	./.	3.5	./.		16.1	8.0	7.7	1.4	0.213		
X	./.	0	60		10.5	3.6	10.0	2.6	**0.325**	2.3	5.5
XI	./.	1.5	./.		12.4	5.1	8.1	1.8	0.291		
XII	./.	3.5	30		13.8	6.8	7.2	1.2	0.249		
XIII	0.022	0	30		11.0	3.4	10.5	3.1	**0.306**	3.7	6.6
XIV	./.	1.5	./.		11.9	4.4	9.6	2.4	**0.294**	3.5	9.2
XV	./.	3.5	./.		14.2	6.6	8.1	1.5	0.236		
XVI	./.	0	60		9.6	3.0	9.6	2.7	**0.349**	3.3	6.4
XVII	./.	1.5	./.		11.0	4.5	8.1	2.0	**0.305**	6.3	16.5
XVIII	./.	3.5	./.		14.2	7.0	7.0	1.4	0.238		
XIX	0.030	0	30		10.5	3.1	11.0	3.3	**0.625**	4.5	7.3
XX	./.	1.5	./.		11.0	3.7	9.1	2.5	**0.646**	4.2	8.0
XXI	./.	3.5	./.		13.8	6.3	8.1	1.8	**0.490**	8.0	15.3
XXII	./.	0	60		9.6	3.0	9.6	2.8	**0.693**	4.5	6.6
XXIII	./.	1.5	./.		10.0	3.7	8.6	2.2	**0.675**	4.5	9.0
XXIV	./.	3.5	./.		12.4	5.9	7.0	1.5	**0.540**	6.8	18.6

This is a remarkable observation that indicates that the velocity field is excited at this specific frequency f_{VS}. This is contrasted with the findings for a high airfoil loading in the right column of Figure 5.7, where the asymmetric pattern is noticeable at first. For the smallest distance x/c_b to the TE, a peak is observed in the lower shear layer, but this is not spatially extended beyond the limits of the wake. In contrast, for larger distances from the trailing edge, the typical VS peak with spatial extension can be observed even for high loading of the airfoil. This suggests that the coherent structures are located further downstream due to the change in airfoil loading.

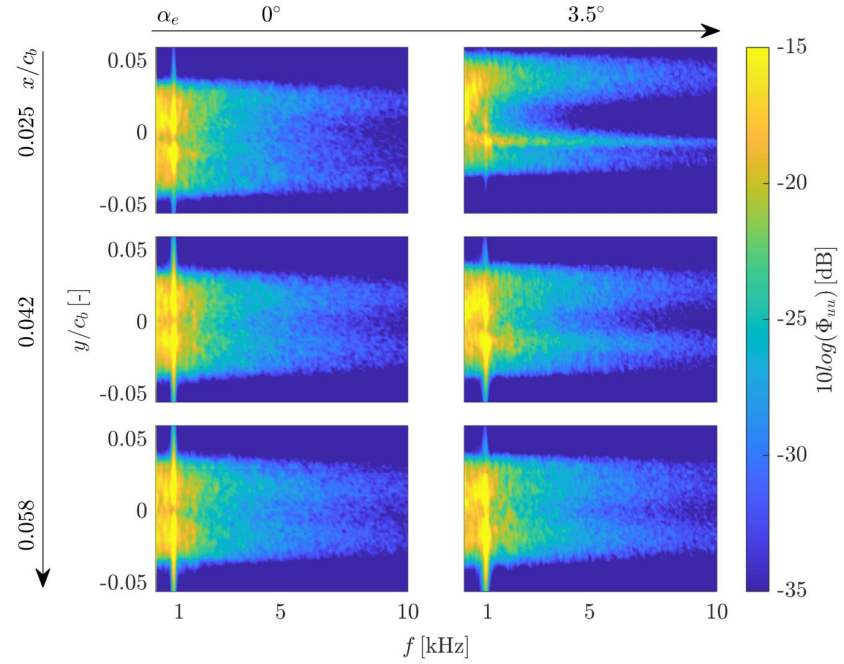

Figure 5.7: LBM-predicted power spectral density of the velocity component u at different distances to the trailing edge x/c_b indicated by the left arrow for case XXII and XXIV (t^* = 0.030, u_∞ = 60 m/s, α_e = 0° and 3.5°).

A preliminary conclusion is that in case of a high degree of TE bluntness and comparably small aerodynamic loading of the complete airfoil, the flow structures typical for vortex shedding are close to the trailing edge. On the other hand, increasing loading by increasing the angle of attack shifts the vortex structures away from the TE, resulting in less or no tonal noise emitted from the TE region. Hence, the tones observed in this numerical and experimental study are most likely caused by a strong interaction of shedded vortices with the airfoil trailing edge, in other words: they are the well-known blunt trailing edge noise (BTEN).

5.2.2 Surface pressure fluctuations

Figure 5.8 depicts the power spectral density of the surface pressure fluctuation obtained from the LBM simulation very close to the TE, i.e. at a position of $x/c_b = 0.98$. Similar to the far-field spectra (see Figure 5.1 and Figure 5.2), tonal components are visible for the same combinations of parameters as in acoustic spectra. It seems that the broadband pressure fluctuations tend to mask the tonal components more than in the far-field noise pressure spectra. Figure 5.9 displays the surface pressure fluctuations at a more upstream position of $x/c_b = 0.87$.

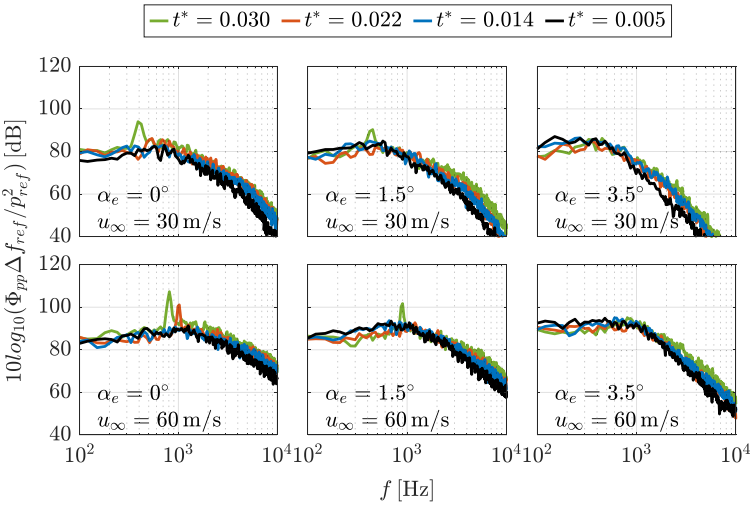

Figure 5.8: Power spectral density of LBM-predicted surface pressure fluctuations on the suction side at $x/c_b = 0.98$.

5.2.3 POD and SPOD analysis

5.2.4 Data acquisition

The POD analysis is applied to the numerical data from the LBM simulations. For this purpose, special measurement planes were selected according to the type of data. As can be seen in Figure 5.10, these are two different planes, each of which was placed in the spanwise center of the domain. Plane A is designed to capture the x- and y-velocity components u and v, respectively. Since the data close to the trailing edge and in the near wake are of particular interest, a high spatial resolution plane was created around this area. For the data collection of the pressure field, a larger area is of interest, since the propagation of the pressure fluctuation is to be considered. The plane B shown in Figure 5.10 was used for this purpose. Data such as sampling rate, acquisition time, and spatial resolution are summarized in Table 5.3. In order to

link the velocity and pressure fields, care was taken to ensure that the data were synchronously collected for the same time period in the simulation. As Table 5.3 proves, sampling frequencies and acquisition times are identical, although the two planes present different spatial resolutions and do not cover the same spatial extent.

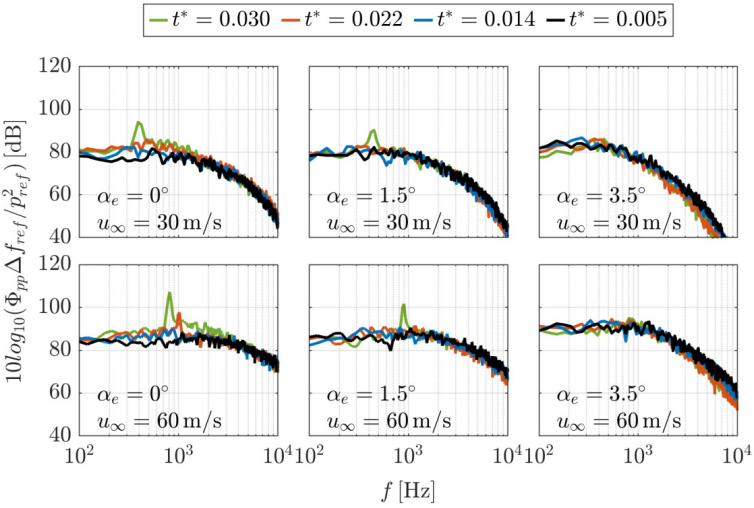

Figure 5.9: As Figure 5.8 but at a more upstream position $x/c_b = 0.87$.

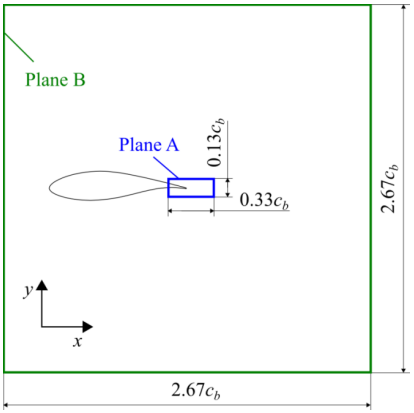

Figure 5.10: Schematic representation of the measurement planes. Plane A (blue) for capturing the velocity and plane B (green) for the static pressure.

Table 5.3: Settings for the data acquisition for POD and SPOD data.

	Plane A	**Plane B**
Data recorded	Velocity	Pressure
Spacing in x and y	0.234 mm	3.75 mm
Number of points N in x and y	429x173	215x215
Sampling frequency f_s	39.3 kHz	39.3 kHz
Acquisition time t_s	0.1 s	0.1 s
Snapshots	4,000	4,000

For the SPOD evaluation an overlap of 0.5, the number of blocks $N_b = 5$ has been chosen.

5.2.5 POD

Figure 5.11 illustrates the energy fraction and the integrated energy of the turbulent kinetic energy (TKE) for the first 50 eigenvalue modes obtained. The cases under consideration refer to the low trailing edge-to-chord ratio $t^* = 0.005$ at $u_\infty = 60$ m/s and the angles of attack $\alpha_e = 0°$, 1.5°, and 3.5°. As the loading of the airfoil is increased it can be observed that the first modes increase in energy. This is to be expected, since with increasing angle of attack the boundary layer increases on the suction side and thus large-scale turbulent structures are likely to be present in the investigated area. At the same fundamental level, it should be noted that the energy contributions of the individual modes differ only by a few percent. The fraction of energy per mode slowly decreases with the number of modes, which indicates that there is no major contributor in terms of energy.

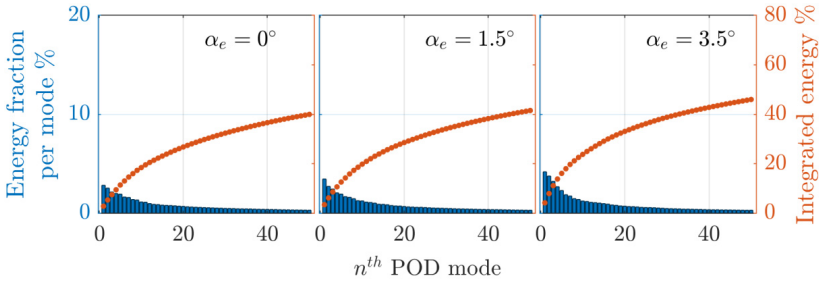

Figure 5.11: Contribution of modes $n = 1$ to 50 to the TKE for the cases with t^*=0.005, $u_\infty = 60$ m/s.

Figure 5.12 illustrates the first six POD modes from the fluctuating velocity field for the cases just discussed. The colormaps are calculated from the velocity u and the arrows represent the modes calculated from u and v.

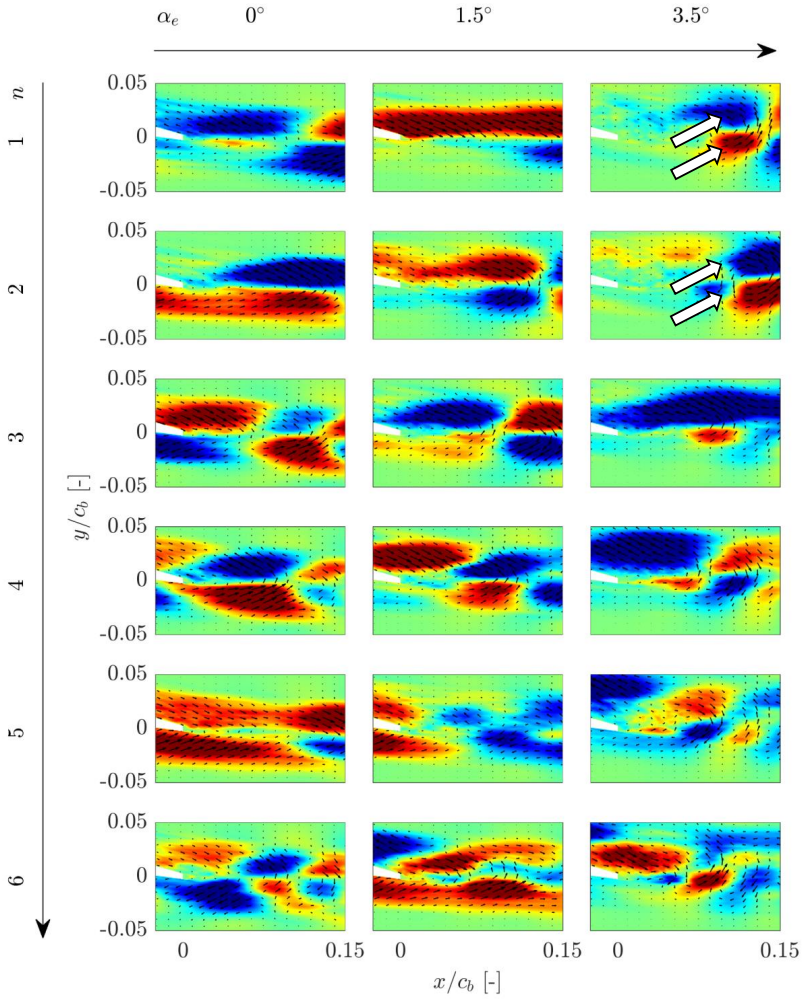

Figure 5.12: Visualization of velocity POD modes $n = 1$ to 6 (from top to bottom) for t^*=0.005, u_∞ = 60 m/s.

In combination with the time evolution of the time coefficient presented in Figure 5.13, the following results can be concluded: The majority of the examined modes are inconspicuous with respect to vortex shedding. For high aerodynamic loading, however, the first two modes

show distinct, organized patterns further downstream in the POD modes indicated by arrows and a periodic course in the time signal of the time coefficient. This vortex shedding is purely aerodynamic in nature and does not contribute to acoustics in the far field.

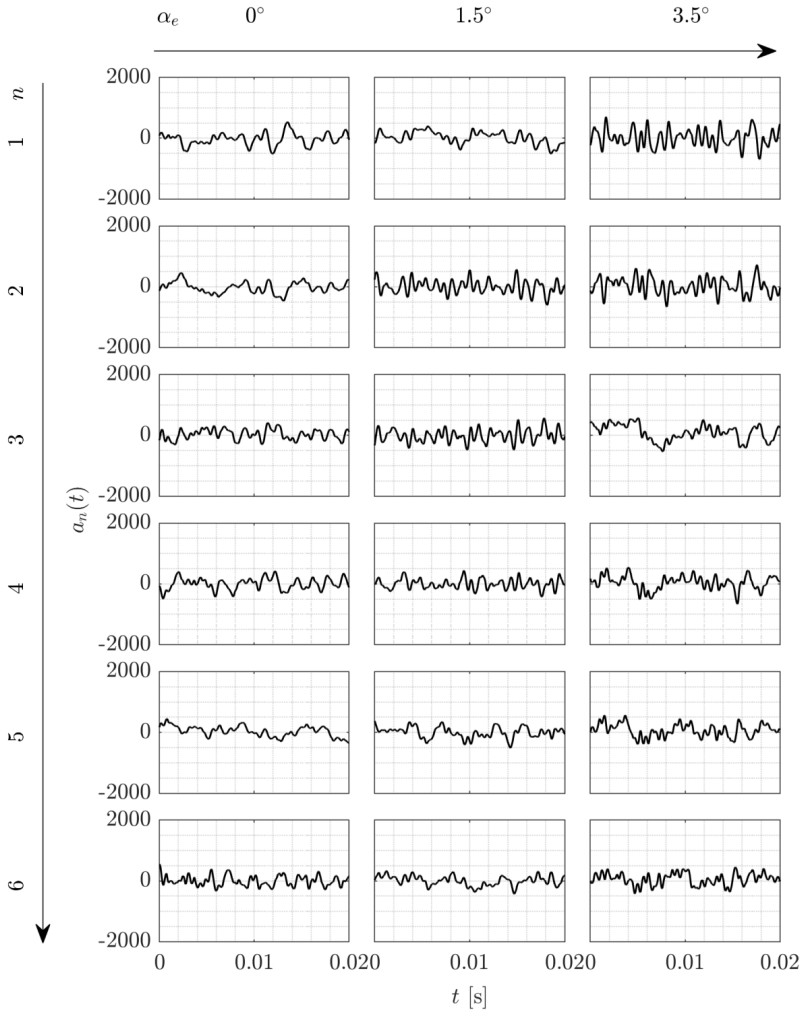

Figure 5.13: Time coefficients a for velocity POD modes n = 1 to 6 (from top to bottom) for t^*=0.005, u_∞ = 60 m/s and angles of attack of α_e = 0° (left), 1.5° (middle) and 3.5° (right).

Comparing these findings to the results of a high degree of bluntness, see Figure 5.14, it is first eye-catching that the distribution of the turbulent kinetic energy gives two main contribu-

tions. This is characterized by the first two modes, which together account for 30% of the total. Regardless of the aerodynamic loading.

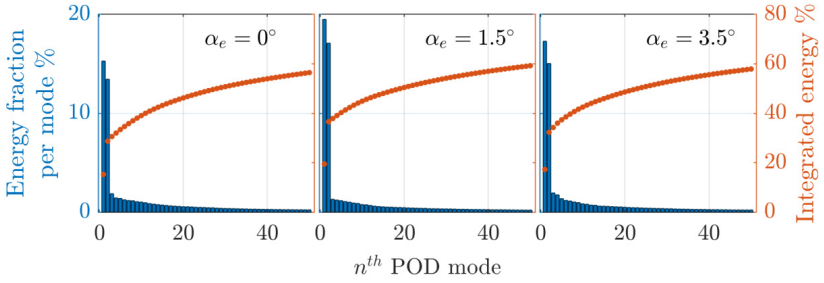

Figure 5.14 Contribution of modes $n = 1$ to 50 to the TKE for the cases with t^*=0.030, u_∞ = 60 m/s.

In Figure 5.15, the first six POD modes of the fluctuating velocity field have been visualized. The colormap gives the modes for the velocity u and the arrows represent the modes calculated from u and v. The first two modes particularly stand out and show organized symmetric repeating patterns for each angle of attack variation. The roll-up process of the vortices is well represented by the arrows. It is worth pointing out that the distance between these structures and the trailing edge increases with the angle of attack. This can be attributed to the recirculation zone, which expands downstream as the angle of attack increases, cf. Figure 5.4. At the same stage, clear BTEN signatures could be identified in the far-field noise of these cases. However, these signatures decreased strongly in level with increasing airfoil loading.

If the time coefficient for these cases is considered, see Figure 5.16, it is not surprising that the first two modes stand out particularly here as well. These modes show strong periodic responses over time of much higher amplitude compared to the following contributors. Additionally, the first and second modes are very similar to each other and seem to differ only in phase. The number of periods per time in Figure 5.16 matches the shedding frequency observed in the far field. At this point, it should be emphasized that the POD analysis is only spatially resolved and frozen in time, which conversely implies that a mode contains several frequencies.

In the following, the POD analysis is now applied to the pressure field of the cases with high degree of bluntness. Figure 5.17 first shows the energy distribution among the individual POD pressure modes. In contrast to the energy distribution of the velocity modes, where the first two modes each account an energy contribution of 13 to 18%, here only the first mode accounts a contribution of 7%, 6.5%, and 3.5% for low to high aerodynamic loading.

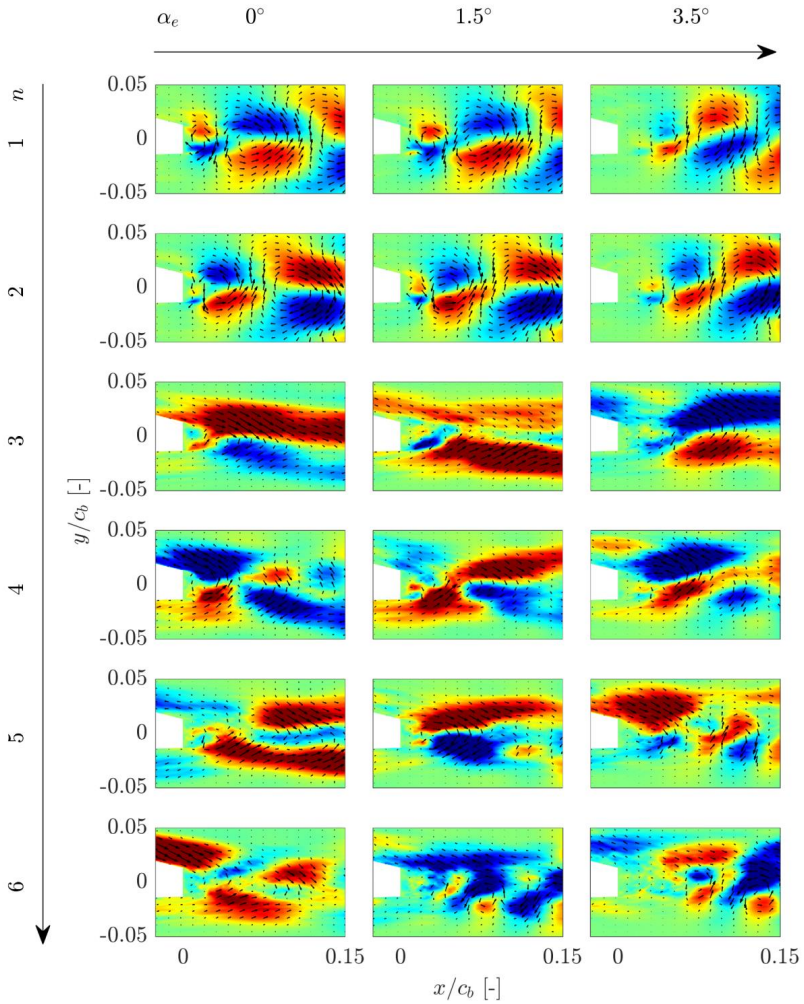

Figure 5.15: Visualization of velocity POD modes $n = 1$ to 6 (from top to bottom) for t^*=0.030, u_∞ = 60 m/s, and angles of attack of α_e = 0° (left), 1.5° (middle), and 3.5° (right).

The time histories of the time coefficients, as seen in Figure 5.18 for modes $n = 1$ and $n = 2$ reveal no dominant periodic behavior for the first modes. This is only observed for modes with less energy content as visible for mode $n = 6$.

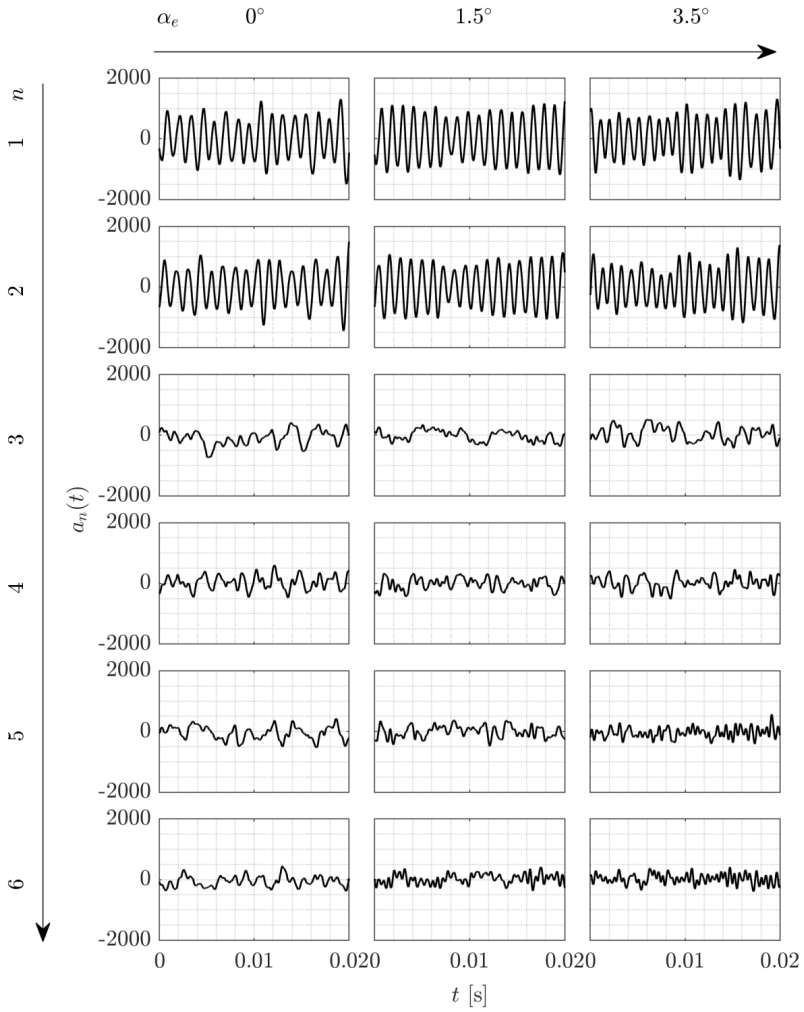

Figure 5.16: Time coefficients *a* for velocity POD modes *n* = 1 to 6 (from top to bottom) for t^*=0.030, u_∞ = 60 m/s and angles of attack of α_e = 0° (left), 1.5° (middle), and 3.5° (right).

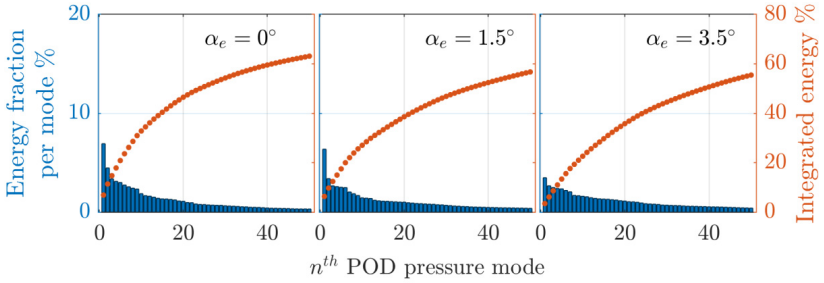

Figure 5.17: Energy distribution of pressure POD modes from n = 1 to 50 for the cases with t^*=0.030, u_∞ = 60 m/s.

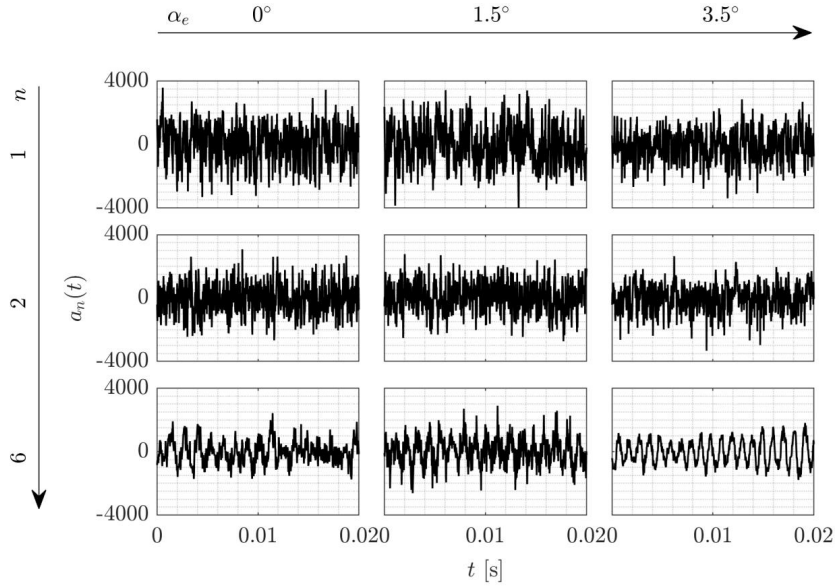

Figure 5.18: Time coefficients a of pressure POD modes n = 1, 2, and 6 (from top to bottom) for t^*=0.030, u_∞ = 60 m/s and angles of attack of α_e = 0° (left), 1.5° (middle) and 3.5° (right).

When reviewing the visualized modes in Figure 5.19, where again the first, second, and sixth mode is depicted for different aerodynamic loading conditions, it can be observed due to the coloring, that the first modes are dominated by the aerodynamic fluctuations in the wake independent on the airfoil loading. This is different for mode six, where aeroacoustic and aerodynamic pressure fluctuations under low airfoil loading have comparable amplitudes. The time coefficient for mode six also shows a periodic behavior, which can be attributed to the

shedding frequency observed in the far-field noise. This mode of propagation corresponds to the typical dipole pattern of the TEN, which propagates from the TE upstream toward the LE. With increasing airfoil load, constant aerodynamic activity in the airfoil wake can be observed for all modes. However, the aeroacoustic decreases with airfoil loading.

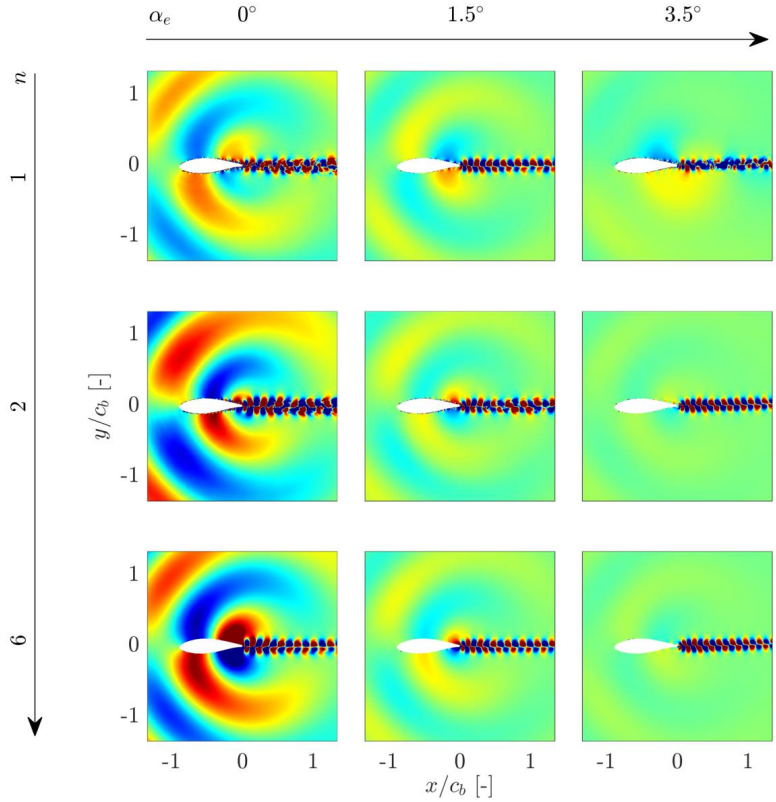

Figure 5.19: Visualization of pressure POD modes n = 1, 2, and 6 (from top to bottom) for t^*=0.030, u_∞ = 60 m/s, and angles of attack of α_e = 0° (left), 1.5° (middle) and 3.5° (right).

In summary, the POD analysis resolves the spatial modes for velocity and the first two determined modes could be related to the BTEN peaks observed in the far field. The POD modes for the pressure fluctuations are strongly dominated by the aerodynamic pressure fluctuations in the wake. Basically, these are of higher magnitude compared to the aeroacoustic pressure fluctuations and hence lead to a different distribution within the modes. Meaning that velocity mode j does not correspond to pressure mode j. This complicates the task of establishing a link between cause and effect, in other words between the coherent structures in the

flow and the propagation of noise. To further study the coherent structures that contribute to the blunt trailing edge noise a SPOD analysis is performed in the next section. With this, it is possible to link the coherent structures in the flow field to the pressure field for a given frequency.

5.2.6 SPOD

In contrast to the POD analysis the SPOD analysis allows to extract not only the spatial structures and their strength, it provides temporal information about the field investigated as well. Thereby it is possible to assign the coherent structures to a frequency or vice versa. For this purpose, the frequency spectrum of the individual velocity and pressure spatio-temporal modes is considered first. The most energetic modes will be investigated further by visualizing them for the frequencies of interest. In a last step, the flow as well as the pressure field will be reconstructed to further analyze the frequency isolated noise sources and their contribution to the overall noise field. The SPOD analysis was first applied to the configurations with low degree of bluntness, high REYNOLDS number $Re_c = 1.2 \cdot 10^{6,}$ and the different airfoil loads. This was done in order to evaluate, compare, and interpret the high bluntness cases on this basis in the subsequent course. The results of all test cases are summarized in Table 5.4.

Figure 5.20 shows the eigenvalue spectra of the five modes for the cases aforementioned. The number of modes is equal to the number of selected blocks, here five, for the DFT. Similar to POD where the modes are sorted in descending order, but here in terms of spectra. The first mode represents the most energetic coherent structure in the flow, while the last mode represents the least energetic structure. The first row contains, as indicated, the results of the SPOD analysis from the velocity field (u component), and the second row the results from the pressure field. The columns represent the considered angles of attack α_e as indicated by the arrow in Figure 5.20. Same as with the POD analysis, there are no conspicuous features in the spectra for low aerodynamic loading. No mode stands out in particular and the energy drop from mode to mode is also uniform. For high aerodynamic loading of the airfoil, a bump is noticeable in the first mode in the frequency range from 1,100 to 1,700 Hz. This is more pronounced in the spectrum of pressure mode one than in mode one of the velocity. This bump is consistent with the observations of the POD analysis, in which vortex shedding typical coherent spatial modes were observed as well as a periodic behavior of the time coefficient for this case.

Next, the energy contributions for a high degree of bluntness are considered. The arrangement of the graphs in Figure 5.21 is the same as in the previously considered spectra. It is evident that the spectra of the first modes have a strong peak which is independent of the loading of the airfoil. This peak is so pronounced in level that it is at least more than an order of magnitude higher than the adjacent region of the spectrum. For higher airfoil loading, the first harmonic ($2f_{VS}$) is also observed which is less prominent. As the airfoil loading increases, these peaks become more broadband. When linking the observed frequencies to the far-field

acoustics, it is to be noted that the monitored BTEN frequency fits regarding frequency to the first peak of mode one.

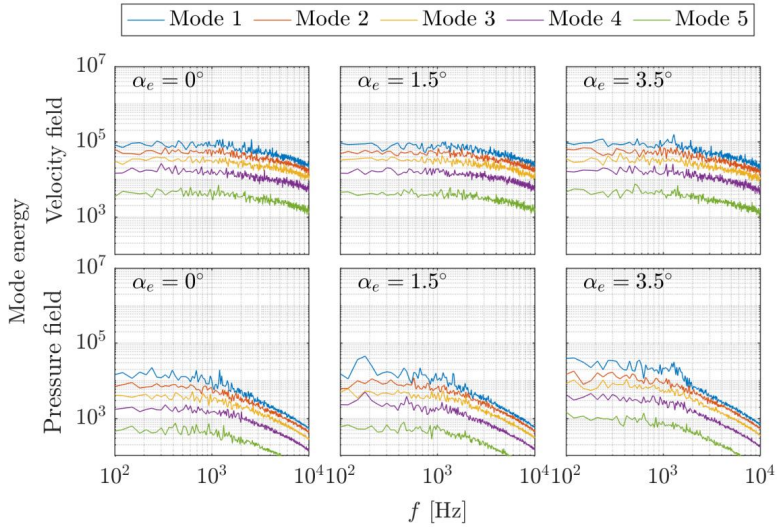

Figure 5.20: SPOD eigenvalue spectra of the five modes of the velocity (top row) and pressure field (bottom row) for t^*=0.005, u_∞ = 60 m/s.

However, the levels in the far-field noise decrease strongly with increasing airfoil loading which is not the case here. Moreover, a harmonic as seen in the SPOD results is not observed in the far-field noise. This is true for the application of the SPOD analysis to the velocity field as well as for the results from the SPOD pressure field.

Table 5.4 provides a direct comparison of the frequencies observed in the far-field noise as well as the frequencies detected from the SPOD analysis. The table also provides the results of the cases that were not shown in detail.

Figure 5.22 presents the velocity mode $n = 1$ for the frequency of the first peak in the first row and the first harmonic in the second for different aerodynamic loadings. The visualization of the modes discloses coherent shedding structures for all angles of attack. As in the POD analysis, it is noticeable that the distance of these structures from the trailing edge increases with airfoil loading.

Besides the fact that the coherent structures form further downstream with increasing angle of attack, it can be observed that the patterns lose symmetry and intensity while increasing the airfoil loading. For the first harmonic, second row of Figure 5.22, the pattern tends to form along a horizontal line starting at the pressure side trailing edge. In this region, enhanced activity has already been observed with the mean values of the REYNOLDS stress, see Figure 5.5

and for u_{rms} Figure 5.6. It is also noticeable that the corresponding opposite pole, i.e. the full pattern, is located further downstream for $2f_{VS}$.

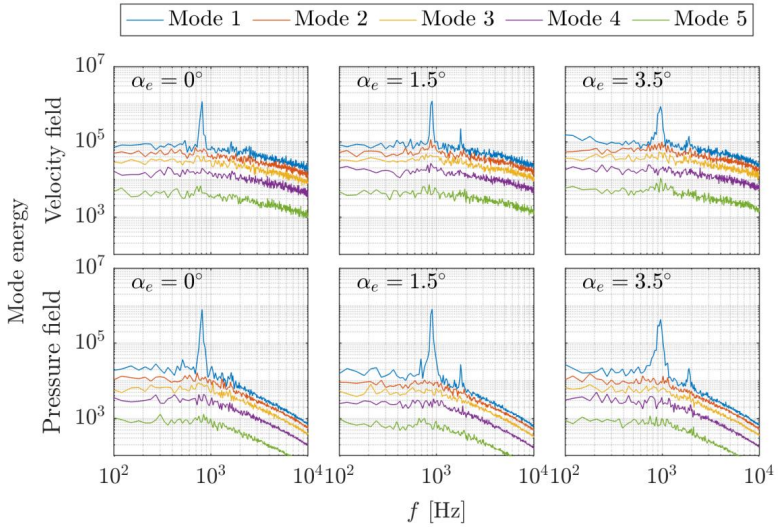

Figure 5.21: SPOD eigenvalue spectra of the five modes of the velocity (top row) and pressure field (bottom row) for t^*=0.030, u_∞ = 60 m/s ($Re_c = 1.1 \cdot 10^6$) and α_e = 0°, 1.5° and 3.5°.

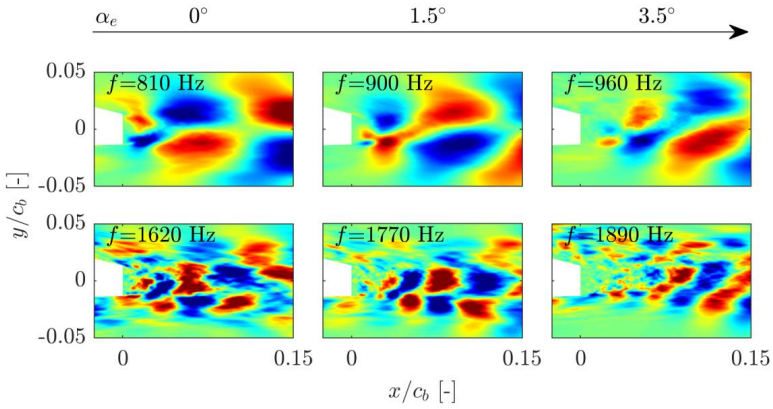

Figure 5.22: Leading velocity SPOD mode at indicated frequencies (f_{VS} in the first and $2f_{VS}$ in the second row) for t^*=0.030, u_∞ = 60 m/s ($Re_c = 1.1 \cdot 10^6$) and angles of attack α_e = 0°, 1.5°, 3.5°.

Figure 5.23 now displays the first pressure SPOD for the frequencies f_{VS} in the first and $2f_{VS}$ in the second row. Basically, when considering the pressure modes for f_{VS}, it can be stated that for all cases aerodynamically dominant structures can be observed in the airfoil wake. The aeroacoustic pressure fluctuations that typically propagate from the trailing edge upstream towards the LE (typical for TEN) are observable, especially for low aerodynamic loading. As the airfoil loading increases, the intensity decreases. For the frequency $2f_{VS}$, mainly aerodynamically dominant structures are present. This corresponds very well to the results observed for the far-field noise related to this frequency, but especially the behavior of the peak level, which decreases with increasing airfoil loading. Regarding the first harmonic $2f_{VS}$, the observations in the far-field are found in line as well, no contribution could be observed in the far-field noise.

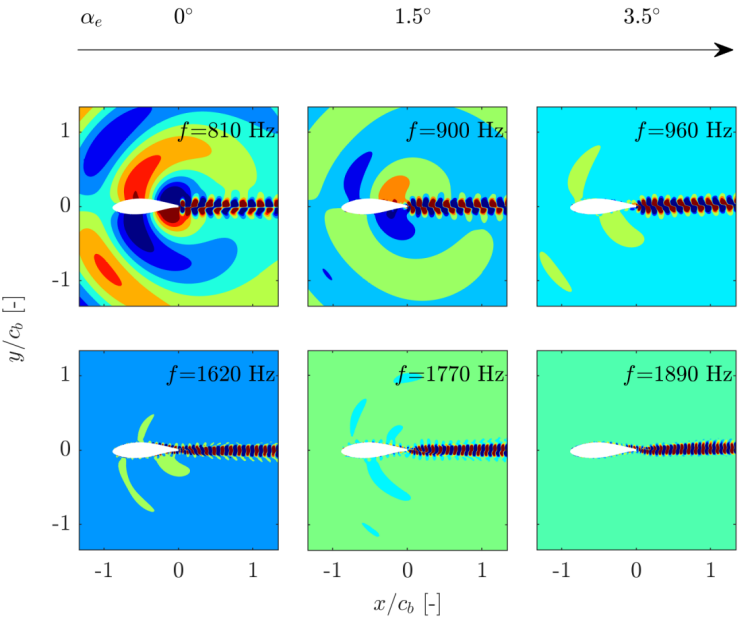

Figure 5.23: Leading pressure SPOD mode at indicated frequencies (f_{VS} in the first and $2f_{VS}$ in the second row) for t^*=0.030, u_∞ = 60 m/s ($Re_c = 1.1 \cdot 10^6$) and angles of attack α_e = 0°, 1.5°, 3.5°.

This suggests that the distance of the coherent structures from the trailing edge plays an essential role in noise propagation. From the averaged flow quantities, it could be observed that the recirculation zone behind the trailing edge expands downstream for increasing airfoil loading, which is accompanied by an increasing suction-side boundary layer as observed in Section 5.2.1. Thus, a remarkable conclusion is that the absence of BTEN in the far-field does

not mean that vortex shedding is not present. Rather, the asymmetric flow field and the extended recirculation zone appear to prevent the vortices from forming right after the TE and hence, impinging on the trailing edge. To shed further light on this mechanism, the reconstructed velocity and pressure field will be considered next.

Figure 5.24, Figure 5.25, and Figure 5.26 display the time evolution of the reconstructed pressure and velocity fluctuations field for the respective frequency, f_{VS} = 810 Hz, 900 Hz, and 960 Hz, over one time period T. On one hand, the formation of the vortices at the trailing edge, the resulting vortex street, and its movement downstream are very well recognizable, but also the scattering of the noise at the trailing edge. This is easily detectable for all cases. The comparison of the reconstructed velocity fields between the different aerodynamic loadings are in line with the results of the averaged flow field data and the visualized SPOD modes: With increasing aerodynamic loading, the vortex street shifts towards the pressure side and forms further downstream. Simultaneously it is evident that the amplitudes of the noise radiated at the trailing edge or pressure fluctuations become weaker as the angle of attack increases.

Please note that the coloring had to be changed between the cases. This manifests the assumption that the distance of the formatting position of those structures to the trailing edge plays an essential role. If the distance gets too large, the turbulent structures of the vortex street do not interact with the trailing edge and noise is not scattered by it. Therefore, no contribution of BTEN is found in the far-field and the coherent structures are purely aerodynamic in nature. Conversely, the absence of an aeroacoustic BTEN signature in the far field does not mean that no vortex street is formed in the wake.

By comparing the coloring of the turbulent structures within the boundary layer for the different angles of attack, it is also noticeable that the intensity of the structures change with the angle of attack. In terms of intensity, the results for an angle of attack of 0°, in particular, stand out here. It is hypothesized that the turbulent structures moving toward the trailing edge are amplified by the upstream propagating acoustic wave. These turbulent structures then continue to move downstream, toward the TE, interact with the TE, and again scatter aeroacoustic pressure fluctuations generating a feedback-loop.

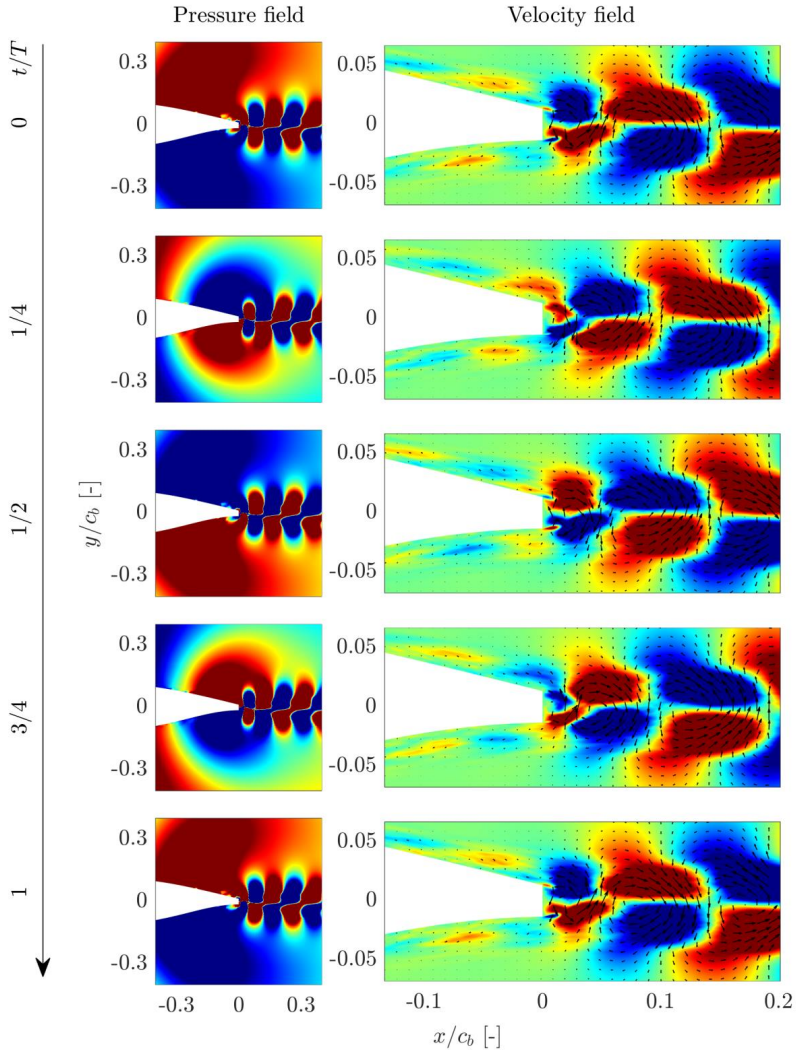

Figure 5.24: Time evolution of reconstructed pressure (colormap: -5 Pa to 5 Pa) and velocity fluctuations (colormap: -2.5 m/s to 2.5 m/s) over one period as indicated for different t/T for the shedding frequency f_{VS} = 810 Hz.

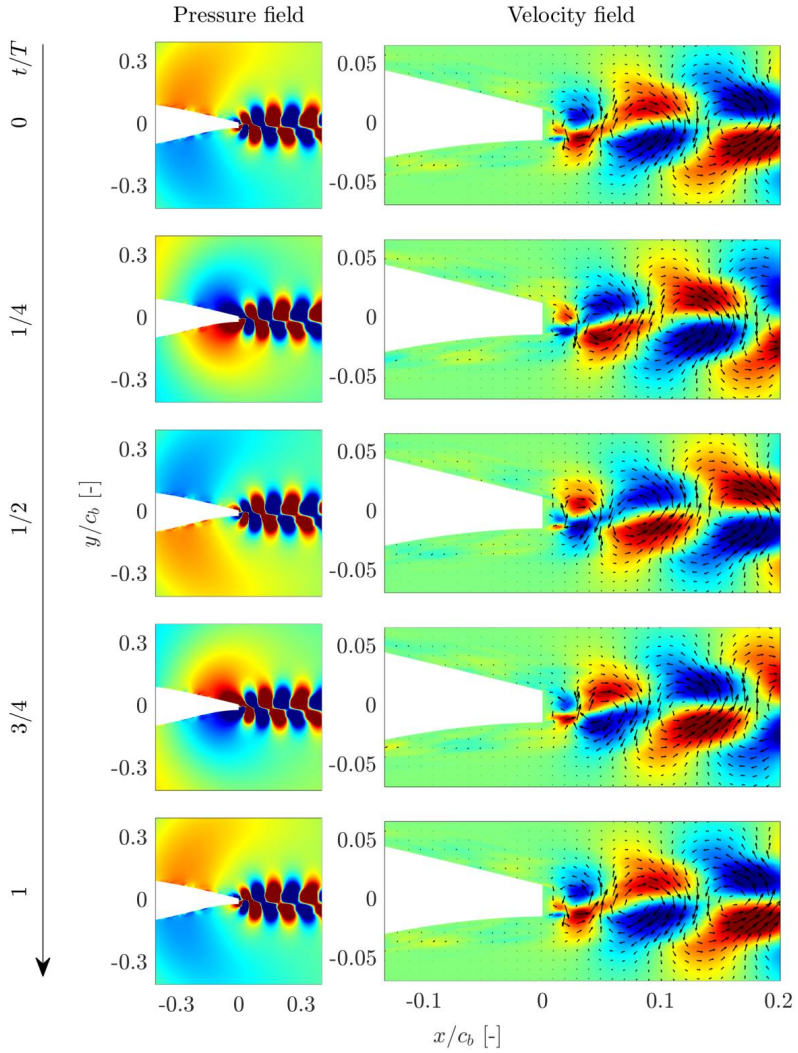

Figure 5.25: Time evolution of reconstructed pressure (colormap: -5 Pa to 5 Pa) and velocity fluctuations (colormap: -2.5 m/s to 2.5 m/s) over one period as indicated for different t/T for the shedding frequency f_{VS} = 900 Hz.

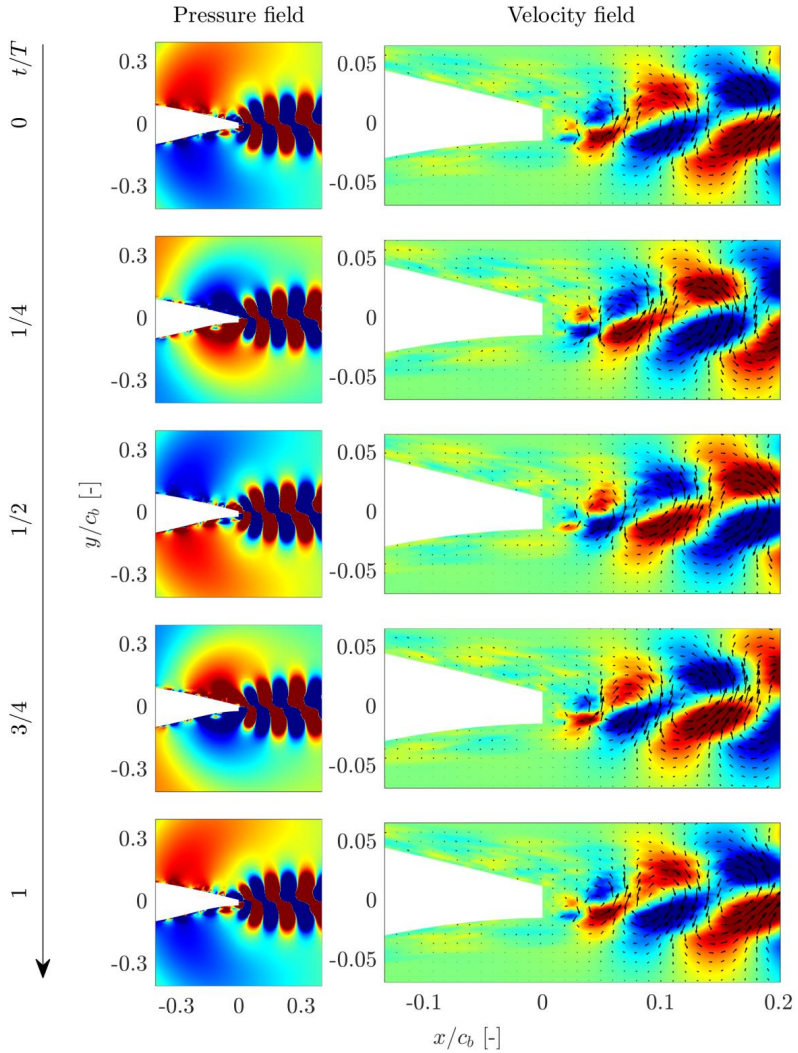

Figure 5.26: Time evolution of reconstructed pressure (colormap: -0.5 Pa to 0.5 Pa) and velocity fluctuations (colormap: -1 m/s to 1 m/s) over one period as indicated for different t/T for the shedding frequency f_{VS} = 943 Hz.

Finally, the influence of the angle of attack on the signature of BTEN in the far field will be discussed. Again, it becomes clear that the distance of the vortex street to the trailing edge plays an essential role. To further substantiate this, a two-point cross-correlation was calculated according to Eq. 3.8 from the reconstructed pressure field at f_{VS} and $2f_{VS}$ for the cases with high degree of bluntness, high REYNOLDS number, and different aerodynamic loading. By two point cross-correlation is meant, that the cross-correlation of the time trace of the pressure fluctuations at a selected position (here within the airfoil wake, indicated by the arrow) to the rest of the field are calculated.

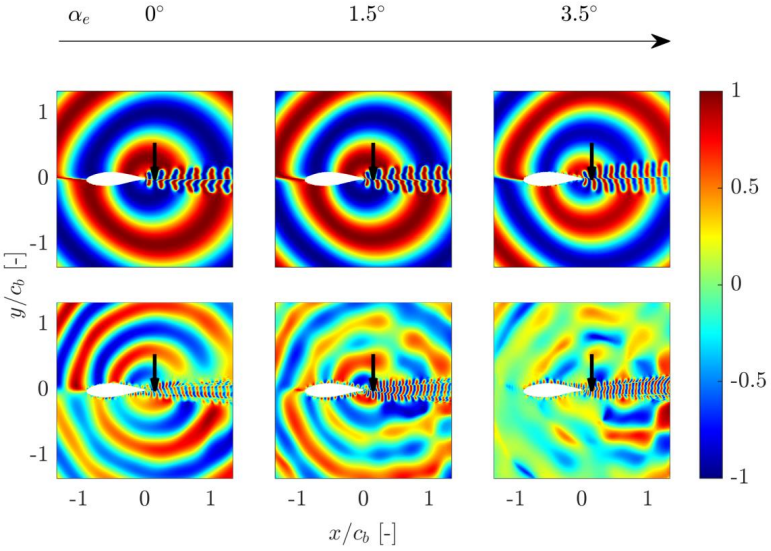

Figure 5.27: Cross-correlation of frequency isolated reconstructed pressure field to the reference point within the airfoil wake (indicated by the black arrow) for t^*=0.030, u_∞ = 60 m/s and angles of attack α_e and frequencies f_{VS} (top row) and its first harmonic (bottom row).

The correlation was calculated for f_{VS} and $2f_{VS}$. The evaluation of the cross-correlation for the vortex shedding frequency reveals that the correlation is less pronounced with increasing angle of attack. For the first harmonic, a lower correlation is already evident at an angle of attack of $\alpha_e = 0°$, which decreases further with the angle of attack. If this is combined with the reconstructed flow images for these cases, see Figure 5.27, the distance to the trailing edge in which the coherent structures are formatted is again noticeable.

Table 5.4: Shedding frequencies for cases where shedding was observed in the LBM simulations. Captured in the far-field at microphone position M4 $f_{VS,FFA}$ and obtained by the SPOD analysis $f_{VS,SPOD}$.

Case	Configuration			LBM results for	
	α_e [°]	u_∞ [m/s]	t^* [-]	$f_{VS,\ FFA}$ [Hz]	$f_{VS,\ SPOD}$ [Hz]
III	3.5	30	0.005	-	510 - 825
VI	3.5	60	./.	-	1,140 – 1,690
IX	3.5	30	0.014	-	392 – 785
X	0	60	./.	1,560	1,560
XII	3.5	./.	./.	-	1,170
XIII	0	30	0.022	510	510
XIV	1.5	./.	./.	510	510
XV	3.5	./.	./.	-	510
XVI	0	60	./.	1,020	1,020
XVII	1.5	./.	./.	1,170	1,140
XVIII	3.5	./.	./.	-	1,020
XIX	0	30	0.030	390	390
XX	1.5	./.	./.	420	420
XXI	3.5	./.	./.	450	450 / 930
XXII	0	60	./.	810	810 / 1,620
XXIII	1.5	./.	./.	900	900 / 1,770
XXIV	3.5	./.	./.	930	960 / 1,890

5.3 Scaling of BTEN

As already BLAKE pointed out, different TE geometries suggest a different *St* scaling of BTEN [11]. Figure 5.28 depicts the dimensional acoustic spectra as a function of all parameters varied. Only cases are considered where a blunt trailing edge noise is noticeable. Figure 5.29 shows different attempts of non-dimensionalization. The definitions of STROUHAL number 2.5a-c in Section 2.2 are applied for non-dimensionalization of the frequency. The spectral levels are normalized with the MACH number and the length scale ratios accordingly.

As a conclusion, the parameters which form Eq. 2.5c, seem to be most suitable. However, the collapse of data is not perfect. All length scales employed so far are based on geometrical and/or time-averaged flow field parameters. It is hypothesized that in cases where the BTEN is less distinct, the generation of vortices at the TE may be stochastic, which would require parameters including this effect. Nevertheless, advanced simulations seem to constitute the most appropriate tool for the ultimate analysis of BTEN from a realistic airfoil section as a function of REYNOLDS number, angle of attack, and degree of bluntness.

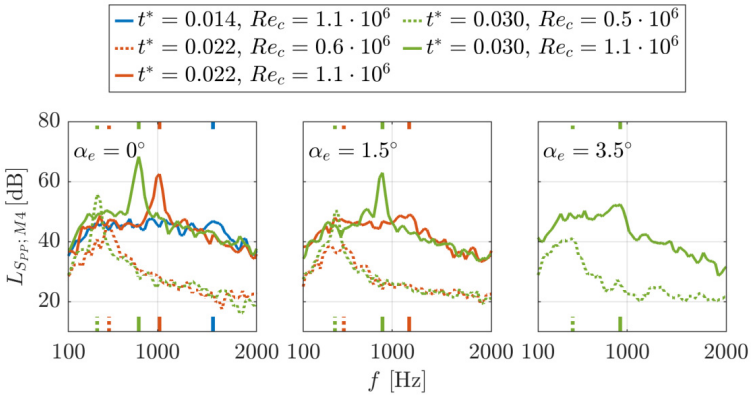

Figure 5.28: Dimensional acoustic spectra as a function of all parameters varied. (Captured at microphone position M4, only cases are considered where a blunt trailing edge noise is noticeable). The frequency at which BTEN occurs in the respective case is marked along the upper and lower x-axis.

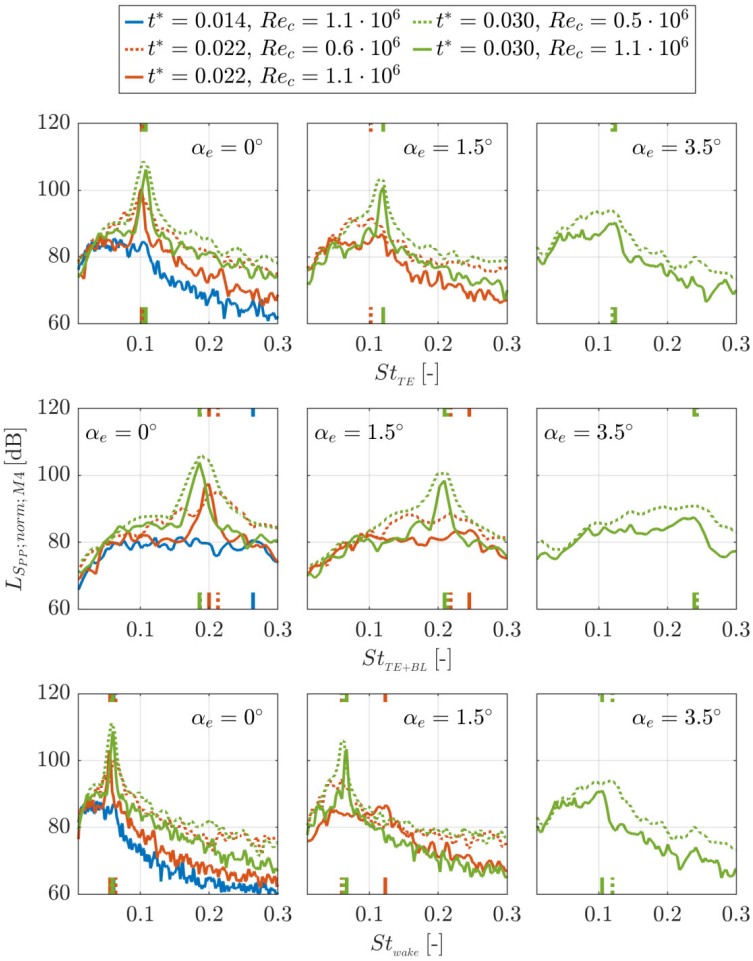

Figure 5.29: Non-dimensional acoustic spectra employing Eq. 2.5a. (top row) 2.5b (middle row) and 2.5c (bottom row), the STROUHAL number at which BTEN occurs in the respective case is marked along the upper and lower *x*-axis.

6. Final conclusion and outlook

The overall objective of this thesis was to shed further light on the mechanism responsible for generating (tonal) blunt trailing edge noise (BTEN) from an airfoil in a flow. The degree of bluntness of the trailing edge (TE) certainly plays the primary role for the formation of large-scale flow structures similar to a Kármán vortex street in the wake of the airfoil. But what are other supporting or preventing conditions for the existence of shedded vortices? And furthermore, does vortex shedding from the trailing edge always result in tonal BTEN?

Many preceding studies on BTEN were confined to the flat plate or symmetrical airfoils at zero lift condition. In contrast, this work deals with a typical state-of-the-art asymmetric airfoil, operated at different angles of attack which is considered synonymous with "aerodynamic" loading of the airfoil. This corresponds to greater-than-zero lift and is of utmost practical relevance, particularly for the design of turbomachinery like for instance wind turbines.

According to the literature, the boundary layer on the airfoil suction and pressure side in interaction with the trailing edge decides about the type of trailing edge noise (TEN), i.e. broadband only or broadband with tones, and their levels. Therefore, for an in-depth study, it is indispensable to capture the turbulent boundary layer flow around the complete airfoil and the unsteady flow field in the vicinity of the TE and the wake. As a consequence, and encouraged by some of the latest references, the numerical Lattice-BOLTZMANN Method (LBM) with the Very Large Eddy Simulation (VLES) turbulence model was selected as the workhorse in this study. Since LBM is able to resolve the unsteady and compressible flow field with low dissipation and dispersion, the direct extraction of the sound pressure in the computational domain is possible.[3] Exemplary results were verified via a mesh refinement study and the variation of the computational domain. Favorable agreement of the LBM results with experimental, and – to a minor degree – XFOIL data led to the conclusion that the numerical method is considered as validated for the current study.

Key findings concerning the far-field noise emitted by the airfoil in the flow are:

- As long as the loading of the airfoil is small: Increasing the trailing edge bluntness causes a distinct tone of increasing level. The bluntness parameter *BP*, i.e. the ratio of the geometric thickness of the trailing edge and the averaged boundary displacement thickness close to the trailing edge was confirmed to be a first suitable metric: For $BP > 0.3$ a tone occurs, as already stated by BLAKE [11]. However, this is only true for relatively low loading of the airfoil. Increased loading tends the tonal BTEN to disappear, even if $BP > 0.3$.

[3] A second option to obtain the far field sound, but rarely used in this work, is to feed the Ffowcs-Williams-Hawkings (FW-H) analogy with unsteady flow field data from the LBM.

- The frequency of the tone, if existent, decreases with degree of bluntness and increases with REYNOLDS number (i.e. the free stream flow velocity).
- Increasing the chord-based REYNOLDS number rises the levels of both, the broad band and the tonal spectral components of the noise.

In a next step standard and advanced methods of flow field analysis were applied in order to link the acoustic far-field signature of the airfoil to flow phenomena:

Time-averaged and rms-velocity maps indicated that in case of the sharp trailing edge and 0° angle of attack, the recirculation zone in the wake contains only one vortex. As the bluntness and the REYNOLDS number are increased, gradually a second vortex develops, resulting in regions with large velocity fluctuations downstream of the trailing edge. The surface pressure fluctuations in the vicinity of the TE showed a very similar spectral shape as the far-field spectra, tonal components are visible for the same combinations of parameters as in acoustic spectra.

A comprehensive POD analysis allowed the spatial resolution of the coherent structures directly related to BTEN. The most dominant modes could be related to the coherent structure of the vortex street, which - in turn - correlates with the BTEN signature. Since the POD analysis is limited as it only resolves spatial modes, a spatially and temporally resolved analysis was carried out with the help of SPOD. The modes obtained with SPOD revealed peaks, consistent with the far-field signature of BTEN. With increasing airfoil loading, these signatures disappear in the acoustic far-field but remain present in the SPOD evaluation. The reconstruction of the velocity and pressure fields for the corresponding isolated frequency ranges showed that a vortex street is formed independent of the angle of attack and bluntness but at different distances to the trailing edge.

The final conclusion is that the existence of vortex shedding does not always coincide with a tonal acoustic signature. In the case of large bluntness and comparably small aerodynamic loading of the complete airfoil, the shedded vortices are located close to the trailing edge, resulting in distinct acoustic tones. It is hypothesized that for these cases the turbulent structures moving toward the trailing edge are amplified by the upstream propagating acoustic wave. On the other hand, increased loading intensifies the asymmetry of suction and pressure side boundary layer. As a consequence, even for comparably blunt TEs, the shedded vortices are shifted away from the TE such that they do not impinge any longer on the airfoil surface. This explains the absence of the typical BTEN signature when loading the airfoil aerodynamically.

Utilizing well-known parameters for scaling frequency and levels of the acoustic spectra shows some success, though the data does not coincide perfectly. It is hypothesized that in cases where the BTEN is less distinct, the generation of vortices at the TE may be stochastic, which would require parameters including this effect. Nevertheless, advanced simulations seem to be the most appropriate tool for the ultimate analysis of BTEN from a realistic airfoil section as a function of REYNOLDS number, angle of attack, and degree of bluntness.

It is important to mention that this study was confined to a fully turbulent boundary layer along the airfoil from leading to trailing edge, ensured by the relatively large values of the chord-based REYNOLDS number in combination with a carefully designed boundary layer tripping close to the leading edge.

The findings obtained in this thesis can be supplemented by further investigations. The *BP* is shown to be a good indicator for the occurrence of BTEN, but at high airfoil loads, a comparatively high *BP* was shown with only a small BTEN contribution in the spectrum. It is to be investigated whether the *BP* can be used as an indicator for higher angles of attack or if a more robust parameter, which takes into account the load on the airfoil, is required.

Further research is needed on scaling the BTEN frequencies with a suitable STROUHAL number. The results show good scalability with the STROUHAL number formed with the characteristic length from the wake of the airfoil. However, there are larger deviations for higher airfoil loads. Here it is suspected that a characteristic length is not to be found in the averaged quantities of the wake but in the unsteady quantities.

For low airfoil loading and high degree of bluntness, it is hypothesized that the turbulent structures moving toward the trailing edge are amplified by the upstream propagating acoustic wave. These turbulent structures then continue to move downstream, toward the TE, interact with the TE, and again scatter aeroacoustic pressure fluctuations generating a feedback loop. The presence of such a feedback loop and the associated hypothesis were not investigated further in this work and require further investigation.

The applied experimental and numerical methods provide good results in pursuit of the objectives of this work. Dependencies of the varied parameters (REYNOLDS number, angle of attack, and degree of bluntness) with respect to the occurrence of BTEN could be shown. However, there were some differences between experimental and numerical results, for which only assumptions could be made in this work. For example, the experimental determination of boundary layer sizes could provide further information. From a numerical point of view, the mesh could be checked especially with respect to the blunt trailing edges. Besides, measures to reduce the background noise at the experimental setup could be taken to extend the area with an adequate signal-to-noise ratio.

Appendix A. Boundary layer tripping

As initially stated this study is confined to a fully turbulent boundary layer on pressure and suction side. For both, the numerical simulation and the experiments, this requires careful tripping. The challenge is to ensure transition close to leading edge for all operation conditions but without overtripping. Overtripping would prevent the boundary layer from developing similarly to a "natural" turbulent boundary layer. Thus, if the tripping band is too thick, the boundary layer thickness will be higher than the naturally formed boundary layer. For this reason, simulations were carried out with different tripping band thicknesses. The purpose was to find a tripping band with sufficient thickness to enforce the laminar-turbulent transition. The tripping band thickness was increased stepwise on suction and pressure side by 0.1 mm and the vorticity as well as the turbulent kinetic energy around the airfoil were examined visually. Furthermore, the surface pressure fluctuations close to the trailing edge were analyzed. Due to the abundance of results, not all can be presented here. However, as an example, the selection procedure for two selected tripping band thicknesses is given. For this Figure A.1 depicts the power spectral density of the surface pressure fluctuations for one airfoil geometry (t^*=0.005) under constant flow conditions (α_e = 3.5° and Re =1.2·10^6).

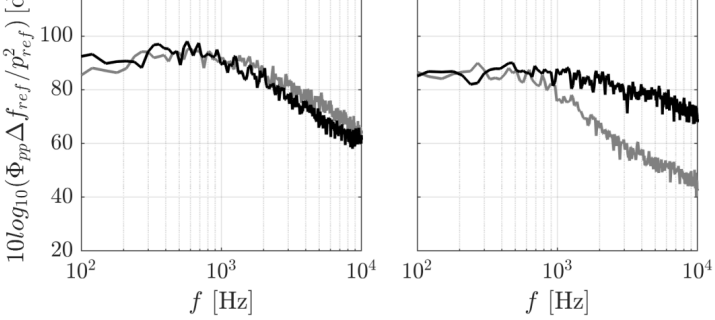

Figure A.1: Surface pressure fluctuations on the suction (left) and pressure side (right) at 0.93c derived by LBM simulations for different tripping band thicknesses under the constant flow conditions α_e = 3.5°, Re_c = 1.2 ·10^6 and t^* = 0.005.

The selected tripping band thicknesses were 0.5 and 0.6 mm for the suction and 0.6 and 0.7 mm for the pressure side. Figure A.2 and Figure A.3 show the vorticity and turbulent kinetic energy for the same scenario. Especially the pressure side in the upper snapshot of Figure A.2 and Figure A.3 shows in each case that activities are present, but these do not seem to be resolved by the mesh and the VLES model used for the sub-grid unresolved scales does not

have the required velocity gradient to turn turbulent. The power spectral density of the surface pressure fluctuations shows higher levels for the low-frequency range and a drastic drop beyond a frequency of 1 kHz which indicates still that the boundary layer is not fully turbulent. On the suction side, however, the tripping band thickness of 0.5 mm appears to be sufficient. Both power spectral density and snapshots reveal a turbulent boundary layer.

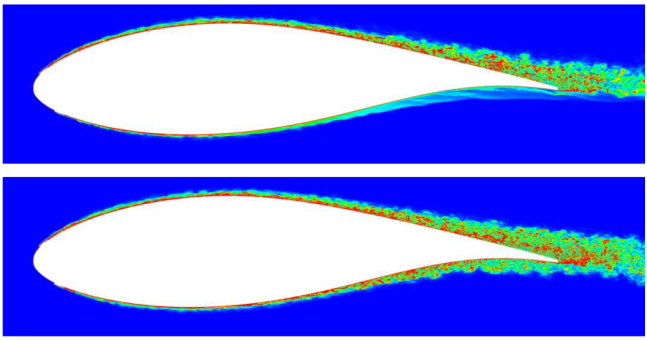

Figure A.2: Instantaneous snapshot of the vorticity field in the vicinity of the airfoil for α_e = 3.5°, Re_c = 1.2 ·10^6 and t^* = 0.005 a tripping band thickness of SS 0.5 mm, PS 0.5 mm (top) and SS 0.6 mm PS 0.7 mm (bottom).

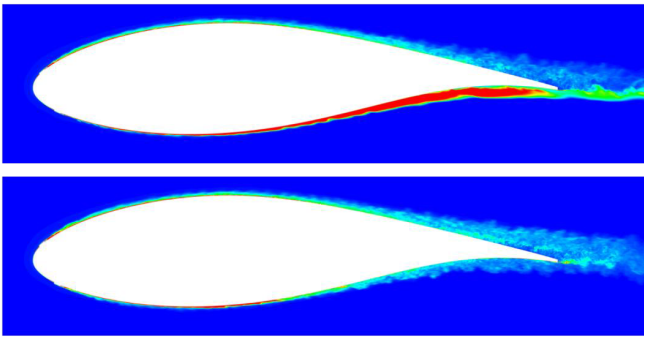

Figure A.3: Instantaneous snapshot of the turbulent kinetic energy in the vicinity of the airfoil for α_e=3.5°, Re_c 1.2·10^6 and t^*=0.005 a tripping band thickness of SS 0.5 mm, PS 0.5 mm (top), and SS 0.6 mm PS 0.7 mm (bottom).

Whereas for the lower snapshots, with thicker tripping band, the vorticity and the turbulent kinetic energy show fine structures on suction and pressure side, additionally the power spec-

tral density of the surface pressure fluctuations demonstrate the typical course of turbulent boundary layers on suction and pressure side. Hence, a fully turbulent boundary layer is present on both sides.

It was observed that changing the airfoil loading and truncation affected the required tripping thickness. For this reason, it was carefully checked for each case whether a turbulent boundary layer was present.

In the experiment, the boundary layer was evaluated with the use of a stethoscope. A sensitive behavior regarding airfoil loading and truncation was also observed within experiments.

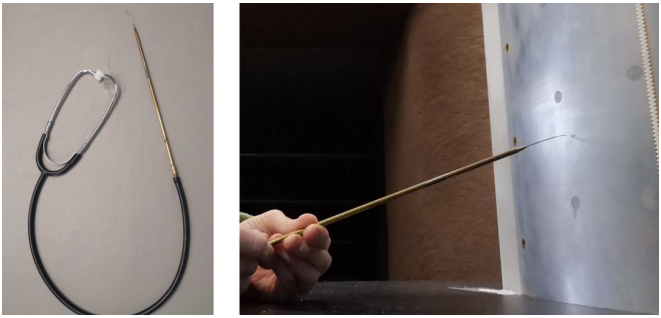

Figure A.4: Stethoscope (left) and stethoscope in use (right).

Appendix B. Geometric vs. effective angle of attack

For wind tunnel measurements with an open-jet the *geometric* angle of attack α_g typically does not correspond to free-flow conditions due to flow curvature and a downwash deflection. This decreases the effective angle of attack α_e which represents the free flow condition, and hence the lift. Therefore, the geometric angle of attack α_g has to be translated into an equivalent effective angle of attack α_e in order to generate the same lift. For the particular measurement setup at the UNIVERSITY OF SIEGEN, this relationship was established by a comparison of experimentally obtained pressure distributions with those from XFOIL [77]. The equivalent angles of attack can be taken from Table B.1. In the experimentally determined pressure distribution, a small jump can be seen on the suction side distribution at the point $x/c = 0.7$. This may be attributed to a small step on the suction side at the connection between the base model and the exchangeable TE section due to unavoidable manufacturing tolerances.

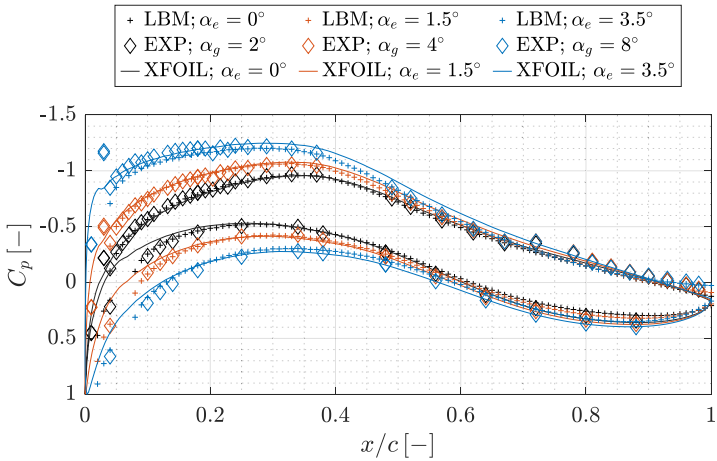

Figure B.1: Static pressure distributions obtained from experiments, LBM- and XFOIL-simulations.

Table B.1: Effective angles of attack and their equivalent geometric angles of attack.

LBM	XFOIL	EXP
α_e [°]	α_e [°]	α_g [°]
0	0	2
1.5	1.5	4
3.5	3.5	8

Appendix C. The probe microphone for unsteady surface pressure measurements

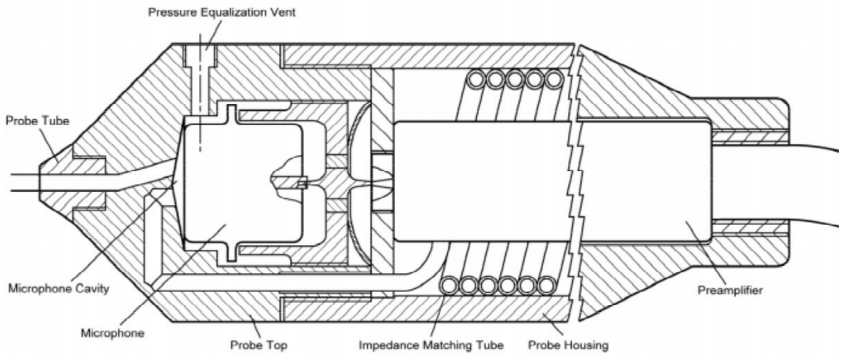

Figure C.1: Schematic representation of the internal construction of the BRÜEL & KJÆR probe microphone type 4182 showing the microphone cavity, equalization vent, and impedance matching tube [78].

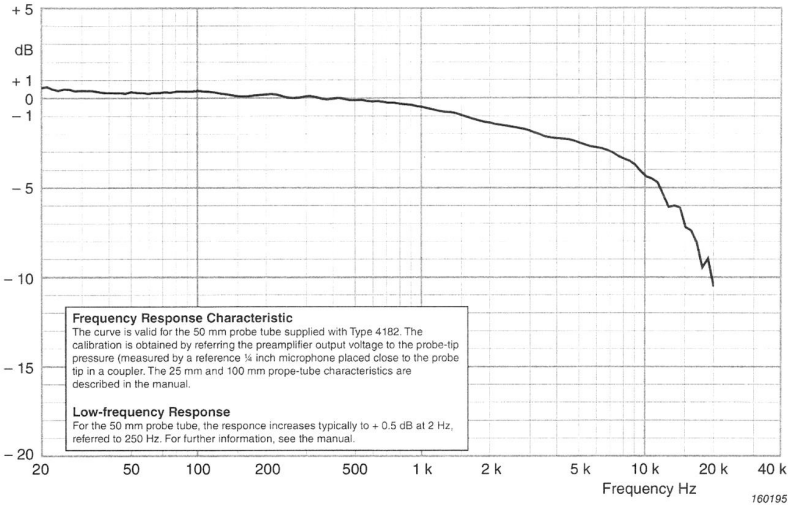

Figure C.2: Typical frequency responses for various stiff probe tube lengths; throughout this study only the tube length 50 mm is used; taken from BRÜEL & KJÆR product data-sheet probe microphone - type 4182 [78].

Appendix D. Aerodynamic effect of trailing edge truncation

In this Section, the qualitative effect caused by the geometry change due to the stepwise truncation of the trailing edge will be shown. For this purpose, the pressure distribution as well as lift and drag will be discussed. A first insight into the effect of truncating the airfoils TE is provided by the LBM predicted pressure distributions in Figure D.1 and Figure D.2 for angles of attack of α_e = 0°, 1.5°, and 3.5°, respectively. The differences are evident for both angles of attack, as almost the entire pressure distribution on both the suction and pressure sides is affected.

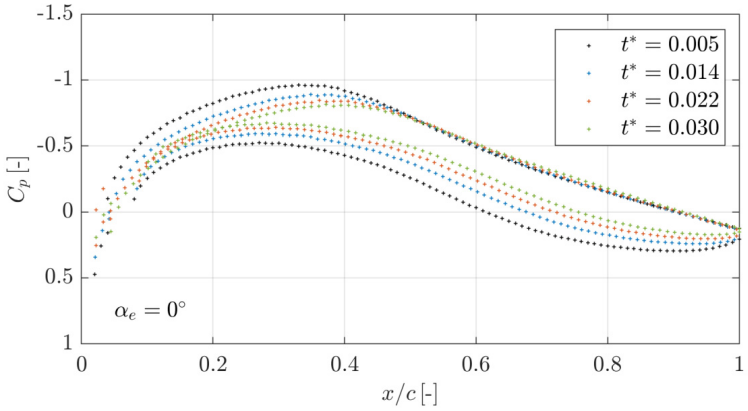

Figure D.1: Pressure distribution for trailing edge thickness-to-chord ratios t^* of 0.005, 0.014, 0.022 and 0.030 at α_e = 0°.

Table D.1 depicts the corresponding coefficients of lift and drag. It can be seen that the drag coefficient undergoes only small changes due to truncating the TE. This behavior was in agreement with the publications from MUCIA AND PINILLA [79]. What at first glance looks like a large loss in lift is in fact a shift of the entire curve towards smaller angles of attack. Furthermore, MUCIA AND PINILLA [79] showed that the stall angle can be positively influenced by the geometry change. This would also be expected here as well. To support this with results, further LBM predictions would be necessary. However, this chapter should only give a small insight into the effect on the qualitative effect. The main focus of this thesis is the effect of the angle of attack for the different airfoil geometries on the aeroacoustics, which will be discussed further in the next chapter.

Table D.1: Lift C_l and drag C_d coefficient different angles of attack α_e trailing edge thickness-to-chord ratios t^* at a freestream velocity of u_∞ = 60 m/s

	Angle of attack α_e	t^*=0.005	t^*=0.014	t^*=0.022	t^*=0.030
C_l	0°	0.384	0.247	0.167	0.107
C_l	1.5°	0.528	0.378	0.287	0.242
C_l	3.5°	0.708	0.550	0.441	0.392
C_d	0°	0.020	0.019	0.019	0.019
C_d	1.5°	0.023	0.022	0.021	0.021
C_d	3.5°	0.027	0.025	0.025	0.024

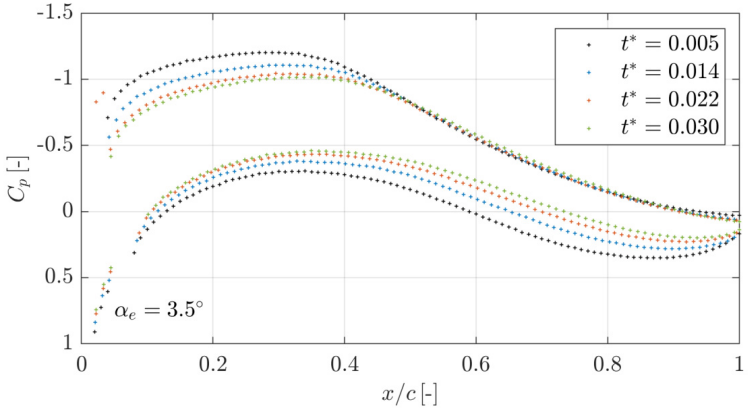

Figure D.2: Pressure distribution for trailing edge thickness-to-chord ratios t^* of 0.005, 0.014, 0.022 and 0.030 at α_e = 3.5°

References

[1] WAGNER, S., BAREISS, R. AND GUIDATI, G.: *Wind Turbine Noise.* Springer, Berlin, Germany, 1996.

[2] BROOKS, T. F., POPE, D. S. AND MARCOLINI, M. A.: *Airfoil Self-Noise and Prediction*. NASA REFERENCE PUBL. 1218, 1989.

[3] ANDERSON, J. D.: *Fundamentals of aerodynamics*. Anderson series. McGraw-Hill, Singapore, 2011.

[4] FINK, M. R. AND BAILEY, D. A.: *Airframe Noise Reduction Studies and Clean-Airframe Noise Investigation*. NASA CONTRACTOR REPORT, R80-914626-12, 1980.

[5] MOREAU, S., ROGER, M. AND CHRISTOPHE, J.: *Flow Features and Self-Noise of Airfoils Near Stall or in Stall*. Proceedings of the 15th AIAA/CEAS Aeroacoustics Conference, Miami (FL), USA, 2009.

[6] PATERSON, R. W., AMIET, R. K. AND MUNCH, C. L.: *Isolated Airfoil-Tip Vortex Interaction Noise*. Journal of Aircraft, Vol. 12, No. 1, pp. 34–40, 1975.

[7] FINK, M. R.: *Prediction of Airfoil Tone Frequencies*. Journal of Aircraft, Vol. 12, No. 2, pp. 118–120, 1975.

[8] PATERSON, R. W., VOGT, P. G., FINK, M. R. AND MUNCH, C. L.: *Vortex Noise of Isolated Airfoils*. Journal of Aircraft, Vol. 10, No. 5, pp. 296–302, 1973.

[9] TAM, C. K. W.: *Discrete Tones of Isolated Airfoils*. The Journal of the Acoustical Society of America, Vol. 55, No. 6, pp. 1173–1177, 1974.

[10] YAKHINA, G., ROGER, M., MOREAU, S., NGUYEN, L. AND GOLUBEV, V.: *Experimental and Analytical Investigation of the Tonal Trailing-Edge Noise Radiated by Low Reynolds Number Aerofoils*. Acoustics, Vol. 2, No. 2, pp. 293–329, 2020.

[11] BLAKE, W. K.: *Mechanics of flow-induced sound and vibration - Complex Flow-Structure Interactions.* Academic Press, London, England, 2017.

[12] HERR, M.: *Trailing-Edge Noise - Reduction Concepts and Scaling Laws*. DLR Forschungsbericht. Deutsches Institut für Luft- und Raumfahrt e.V., PhD thesis, 2013.

[13] BROOKS, T. F. AND HODGSON, T. H.: *Trailing Edge Noise Prediction from Measured Surface Pressures*. Journal of Sound and Vibration, Vol. 78, No. 1, pp. 69–117, 1981.

[14] CHEVRAY, R. AND KOVASZNAY, L.: *Turbulence Measurements in the Wake of a Thin Flat Plate*. AIAA Journal, Vol. 7, No. 8, pp. 1641–1643, 1969.

[15] HUTCHESON, F. V. AND BROOKS, T. F.: *Measurement of Trailing EDGE Noise Using Directional Array and Coherent Output Power Methods*. International Journal of Aeroacoustics, Vol. 1, No. 4, pp. 329–353, 2002.

[16] HUTCHESON, F. V. AND BROOKS, T. F.: *Effects of Angle of Attack and Velocity on Trailing Edge Noise*. Proceedings of the 42nd AIAA Aerospace Sciences Meeting and Exhibit, Reno (NV), USA, 2004.

[17] BARONE, M. AND BERG, D.: *Aerodynamic and Aeroacoustic Properties of a Flatback Airfoil: An Update*. Proceedings of the 47th AIAA Aerospace Sciences Meeting including The New Horizons Forum and Aerospace Exposition, Orlando (FL), USA, 2009.

[18] BERG, D. AND ZAYAS, J.: *Aerodynamic and Aeroacoustic Properties of Flatback Airfoils*. Proceedings of the 46th AIAA Aerospace Sciences Meeting and Exhibit, Reno (NV), USA, 2008.

[19] VAN DER VELDEN, W. C.: *Computational Aeroacoustic Approaches for Wind Turbine Blade Noise Prediction*. DELFT UNIVERSITY OF TECHNOLOGY, PHD THESIS, 2017.

[20] VAN DER VELDEN, W. C., PRÖBSTING, S., JONG, A. de, VAN ZUIJLEN, A., GUAN, Y. AND MORRIS, S.: *Numerical and Experimental Investigation of a Beveled Trailing Edge Flow and Noise Field*. Proceedings of the 21st AIAA/CEAS Aeroacoustics Conference, Dallas (TX), USA, 2015.

[21] VAN DER VELDEN, W. C., PRÖBSTING, S., VAN ZUIJLEN, A. H., JONG, A. T. de, GUAN, Y. AND MORRIS, S. C.: *Numerical and Experimental Investigation of a Beveled Trailing Edge Flow Field and Noise Emission*. Journal of Sound and Vibration, Vol. 384, pp. 113–129, 2016.

[22] BILKA, M. J., MORRIS, S. C., BERNTSEN, C., SILVER, J. C. AND SHANNON, D. W.: *Flowfield and Sound from a Blunt Trailing Edge with Varied Thickness*. AIAA Journal, Vol. 52, No. 1, pp. 52–61, 2014.

[23] LEW, P.-T., NAJAFIYAZDI, A. AND MONGEAU, L.: *Numerical Simulation of Sound from Flow over an Airfoil with a Blunt Trailing Edge*. Proceedings of the 16th AIAA/CEAS Aeroacoustics Conference, Stockholm, Sweden, 2010.

[24] SHANNON, D. W.: *Flow Field and Acoustic Measurements of a Blunt Trailing Edge.* University of Notre Dame, PhD thesis, 2007.

[25] SHANNON, D. W. AND MORRIS, S. C.: *Experimental Investigation of a Blunt Trailing Edge Flow Field with Application to Sound Generation*. Experiments in Fluids, Vol. 41, No. 5, pp. 777–788, 2006.

[26] SHANNON, D. W. AND MORRIS, S. C.: *Trailing Edge Noise Measurements Using a Large Aperture Phased Array*. International Journal of Aeroacoustics, Vol. 7, No. 2, pp. 147–176, 2008.

[27] SHANNON, D. W., MORRIS, S. C. AND MUELLER, T. J.: *Radiated Sound and Turbulent Motions in a Blunt Trailing Edge Flow Field*. International Journal of Heat and Fluid Flow, Vol. 27, No. 4, pp. 730–736, 2006.

[28] WU, L., JING, X. AND SUN, X.: *Prediction of Vortex-Shedding Noise from the Blunt Trailing Edge of a Flat Plate*. Journal of Sound and Vibration, Vol. 408, pp. 20–30, 2017.

[29] ROGER, M., MOREAU, S. AND GUÉDEL, A.: *Vortex-Shedding Noise and Potential-Interaction Noise Modeling by a Reversed Sears' Problem*. Proceedings of the 12th AIAA/CEAS Aeroacoustics Conference, Cambridge (MA), USA, 2006.

[30] ROGER, M. AND MOREAU, S.: *Back-Scattering Correction and Further Extensions of Amiet's Trailing-Edge Noise Model. Part 1: Theory*. Journal of Sound and Vibration, Vol. 286, No. 3, pp. 477–506, 2005.

[31] HERR, M.: *Design Criteria for Low-Noise Trailing-Edges*. Proceedings of the 13th AIAA/CEAS Aeroacoustics Conference, Rome, Italy, 2007.

[32] HERR, M. AND DOBRZYNSKI, W.: *Experimental Investigations in Low-Noise Trailing Edge Design*. AIAA Journal, Vol. 43, No. 6, pp. 1167–1175, 2005.

[33] BROOKS, T. F. AND HODGSON, T. H.: *Prediction and Comparison of Trailing Edge Noise using Measured Surface Pressures*. Proceedings of the 6th Aeroacoustics Conference, Hartford (CT), USA, 1980.

[34] LE GARREC, T., GLOERFELT, X. AND CORRE, C.: *Direct Noise Computation of Trailing Edge Noise at High Reynolds Numbers*. Proceedings of the 14th AIAA/CEAS Aeroacoustics Conference, Vancouver (BC), Canada, 2008.

[35] KIM, T. AND LEE, S.: *Aeroacoustic Simulations of a Blunt Trailing-Edge Wind Turbine Airfoil*. Journal of Mechanical Science and Technology, Vol. 28, No. 4, pp. 1241–1249, 2014.

[36] ZHU, W. J., SHEN, W. Z., SØRENSEN, J. N. AND LELOUDAS, G.: *Improvement of Airfoil Trailing Edge Bluntness Noise Model*. Advances in Mechanical Engineering, Vol. 8, No. 2, pp. 1–12, 2016.

[37] TIMMER, W. A. AND VAN ROOIJ, R. P. J. O. M.: *Summary of the Delft University Wind Turbine Dedicated Airfoils*. Journal of Solar Energy Engineering, Vol. 125, No. 4, pp. 488–496, 2003.

[38] DASSAULT SYSTÈMES SIMULIA CORPORATION: *PowerFLOW 2020 User's Guide*, 2020.

[39] KRÜGER, T., KUSUMAATMAJA, H., KUZMIN, A., SHARDT, O., SILVA, G. AND VIGGEN, E. M.: *The Lattice Boltzmann Method - Principles and practice*. Graduate texts in physics. Springer International Publishing, Switzerland, 2017.

[40] GUO, Z. AND SHU, C.: *Lattice Boltzmann Method and its Applications in Engineering*. Advances in computational fluid dynamics, Vol. 3. World Scientific, Hackensack (NJ), USA, 2013.

[41] BHATNAGAR, P. L., GROSS, E. P. AND KROOK, M.: *A Model for Collision Processes in Gases. I. Small Amplitude Processes in Charged and Neutral One-Component Systems*. Physical Review, Vol. 94, No. 3, pp. 511–525, 1954.

[42] CHAPMAN, S. AND COWLING, T. G.: *The Mathematical Theory of Non-Uniform Gases - An Account of the Kinetic Theory of Viscosity, Thermal Conduction and Diffusion in Gases*. Cambridge mathematical library. Cambridge University Press, Cambridge, 1998.

[43] CHEN, H., CHEN, S. AND MATTHAEUS, W. H.: *Recovery of the Navier-Stokes Equations Using a Lattice-Gas Boltzmann Method*. Physical Review A, Vol. 45, No. 8, R5339-R5342, 1992.

[44] YAKHOT, V. AND ORSZAG, S. A.: *Renormalization Group Analysis of Turbulence. I. Basic Theory*. Journal of Scientific Computing, Vol. 1, No. 1, pp. 3–51, 1986.

[45] AVALLONE, F., VAN DER VELDEN, W. AND RAGNI, D.: *Benefits of curved serrations on broadband trailing-edge noise reduction*. Journal of Sound and Vibration, Vol. 400, pp. 167–177, 2017.

[46] LAUNDER, B. E. AND SPALDING, D. B.: *The Numerical Computation of Turbulent Flows*. Numerical Prediction of Flow, Heat Transfer, Turbulence and Combustion, pp. 96–116, 1983.

[47] KOTAPATI, R. B., SHOCK, R. AND CHEN, H.: *Lattice-Boltzmann Simulations of Flows Over Backward-Facing Inclined Steps*. International Journal of Modern Physics C, Vol. 25, No. 1, 1340021, 2014.

[48] TEIXEIRA, C. M.: *Incorporating Turbulence Models into the Lattice-Boltzmann Method*. International Journal of Modern Physics C, Vol. 9, No. 8, pp. 1159–1175, 1998.

[49] BRÈS, G., PÉROT, F. AND FREED, D.: *Properties of the Lattice Boltzmann Method for Acoustics*. Proceedings of the 15th AIAA/CEAS Aeroacoustics Conference, Miami (FL), USA, 2009.

[50] SANJOSÉ, M., MEON, C., MOREAU, S., IDIER, A. AND LAFFAY, P.: *Direct Numerical Simulation of Acoustic Reduction Using Serrated Trailing-Edge on an Isolated Airfoil*. Proceedings of the 20th AIAA/CEAS Aeroacoustics Conference, Atlanta (GA), USA, 2014.

[51] WAGNER, C., HÜTTL, T. AND SAGAUT, P.: *Large-Eddy Simulation for Acoustics.* Cambridge University Press, 2007.

[52] OBERAI, A. A., ROKNALDIN, F. AND HUGHES, T. J. R.: *Computation of Trailing-Edge Noise Due to Turbulent Flow over an Airfoil*. AIAA Journal, Vol. 40, No. 11, pp. 2206–2216, 2002.

[53] EWERT, R. AND SCHRÖDER, W.: *On the Simulation of Trailing Edge Noise with a Hybrid LES/APE Method*. Journal of Sound and Vibration, Vol. 270, No. 3, pp. 509–524, 2004.

[54] OBERAI, A. A., ROKNALDIN, F. AND HUGHES, T. J. R.: *Trailing-Edge Noise due to Turbulent Flows*. BOSTON UNIVERSITY, 2002.

[55] FFOWCS WILLIAMS, J. E. AND HAWKINGS, D. L.: *Sound Generation by Turbulence and Surfaces in Arbitrary Motion*. Philosophical Transactions of the Royal Society of London. Series A, Mathematical and Physical Sciences, Vol. 264, No. 1151, pp. 321–342, 1969.

[56] CASALINO, D.: *An Advanced Time Approach for Acoustic Analogy Predictions*. Journal of Sound and Vibration, Vol. 261, No. 4, pp. 583–612, 2003.

[57] FARASSAT, F. AND SUCCI, G. P.: *A Review of Propeller Discrete Frequency Noise Prediction Technology with Emphasis on Two Current Methods for Time Domain Calculations*. Journal of Sound and Vibration, Vol. 71, No. 3, pp. 399–419, 1980.

[58] BRÈS, G., PÉROT, F. AND FREED, D.: *A Ffowcs Williams - Hawkings Solver for Lattice-Boltzmann Based Computational Aeroacoustics*. Proceedings of the 16th AIAA/CEAS Aeroacoustics Conference, Stockholm, Sweden, 2010.

[59] CURLE, N.: *The Influence of Solid Boundaries Upon Aerodynamic Sound*. Proceedings of the Royal Society of London. Series A. Mathematical and Physical Sciences, Vol. 231, No. 1187, pp. 505–514, 1955.

[60] INTERNATIONAL STANDARDS ORGANIZATION, ISO 3745:2017. *Acoustics - Determination of Sound Power Levels and Sound Energy Levels of Noise Sources Using Sound Pressure - Precision Methods for Anechoic Rooms and Hemi-Anechoic Rooms*, Geneva, Switzerland, 2017.

[61] DEUTSCHES INSTITUT FÜR NORMUNG E.V., EN DIN 12599:2013. *Lüftung von Gebäuden–Prüf-und Messverfahren für die Übergabe raumlufttechnischer Anlagen (01.13).* Beuth, Berlin, Germany, 2013.

[62] VAN DER VELDEN, W. C., VAN ZUIJLEN, A. AND RAGNI, D.: *Flow Topology and Noise Emission Around Straight, Serrated and Slitted Trailing Edges Using the Lattice Boltzmann Methodology*. Proceedings of the 22nd AIAA/CEAS Aeroacoustics Conference, Lyon, France, 2016.

[63] BERKOOZ, G., HOLMES, P. AND LUMLEY, J. L.: *The Proper Orthogonal Decomposition in the Analysis of Turbulent Flows*. Annual Review of Fluid Mechanics, Vol. 25, No. 1, pp. 539–575, 1993.

[64] CHATTERJEE, A.: *An Introduction to the Proper Orthogonal Decomposition*. Current Science, No. 7, pp. 808–817, 2000.

[65] TAIRA, K., BRUNTON, S. L., DAWSON, S. T. M., ROWLEY, C. W., COLONIUS, T., MCKEON, B. J., SCHMIDT, O. T., GORDEYEV, S., THEOFILIS, V. AND UKEILEY, L. S.: *Modal Analysis of Fluid Flows: An Overview*. AIAA Journal, Vol. 55, No. 12, pp. 4013–4041, 2017.

[66] WEISS, J.: *A Tutorial on the Proper Orthogonal Decomposition*. Proceedings of the AIAA Aviation 2019 Forum, Dallas (TX), USA, 2019.

[67] CHEN, H., REUSS, D. L., HUNG, D. L. S. AND SICK, V.: *A Practical Guide for Using Proper Orthogonal Decomposition in Engine Research*. International Journal of Engine Research, Vol. 14, No. 4, pp. 307–319, 2013.

[68] SIROVICH, L.: *Turbulence and the Dynamics of Coherent Structures. I. Coherent Structures*. Quarterly of Applied Mathematics, Vol. 45, No. 3, pp. 561–571, 1987.

[69] TOWNE, A., SCHMIDT, O. T. AND COLONIUS, T.: *Spectral Proper Orthogonal Decomposition and its Relationship to Dynamic Mode Decomposition and Resolvent Analysis*. Journal of Fluid Mechanics, Vol. 847, pp. 821–867, 2018.

[70] GEORGE, W. K.: *A 50-Year Retrospective and the Future*. Whither turbulence and big data in the 21st century?, pp. 13–43.

[71] SCHMIDT, O. T. AND COLONIUS, T.: *Guide to Spectral Proper Orthogonal Decomposition*. AIAA Journal, Vol. 58, No. 3, pp. 1023–1033, 2020.

[72] LE FLOC'H, A.: *Étude Expérimentale d'une Famille de Bulbes de Décollement Turbulents.* École de technologie supérieure, University of Québec, PhD thesis, Montréal, Canada, 2021.

[73] LELE, S.: *Computational Aeroacoustics - A Review*. Proceedings of the 35th Aerospace Sciences Meeting and Exhibit, Reno (NV), USA, 1997.

[74] COLONIUS, T. AND LELE, S. K.: *Computational Aeroacoustics: Progress on Nonlinear Problems of Sound Generation*. Progress in Aerospace Sciences, Vol. 40, No. 6, pp. 345–416, 2004.

[75] MANEGAR, F. A., STAHL, K., CAROLUS, T. H. AND BINOIS, R.: *Noise Reduction Mechanism of Trailing Edge Blowing Using the Lattice-Boltzmann Method: Numerical and Experimental Analysis*. Proceedings of the 48th International Congress and Exhibition on Noise Control, Madrid, Spain, 2019.

[76] GRAVANTE, S. P., NAGUIB, A. M., WARK, C. E. AND NAGIB, H. M.: *Characterization of the Pressure Fluctuations Under a Fully Developed Turbulent Boundary Layer*. AIAA Journal, Vol. 36, No. 10, pp. 1808–1816, 1998.

[77] DRELA, M. AND YOUNGREN, H.: *XFOIL 6.94 User Guide*. AERONAUTICAL AND ASTRONAUTICAL ENGINEERING, Cambridge (MA), USA, 2001.

[78] BRÜEL & KJAER: *Product Data - Probe Microphone - Type 4182*. 003200000, Denmark.

[79] MURCIA, J. P. AND PINILLA, Á.: *CFD Analysis of Blunt Trailing Edge Airfoils Obtained with Several Modification Methods*. Revista de Ingeniería, No. 33, pp. 14–24, 2011.